Université de Montréal

Décharges Sparks dans les liquides diélectriques : caractérisation et application à la synthèse de nanoparticules

Par

Merciris Thomas

Université de Montréal, Faculté des arts et des sciences,

Département de Physique

Mémoire présenté en vue de l'obtention du grade de Maitrise

En Physique, option Plasma – Cheminement international.

Juillet 2020

Université de Montréal

Unité académique : Faculté des Arts et des Sciences, Département de Physique.

Ce mémoire intitulé

Décharges Sparks dans les liquides diélectriques : caractérisation et application à la synthèse de nanoparticules

Présenté par

Thomas Merciris

A été évalué(e) par un jury composé des personnes suivantes

Joëlle Margot
Présidente-rapporteuse

Ahmad Hamdan
Directeur de recherche

Flavien Valensi
Codirecteur

Nicolas Naudé
Membre du jury

Résumé

Ce projet de recherche s'inscrit dans le parcours international de la maitrise de Physique (option plasma) de l'Université de Montréal en collaboration avec l'Université Paul Sabatier de Toulouse (France). Il concerne la caractérisation des décharges électriques (Sparks) dans les liquides diélectriques et ses applications dans la synthèse de nanoparticules. L'objectif est d'amélioré la connaissance des conditions de formation des nanoparticules. Cela implique de caractériser l'ensemble du système expérimental et de développer sa métrologie d'une part, et d'autre part d'obtenir l'évolution des paramètres plasma lors de la synthèse.

Dans un premier temps, sur le site du LAPLACE (UMR5213), Toulouse, il a fallu développer une alimentation électrique impulsionnelle destinée à réaliser des décharges dans les liquides. En se basant sur un dispositif existant qui fût amélioré, le fonctionnement a été caractérisé du point de vue électrique (courant - tension). L'application à la synthèse de nanoparticules a été ensuite abordée pour différentes conditions expérimentales, en considérant l'aspect énergétique (bilan d'énergie, caractéristiques de la décharge…).

Les travaux se sont poursuivis à l'Université de Montréal, où un circuit électrique équivalent du système expérimental est réalisé afin de visualiser l'évolution temporelle des paramètres plasma (température et densité électronique) en fonction des paramètres électriques choisis. Aussi, la synthèse de nanoparticules de Co et Ni par la décharge a été évaluée et les nanoparticules formées sont caractérisées à l'aide du microscope électronique à Transmission de Polytechnique Montréal..

Mots-clés : Nanoparticules, Décharges Spark, Circuits équivalents, Nickel, Cobalt, Générateur haute-tension impulsionnelle, Cavitation.

Abstract

This research project is part of the international master's program in Physics (plasma option) between Université de Montréal and Université Paul Sabatier - Toulouse (France). It concerns the synthesis of nanoparticles by pulsed electrical discharges in liquids. The objective is to develop the synthesis process while improving the knowledge of the formation conditions of nanoparticles. This involves characterizing the entire experimental system and developing its metrology on the one hand, and on the other hand obtaining the evolution of plasma parameters during synthesis.

Initially, at the LAPLACE lab (UMR5213), Toulouse, it was necessary to develop a pulsed electrical supply to produce discharges in liquids. Based on an existing device that, after being improved, the discharge process is characterized from the electrical point of view (current, voltage). The application of the device in the synthesis of nanoparticles was tested under different experimental conditions, considering the energy aspect (energy balance, characteristics of the discharge, etc.).

The second part was conducted at Université de Montréal, where the synthesized nanoparticles are characterized using the transmission electron microscope of Polytechnique Montreal. Also, the electrical circuit equivalent to the experimental system was determined to visualize the time evolution of the plasma parameters (Temperature and Electron Density) based on the electrical characteristics.

Keywords: Nanoparticles, Spark discharge, Equivalents circuits, Nickel, Cobalt, High Voltage Pulsed power supply, Cavitation

Table des matières

Résumé 3
Abstract 4
Table des matières 5
Liste des tableaux 6
Liste des figures 7
Liste des sigles et abréviations 10
Remerciements 11
Introduction 12
1.État plasma et Nanoparticules 13
A. L'état plasma (Généralités) 13
B. Les plasmas dans les liquides diélectriques 22
C. Les nanoparticules 29
Objectifs spécifiques du mémoire 34
2.Alimentation impulsionnelle pour la génération de nanoparticules 35
3.Détermination d'un circuit équivalent pour les décharges dans l'eau : Évolution temporelle de la densité et température électronique 43
Conclusion 53
Références bibliographiques 54
ANNEXES 58
A. « Pulser » Laplace 58
B. Synthèse d'oxide de Cobalt et de Nickel dans un film d'oxide de Cobalt par décharge « Spark » dans l'eau déionisée 62

Liste des tableaux

Chapitre 1

Tableau 1.— Mécanisme de diminution de la densité du liquide..... 24

Chapitre 3

Tableau 1.— Plasma inductance predicted by the model at varying conditions of applied voltage……47

Tableau 2.— Variation of P and τ, parameters used in the plasma conductance model, as a function of applied voltage. …… 48

Tableau 3.— Temporal variation of electron density. ……49

Annexe A

Tableau 1.— Caractéristiques de la bobine THT 58

Annexe B

Tableau 1.— Theoretical interplanar distances of the expected material (Ni, NiO, Co, CoO, and Co_3O_4)…68

Liste des figures

Chapitre 1

Figure 1.— Classifications des plasmas en fonction de leurs énergies moyennes et de leurs densités de particule [11] 14
Figure 2.— Déplacements des charges dans le plasma [13] 15
Figure 3.— Régimes de décharge : Courbes courant-tension [19] 18
Figure 4.— Claquage de Townsend : Avalanche électronique [22] 18
Figure 5.— Courbe de Paschen (tension de claquage en fonction du produit pression distance) pour différents gaz [23] 19
Figure 6.— Claquage de type streamer [29] 21
Figure 7.— Variation du délai de claquage (a) [30] : Avec différentes électrodes sous N_2 (0.1MPa / gap =1mm) (b)[32] et en fonction du rayon de courbure et de la tension appliquée dans l'huile [20] (c) 22
Figure 8.— Evolution temporelle d'une décharge dans un liquide diélectrique [34] 23
Figure 9.— Visualisation des modes de propagation d'un streamer [33] 25
Figure 10.— Evolution de la vitesse moyenne des modes de propagation des streamers dans les liquides en fonction de la tension appliquée [20] 25
Figure 11.— Evolution de l'émission en fonction du temps pour des décharges de 200ns avec des électrodes en zinc dans de l'azote liquide [41] 26
Figure 12.— Evolution de pression pour des décharges corona de 40ns (6kV) dans l'eau déionisée. [43] 26
Figure 13.— Diagramme de phase de l'eau (Etat en fonction de la pression et de la température) 27
Figure 14.— Cavitation d'une bulle crée par pulse laser E= 9mJ, dt=5,56us [46] 28
Figure 15.— Dynamique de la bulle de cavitation dans l'heptane avec des décharges de 500ns (10kV) [47] 28
Figure 16.— Etapes de synthèse de nanoparticules de taille contrôlée par réduction au NaBH4 [53] 30
Figure 17.— Synthèse de nanoparticules d'argent par irradiation UV du nitrate d'argent et de chloramine T [53] 31
Figure 18.— Synthèse de nanoparticules par impact laser sur une cible constituée d'argent [55] 32
Figure 19.— Alliage cobalt-nickel d'une particule synthétisée à l'aide d'électrodes successivement en nickel puis en cobalt dans l'azote liquide [61] 33

Chapitre 2

Figure 1.— Shematic representation of Zero Voltage Switch (ZVS) including oscillating circuit (at the left) and high voltage transmformer T1 (at the right). 36
Figure 2.— The schematic diagram of the global setup. 37
Figure 3.— The schematic diagram of electrode system. 37
Figure 4.— Evolution of the high voltage output before and after the discharge. 38
Figure 5.— Measured current for underwater discharges (U_{DC} = 50V / e_g = 0.2mm) before and after breakdown (at t = 0). 38
Figure 6.— Discharge equivalent circuit. 38
Figure 7.— Evolution of the calculated capacitance over successive disharges: (a) air, e_g = 0.5mm, U_{DC} = 20 V; (b) air, e_g = 1.0 mm, U_{DC} = 20 V; (c) water, e_g = 0.2mm, U_{DC} = 50 V. 38

Figure 8.— Least-square method to determined RLC parameter on current discharge : (a) air, e_g = 0.5mm, U_{DC} = 20 V; (b) air, e_g = 1.0 mm, U_{DC} = 20 V; (c) water, e_g = 0.2mm, U_{DC} = 50 V. ……39
Figure 9.— Influence of circuit input voltage U_{DC} on discharge electric parameter: a) deposited charge; b) breakdown voltage; c) deposited energy; d) breakdown delay with a 0.2mm gap. ……..39
Figure 10.— Influence of circuit electrodes gap e_g on discharge electric parameter: a) deposited charge; b) breakdown voltage; c) deposited energy; d) breakdown delay for U_{DC} = 50 V. ……..40
Figure 11.— Distribution of impacts diameters (U_{DC} = 50V – e_g =0.2mm). ……..40
Figure 12.— Bubble shadowgraphy: dt = 10 µs, image size: 3 by 2 mm (e_g = 0.2 mm, U_{DC} = 50 V). Discharge is visible second picture. ……41
Figure 13.— Bubble radius (experimental and calculated) and calculated pressure (e_g = 0. 3mm, U_{DC} = 50 V). ……41

Chapitre 3

Figure 1.— Scheme of the experimental setup. …… ……45
Figure 2.— Typical (a) voltage and (b) current waveforms with and without filtration (applied voltage = 15 kV and pulse width = 300 ns)……45
Figure 3.— Equivalent electrical circuit of the experimental setup. ……46
Figure 4.— Flowchart diagram of the differential equations determined for the equivalent circuits shown in Figure.3. ……46
Figure 5.— Flowchart of the program and resolution pathways.……47
Figure 6.— Simulated and measured current waveforms: a) applied voltage = 15 kV, pulse width = 200 ns and b) applied voltage = 15 kV, pulse width = 400 ns……47
Figure 7.— a) Simulated and measured current waveforms at an applied voltage of 15 kV and pulse width of 300 ns. b) Comparison between the measured voltages and those predicted using the model parameters optimized in a). ……48
Figure 8.— Temporal evolution of plasma conductance under varying conditions of applied voltage (pulse width = 500 ns). The dashed line indicates the breakdown. ……48
Figure 9.— a) Evolution of Hα line as a function of time. b) Lorentzian fit of the 700 ns Hα line. ……49
Figure 10.— Temporal evolution of electron temperature at a) r_p = 10 µm and b) r_p = 100 µm (applied voltage = 5, 10, 15, and 20 kV, pulse width = 500 ns). c) Temporal evolution of plasma radius at T_e = 0.75 eV (applied voltage = 5, 10, 15, and 20 kV, pulse width = 500 ns). The dashed line indicates the breakdown……50
Figure 11.— Electrical current waveform and its correspondence PM signal acquired for a discharge at an applied voltage of 5 kV and pulse width of 500 ns. ……50

Annexe A

Figure 1.— Circuit électronique initialement présent au LAPLACE 58
Figure 2.— Schéma de Kapp (Equivalent à un transformateur réel) 59
Figure 3.— Schéma simplifié de fonctionnement 59
Figure 4.— Circuit électronique de commutation développée par le service électronique du LAPLACE et Gilles Charles (GREMI de l'Université d'Orléans, site de Bourges) 60
Figure 5.— Schéma simplifié de la commutation 61
Figure 6.— Schéma du système actuel présent au LAPLACE (Toulouse) 62

Annexe B

Figure 1.— Experimental setup 67
Figure 2.— a) SAED pattern from TEM measurement from a Ni sample at 5kV_100ns and identification of the crystal from circular ring corresponding to the crystal D_Space. b) Relative intensity of the different crystals (Ni and NiO) from the NBS circular 539 volume 1. c) Radial profile of the experimental SAED pattern. 69
Figure 3.— Nickel and nickel oxide nanoparticles formed with 20kV-500 ns pulses 71
Figure 4.— Nickel and nickel oxide nanoparticles formed with 5kV-100 ns pulses 72
Figure 5.— SAED pattern of the nickel sample (20kV / 500ns) 73
Figure 6.— Cobalt and cobalt oxide nanoparticles formed with 20kV-500 ns pulses 74
Figure 7.— Cobalt and cobalt oxide nanoparticles created formed with 5kV-100 ns pulses 75
Figure 8.— SAED pattern of the cobalt sample (5kV_100ns) 76
Figure 9.— Nanoparticles formed by nickel (anode) and cobalt (cathode) electrodes with 20kv_500ns discharge 77
Figure 10.— Nanoparticles formed by nickel (anode) and cobalt (cathode) electrodes with 5kv_100ns discharge 77
Figure 11.— Nanoparticles formed by a cobalt (anode) nickel (cathode) with 20kv_500ns discharge. 78
Figure 12.— Nanoparticles formed by a cobalt (anode) nickel (cathode) with 5kv_100ns discharge. 79
Figure 13.— UV-visible spectrum and Tauc plot of Ni and NiO nanoparticles (Pulse width 500ns) 80
Figure 14.— UV-visible spectrum and Tauc plot of Co and Co_3O_4 nanoparticles (Pulse width 500ns) x 81
Figure 15.— UV-visible spectrum and Tauc plot of Ni /Co nanoparticles inside the cobalt oxide layer (Pulse width 500ns) (Anode: Nickel / Cathode: Cobalt) 83
Figure 16.— UV-visible spectrum and Tauc plot of Ni /Co nanoparticles inside the cobalt oxide layer (Pulse width 500ns) (Anode: Cobalt / Cathode: Nickel) 84
Figure 17.— Reconstitution of the alloy absorbance with the pure metal absorbance in the same experimental conditions 85

Liste des sigles et abréviations

LAPLACE : Laboratoire plasma et conversion d'énergie - UMR5213 (Toulouse, 31, France)

$ln\ \Lambda$: Logarithme coulombien

MET : Microscope Électronique à Transmission

n_0 : Densité des espèces neutre en (m^{-3})

PbS : Sulfure de plomb

UdeM : Université de Montréal (Montréal, QC, Canada)

UT3 : Université de Toulouse 3 : Paul Sabatier (Toulouse, 31, France)

n_0 : Densité des espèces neutre en (m^{-3})

T_e : Température électronique (eV)

Z_i : Niveau d'ionisation

η : Résistivité (Ω.m)

σ : Conductivité (S/m)

$\sigma_s^{\alpha|0}$: Section efficace de collision élections-neutre

ν_{e-i} : Fréquence de collisions électrons-ions (Hz)

ν_{e-n} : Fréquence de collisions électrons-neutre (Hz)

v_{th} : Vitesse thermique des électrons ($m.s^{-1}$)

Remerciements

Voilà une étape de plus d'accomplie, je ne saurais jamais assez remercier mes parents de m'avoir permis de réaliser les études supérieures de mon choix et de m'avoir soutenu financièrement et moralement.

Je remercie Flavien Valensi (LAPLACE ScIPRA UPS) ainsi que les équipes du LAPLACE de m'avoir accueilli lors de mon séjour au LAPLACE pour la première partie de ce projet, J.M Blaquière (LAPLACE CS) et le service électronique pour la réalisation du système de commutation de l'alimentation réalisée, ainsi que Gilles Charles (GREMI de l'Université d'Orléans, site de Bourges) qui nous a fourni une deuxième alimentation permettant des décharges plus énergétiques.

Ce fut également la découverte d'une nouvelle culture, et d'un nouveau pays : Le Canada. Malgré les difficultés que chacun a pu traverser au printemps 2020, il était agréable de vivre provisoirement dans la ville de Montréal malgré parfois les températures polaires.

Le groupe de recherche de plasma du professeur Ahmad Hamdan, malgré sa relative jeunesse, est un espace d'entraide où il est possible de s'intéresser aux projets actuellement mise en œuvre. Avec, par exemple, Kyana Mohammadi et sa maitrise sur la synthèse des nanoparticules d'argents, où nous avons pu nous entraider sur le réglage des instruments de mesures Je la remercie donc chaleureusement.

Il est également, possible de croiser, le groupe de Luc Stafford et mes deux collègues canadiens avec qui j'ai partagé cette aventure de deux ans, sans eux, il aurait été surement plus compliqué de surmonter l'isolement relatif toujours présent quand on part à l'étranger.

Je remercie également les membres jury qui vont prendre le temps de lire ce mémoire qui représente deux années de travail mise à contribution, je l'espère, d'une collaboration fructueuse entre l'université de Montréal et l'université de Paul Sabatier.

Introduction

Les premières nanoparticules n'ont pas été créées de façon volontaire, les moyens de les observer ou de les étudier étant alors inexistants. D'ailleurs, les hommes utilisent leurs propriétés depuis plus de 4 500 ans en renforçant la céramique par ajout de nanofibres naturelles ou en utilisant le sulfure de plomb (PbS) comme teinture en les synthétisant par un processus chimique. La première description scientifique de la synthèse de nanoparticules a été réalisée par Michael Faraday en 1854 qui a également comparé leurs caractéristiques optiques [1].

Les nanoparticules sont, aujourd'hui, utilisées dans de nombreuses applications modernes telles que dans l'alimentation (conservateurs, …), les cosmétiques (pigment, teinture, …) ou encore l'industrie (piles à combustibles, panneaux solaires, détection de polluants …) par changement des propriétés des matériaux. Par exemple, les propriétés bactéricides des nanoparticules d'argent sont utilisées dans les textiles pour lutter contre les mauvaises odeurs ou encore des nanoparticules d'or sont ajoutées dans le verre afin de le rendre bichromatique [2].

Ces applications variées, inquiètent de nombreux organismes, car leurs effets est encore mal connu sur la santé d'autant plus qu'il existe une grande variété de nanoparticules, que ce soit par leur taille, mais aussi par leurs constituants. Des études de l'Agence nationale de sécurité sanitaire de l'alimentation, de l'environnement et du travail (ANSES) font l'inventaire des effets connus de certains nanomatériaux, en premier lieu, il est montré que les nanoparticules ont la capacité de passer les barrières physiologiques et que certaines sont toxiques [3]. L'exemple le plus récent est le dioxyde de titane (E171) qui est interdit depuis le 1er janvier 2020 en France dans les denrées alimentaires pour donner suite à un rapport de l'Institut national de la recherche agronomique (INRA) qui démontre que des rats exposés à cette substance ont développé des cellules cancéreuses [4].

La synthèse et l'utilisation sécuritaires de ces nanoparticules est donc un enjeu de société. Comprendre leurs processus de formation et identifier leurs caractéristiques sont donc très importants pour optimiser leurs fabrications.

1.État plasma et Nanoparticules

A. L'état plasma (Généralités)

Le plasma peut être défini comme le quatrième état de la matière. Il représente l'état où les particules s'ionisent, se dissocient, il est par conséquent composé d'atomes, d'ions, d'électrons et de molécules. Électriquement neutre à une échelle macroscopique, il est l'état de la matière visible le plus commun dans l'univers (étoiles, nébuleuses...).

Il doit résulter d'un apport important d'énergie électrique, thermique ou électromagnétique. De ce fait, il est plus rare de trouver un plasma à l'état naturel. Cependant, certains événements, tels que le vent solaire, peuvent générer un état plasma dans notre atmosphère sous la forme d'aurore polaire. Un autre exemple couramment observé est la foudre causée par la décharge d'un nuage chargé (tel que le cumulonimbus).

Les caractéristiques physiques et chimiques particulières du plasma, synthétisé de façon artificielle, lui permettent d'être utilisé dans des domaines variés, tels que :

- La métallurgie pour son caractère thermique et de transfert de chaleur, principalement pour fondre les métaux dans des fours à arc. [5]
- La sécurité électrique avec les disjoncteurs qui permettent d'ouvrir un circuit électrique en opération : cette ouverture crée alors un arc électrique qui sera par la suite coupé par le dispositif. [6]
- La fabrication de composants électroniques (microprocesseurs…) par des procédés, qui par dépôt ou gravure, déposent ou enlèvent de la matière à des échelles nanométriques. [7]
- Le traitement de surface (dépôt de film, nettoyage de surface …) par des méthodes similaires avec des plasmas ayant peu de transfert thermique contrairement à la métallurgie. [8]
- Dans le domaine de la santé (stérilisation du matériel médical, traitement de plaie …) avec des procédés qui utilisent les sous-produits des plasmas tels que le rayonnement UV ou encore la dissociation de certaines molécules afin d'obtenir soit des milieux activés par plasma, soit des effets directs sur les plaies. [9]

Les plasmas et leurs compréhensions sont donc un enjeu important pour de nombreux aspects de notre société afin de comprendre et se protéger de phénomènes naturels tels que le foudroiement, mais également de développer de nouvelles technologies et procédés tels que celui de ce mémoire qui est de générer des nanoparticules.

1. Types de plasmas

Les applications industrielles des plasmas sont donc très diverses et cela est dû à la variété des plasmas qui peuvent être généré avec différentes sources d'énergies sous différentes conditions de pressions. (Figure 1)

Il est possible de classer ces différents plasmas en fonction de leur degré d'ionisation :

$$\alpha_i = \frac{n_e}{n_e + n_N} \tag{1}$$

avec n_e : la densité électronique et n_N : la densité des atomes neutres.

Celle-ci peut être très faible (de l'ordre de 10^{-10}) ou égale 1 dans le cas de milieux totalement ionisés (étoiles).

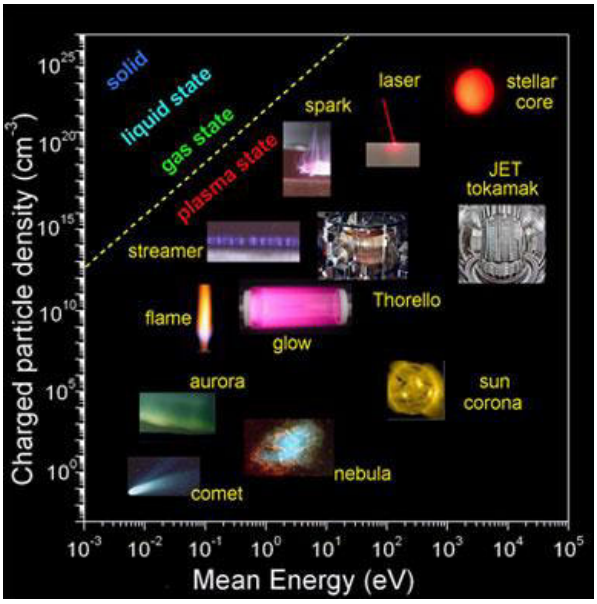

Figure 1. — Classifications des plasmas en fonction de leurs énergies moyennes et de leurs densités de particule [11]

Généralement les plasmas dit « thermiques » ont des degrés d'ionisation importants (> 0,1) et, par conséquent, les collisions électrons-atomes et surtout les collisions électrons-ions « thermalisent » le milieu conduisant à des températures importantes (plusieurs milliers de kelvins). Au contraire, les plasmas faiblement ionisés, ne sont pas à l'équilibre thermique, c'est-à-dire, que la température des électrons (ou énergie moyenne) est différente de celles des atomes et des ions.[10], [11]

2. Conductivité du milieu plasma

Le milieux plasma est constitué de particules chargées. Ces particules, en présence d'un champ électrique, vont subir la force de Coulomb et se déplacer dans le milieu créant ainsi un courant électrique dans le plasma. Seules les collisions de ces particules chargées, entre elles et avec les particules neutres vont limiter ce courant. Il peut être étudié afin de déterminer les caractéristiques microscopiques, telles que la conductance, qui sont liées aux propriétés plasmas [12]. (Figure 2)

Dans un cas simple, constitué d'un cylindre homogène de plasma soumis à un champ électrique [13], la relation reliant la conductivité électrique avec les densités des espèces chargées et leurs mobilités dans le milieu s'écrit :

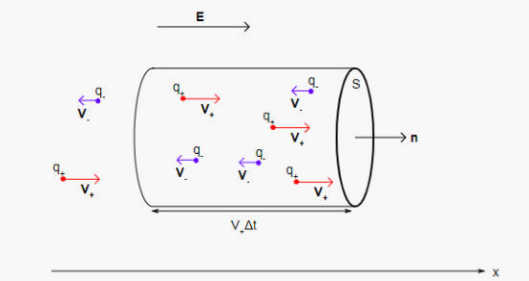

Figure 2.— Déplacements des charges dans le plasma [13]

$$\sigma = e\mu_e n_e + e\mu_i n_i \tag{2}$$

Avec e : la charge de l'électron, μ_e et μ_i : la mobilité des électrons et des ions, n_e et n_i : la densité des électrons et des ions.

Il est important de noter que la mobilité des ions étant très inférieure à celle des électrons (à cause de leur masse plus importante), le terme ionique est souvent négligé. La mobilité ionique et électronique reste à déterminer en fonction de la fréquence moyenne de collision d'un électron, soit la formule suivante :

$$\mu_e = \frac{e}{m_e \overline{\nu_e}} \tag{3}$$

Avec m_e : la masse de l'électron et $\overline{\nu_e}$: la fréquence moyenne de collision d'un électron.

Afin de déterminer cette fréquence, des hypothèses sur les fonctions de distributions en vitesse des ions et des électrons doivent être prise en compte ; il faut également connaître les sections efficaces de collision pour les collisions prise en compte.

Il est possible de considérer de multiple cas [14] :

- Un plasma totalement ionisé où les collisions électrons-ions et électrons-électrons sont majoritaires. (Collisions coulombiennes)
- Un plasma peu ionisé où les collisions électrons-atome sont majoritaires. (Collisions non-coulombiennes)
- Ou une combinaison des deux.

À la suite de la prise en compte ou non de certains types de collisions et du choix de la fonction de distributions, il est alors possible de trouver des formules de conductivité en fonction de la température (moyenne) des espèces considérées et de leurs densités.

Ainsi avec une distribution maxwellienne et en considérant une approximation à deux termes de la fonction de distribution des électrons :

$$f(v) = f_0(v) + \delta f = f_0(v) + \cos(\theta) f_1(v) \tag{4}$$

Avec

$$f_0(v) = (2\pi v_{Te}^2)^{-3/2} \exp\left(-\frac{v^2}{2v_{Te}^2}\right) \tag{5}$$

Avec v_{Te} : la vitesse thermique moyenne des électrons

Et par la résolution de l'équation de Boltzmann pour un état stationnaire et homogène : [15]

$$-\frac{eE}{m_e} \cdot \frac{\partial f_0(v)}{\partial v} = I_c(\delta f) \tag{6}$$

Avec E : le champ électrique appliqué, $f(v)$: la fonction de distribution des électrons et I_c l'intégrale de collision. Ici : $I_c(\delta f) = \nu(v)\delta f(v)$ (7)

il est possible de déterminer la vitesse de dérive des électrons (qui détermine le courant et donc la résistivité du plasma):

$$\bar{v} = \int v\, f(v) dv = \int v\, \delta f(v) = -\mu_e E \tag{8}$$

$$\text{Soit : } \delta f = \frac{\cos(\theta) eE v f_0(v)}{m_e v_{Te}^2 \nu(v)} \tag{9}$$

Le calcul de la mobilité électronique est alors réalisé :

$$\mu_e = \frac{e}{T}\int \frac{v^2 f_0(v)}{\nu(v)} cos(\theta) dv\, d\theta \tag{10}$$

En fonction du type de collision réalisée, on obtient alors des fréquences de collision différentes, par intégration sur l'ensemble des angles et des vitesses. Dans le cas des collisions électron-neutre :

$$\bar{\nu}_{en}(v) = \frac{3\sqrt{2\pi}}{4} n_a \bar{q}(T) v_{Te} \tag{11}$$

Avec $\bar{q}(T)$ la section efficace de collision de l'atome et n_a la densité de l'espèce neutre.

Dans le cas des collisions électron-ion :

$$\bar{\nu}_{ei}(v) = \frac{\pi^{\frac{3}{2}}}{4\sqrt{2}} \left(\frac{Ze^2}{k_b T_e}\right)^2 n_i v_{Te} \ln \Lambda \tag{12}$$

Avec T_e : la température électronique et $ln\,\Lambda$: le logarithme coulombien, n_i la densité de l'espèce ionisée et Z le niveau d'ionisation.

Dans notre cas, pour des décharges d'une centaine de nanosecondes, on négligera les collisions électrons-neutres à cause de la densité électronique importante présente dans le milieu (voir plus loin, chapitre 3 p43). Cela revient donc à obtenir l'équation de résistivité de « Spitzer » en considérant les espèces une fois ionisées [16] :

$$\eta\ (\Omega.m) = \frac{1}{1.53e{-}4} * \frac{ln\,\Lambda}{T_e^{3/2}} \tag{13}$$

3. Les types de claquage

Afin d'atteindre l'énergie nécessaire à la création d'un plasma, de nombreuse méthodes sont disponibles telles que générer des micro-ondes concentrées en un point de l'espace [17] ou encore de focaliser des impulsions laser sur une cible [18], mais nous allons nous attarder sur les méthodes électriques.

Un apport d'énergie électrique suffisant doit être obtenu. Il est alors possible de soit utiliser un matériau conducteur auquel on fournira un courant important afin que celui-ci se vaporise et

s'ionise par effet Joule, soit d'appliquer une tension importante aux bornes d'un diélectrique afin qu'un canal conducteur soit créé : il s'agit d'un claquage électrique.

Un claquage peut se produire de deux façons distinctes :

- Par claquage de Townsend
- Par claquage Streamer

Ces deux mécanismes sont très différents l'un de l'autre et conduisent à des types de décharges différentes [19], [20]. (Figure 3)

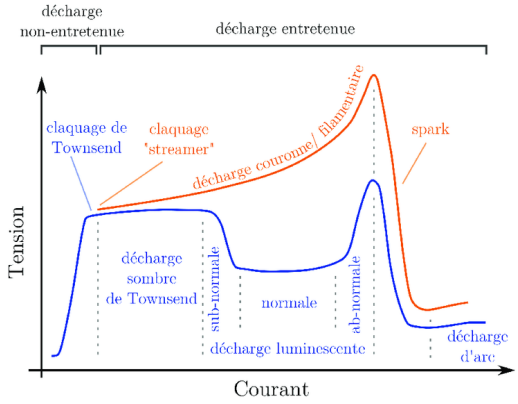

Figure 3.— Régimes de décharge : Courbes courant-tension [19]

Le claquage de type Townsend se déroule généralement à basse pression où la densité atomique est faible, de ce fait, la charge d'espace créée par le front d'ionisation est faible et n'a que peu d'influence sur le champ électrique appliqué. Au contraire, à plus haute pression, la charge d'espace est non négligeable et doit être prise en compte [20].

a. Claquage de Townsend

Lors de l'application d'une tension aux bornes d'un espace gazeux, un champ électrique est créé. La présence d'un électron libre (celui-ci peut avoir différentes origines telles que l'échauffement de la cathode, ou le rayonnement cosmique…[21]) dans cet espace enclenche alors le processus de claquage.

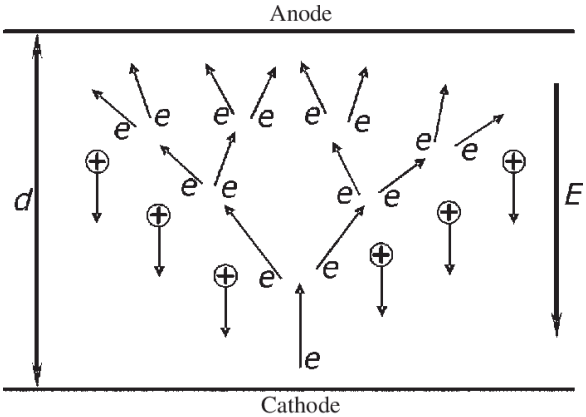

Figure 4.— Claquage de Townsend : Avalanche électronique [22]

Cet électron libre va alors être accéléré par le champ électrique présent, en direction de l'anode en réalisant des collisions avec des atomes/molécules présents dans l'espace inter-électrodes. Ces atomes vont s'ioniser (si l'énergie transmise par ces électrons dépasse le seuil

d'ionisation de l'atome) et créer des ions et des électrons. Les électrons, plus mobiles que les ions, vont continuer à ioniser le milieu jusqu'à atteindre l'anode (avalanche électronique) tandis que les ions, se dirigeant alors vers la cathode, vont créer des électrons secondaires à son contact et le processus se répète alors avec les électrons secondaires [20], [22]. (Figure 4)

On appelle alors le 1er coefficient de Townsend (nommé α), le nombre qui exprime la quantité moyenne d'électrons formés dans le gap par un électron par unité de longueur. Tandis que le second coefficient de Townsend (nommé γ) correspond au nombre moyen d'électrons émis à la cathode par collision d'un ion avec celle-ci.

La décharge est entretenue si le nombre d'électron généré (par processus α ou γ) est supérieur au nombre d'électrons perdu par recombinaison à l'anode (ou dans le gap), soit la condition suivante :

$$\gamma(\exp(\alpha d) - 1) = 1 \tag{14}$$

α étant relié aux paramètres fondamentaux du gaz, il est possible d'obtenir une courbe donnant la tension minimale de claquage en fonction du produit pression-distance [23], [24]. Cette courbe est appelée courbe de Paschen et comporte un minimum (Figure 5) :

$$V_{claquage} = \frac{Bpd}{\ln\left(\frac{A}{\ln\left(1+\frac{1}{\gamma}\right)}\right)+\ln(pd)} \tag{15}$$

A et B sont des constantes propres au gaz tandis que γ dépend du matériau de la cathode [25].

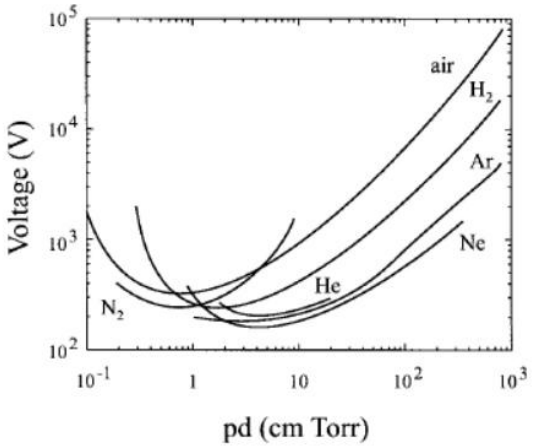

Figure 5. — Courbe de Paschen (tension de claquage en fonction du produit pression distance) pour différents gaz [23]

b. *Claquage de type Streamer*

Pour le claquage de type streamer, le début de la décharge est similaire qu'un claquage de type Townsend : un électron libre va déclencher une avalanche électronique, les électrons étant plus rapides que les ions, ils sont rapidement absorbés par l'anode tandis que les ions lents forment une charge d'espace positive. Cette charge d'espace produit un champ qui peut être du même ordre de grandeur que le champ appliqué et va alors contribuer à son amplification là où les électrons ont disparu.

Ce type de claquage est décrit par la théorie streamer-leader proposé par Meek et Loeb [26], [27] et par Reather [28] en 1940. Ce type de décharge est obtenu par augmentation du champ afin d'atteindre $\exp(\alpha d) > 10^8$ (avec α le 1er coefficient de Townsend et d la distance inter-électrode). La charge d'espace n'est alors plus négligeable et la photoionisation joue un rôle important.

Des électrons secondaires sont également émis par photo ionisation à l'abord de la charge d'espace. Ces électrons forment alors d'autres avalanches électroniques. La charge d'espace renforce ainsi le champ dans le gap. Les avalanches secondaires (causées par la photoionisation) permettent de multiple front d'ionisation qui se propage dans l'espace inter électrodes. Lorsque le streamer touche la cathode, le claquage se produit [20], [29]. (Figure 6)

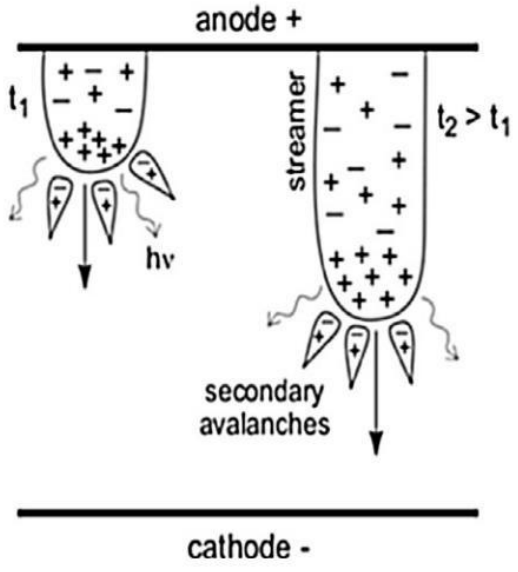

Figure 6. — Claquage de type streamer [29]

c. *Claquage sous tension de choc (impulsionnel)*

Dans le cas où le champ appliqué n'est pas continu, mais impulsionnel, d'autres éléments sont à considérer. En effet, la présence d'un électron libre à un endroit précis de l'espace est aléatoire car créée arbitrairement par le rayonnement cosmique ou la radioactivité terrestre. Par conséquent, si le temps d'une alternance est suffisant pour l'apparition d'un électron libre (et la tension appliquée suffisante) alors le claquage aura lieu.

Dans le cas contraire, si l'impulsion est brève (< 1 µs), la probabilité qu'un électron libre soit présent est faible et il se peut que le claquage ne se produise pas même si la tension appliquée est supérieure à la tension de claquage « en continu » [20].

Il est donc possible d'appliquer une tension supérieure à la tension de claquage théorique sans que le claquage ait lieu immédiatement, il peut être visualisé avec un retard ou ne pas être observé si l'impulsion est d'une largeur trop courte.

En figure 7,des études montrent l'influence de certains paramètres sur ce délai avant claquage et sur la probabilité de celui-ci [21], [30]–[32] dans différents milieux tels que les gaz ou les liquides diélectriques.

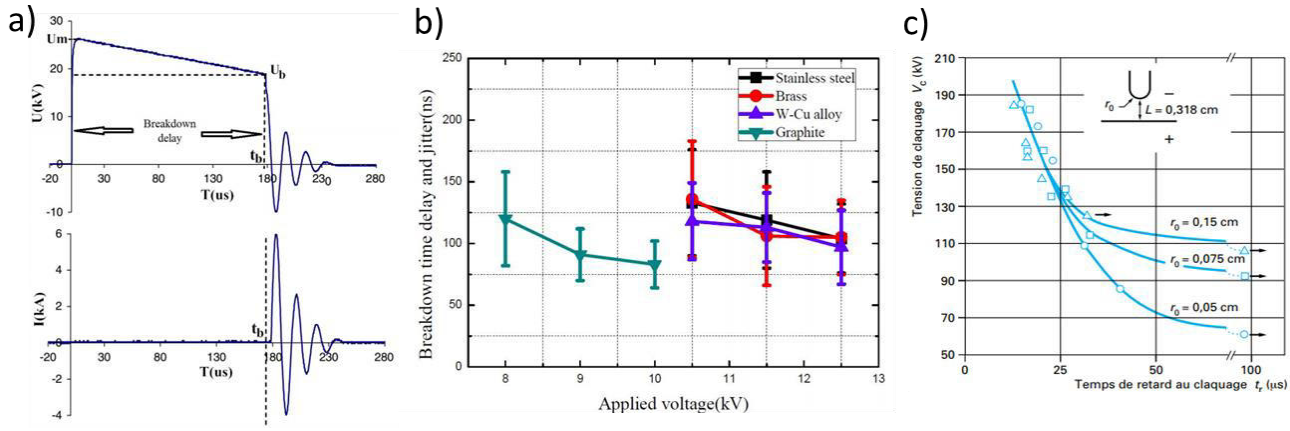

Figure 7.— Variation du délai de claquage (a) [30] : Avec différentes électrodes sous N_2 (0.1MPa / gap =1mm) (b)[32] et en fonction du rayon de courbure et de la tension appliquée dans l'huile [20] (c)

En fonction de la durée de l'impulsion, il est également possible de limiter le passage à l'arc ou la thermalisation du plasma. Ainsi, pour des impulsions inférieurs à 1 µs, la température électronique et la température des atomes et ions ne seront pas les mêmes [33] car les électrons ne parviennent pas à transférer leurs énergies dans le temps imparti.

B. Les plasmas dans les liquides diélectriques

Bien qu'étudiés dans les phénomènes liés à l'électrolyse depuis plus d'un siècle à la suite de leur découverte lors de ce processus, les plasmas dans les liquides sont encore assez mal compris et modélisés du fait de la difficulté d'obtenir des données fiables dans ces milieux [34]. La raison est que la pureté du liquide et la quantité de gaz dissous a une grande influence sur le processus de claquage [35].

Les études des décharges dans les liquides diélectriques ont été ensuite poursuivies dans le cadre de leurs applications dans les disjoncteurs. Le disjoncteur à huile, par exemple, est un moyen simple et économique de couper des tensions allant de 5 à 150 kV [36].

Des activités et procédés ont été alors mis en pratique, à la suite des observations réalisées sur ces décharges, tels que l'électroérosion, la fracturation des roches, ou encore la synthèse d'explosifs [37].

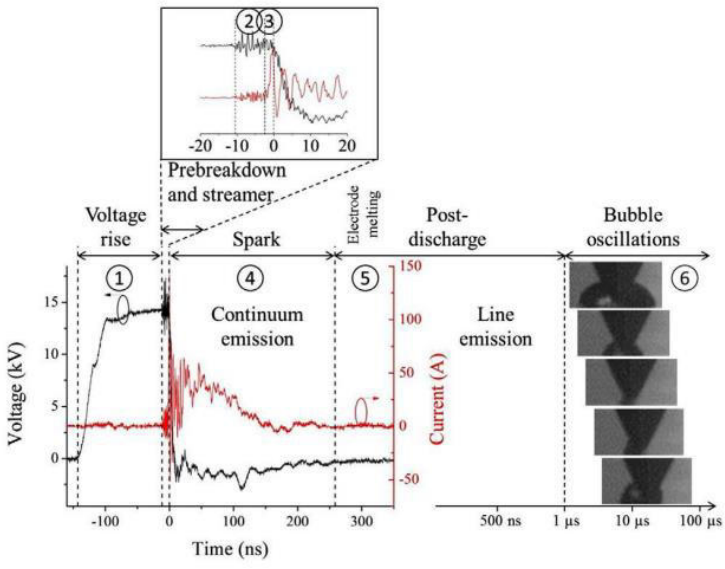

Figure 8.— Evolution temporelle d'une décharge dans un liquide diélectrique [34]

Nous nous focaliserons sur les décharges impulsionnelles d'une centaine de nanosecondes. (Figure 8)

Comme indiqué dans la partie précédente, le claquage d'un diélectrique gazeux est dans le cas d'une décharge électrique issu de l'application d'un fort potentiel électrique. Le gaz a alors perdu ses caractéristiques isolantes. Il se passe un phénomène similaire lors des

décharges dans les liquides diélectriques, cependant des différences sont à préciser :

- Une étape de pré claquage est nécessaire afin d'initier le streamer, durant cette étape d'injection de charge, la tension appliquée oscille avec une amplitude faible (centaines de volts) juste avant de s'effondrer.
- Lors de la décharge, le liquide environnant, absorbe et réémet un rayonnement. Le milieu ne peut pas être considéré optiquement « mince ».
- La présence d'une bulle gazeuse peut être observée, celle-ci ayant une dynamique bien plus lente que celle de la décharge.

1. Montée en tension

Les milieux liquides étant bien plus denses que les milieux gazeux, le libre parcours moyen des particules chargées est plus faible et conduit à l'impossibilité pour les charges de gagner assez d'énergie pour ioniser les autres particules [35].

Le temps en montée (ou « rise time » en anglais) de la tension à une importance sur les processus mis en jeu lors du claquage du liquide [38], il existe alors deux mécanismes qui provoquent ce claquage :

- La formation de microbulles de gaz par effet thermique de chauffage du liquide environnant, la densité des espèces est alors plus faible et le claquage peut avoir lieu [39]. (Temps de montée de la tension > 100 ns)
- Ou bien la formation d'une onde de pression par électrostriction (Déformation d'un diélectrique à l'aide d'un champ électrique) qui change la densité du liquide localement [40].

Tableau 1.— Mécanisme de diminution de la densité du liquide

	Temps de montée	Mécanisme de diminution de la densité du liquide
Dispositif du LAPLACE	≈ 10^{-5} s	Microbulle
Dispositif de L'UdeM	≈ 10^{-8} s	Électrostriction

Le tableau 1, ci-dessus, montre alors que les dispositifs du LAPLACE et de l'UdeM auront des mécanismes de claquage différents. D'autres phénomènes sont également proposés tels que la dissociation des molécules du liquide par le champ électrique appliquée [34].

La polarité de la tension appliquée a également une importance sur les parts de chaque phénomène : la géométrie du streamer est également modifiée, le retard avant la décharge change. Ainsi, la tension de claquage est plus faible pour une tension appliquée positive que négative dans une configuration pointe plan. [13]

2. Préclaquage et streamer

Les streamers peuvent être subdivisés en plusieurs catégories selon leur vitesse et leur polarité (Figure 9) :

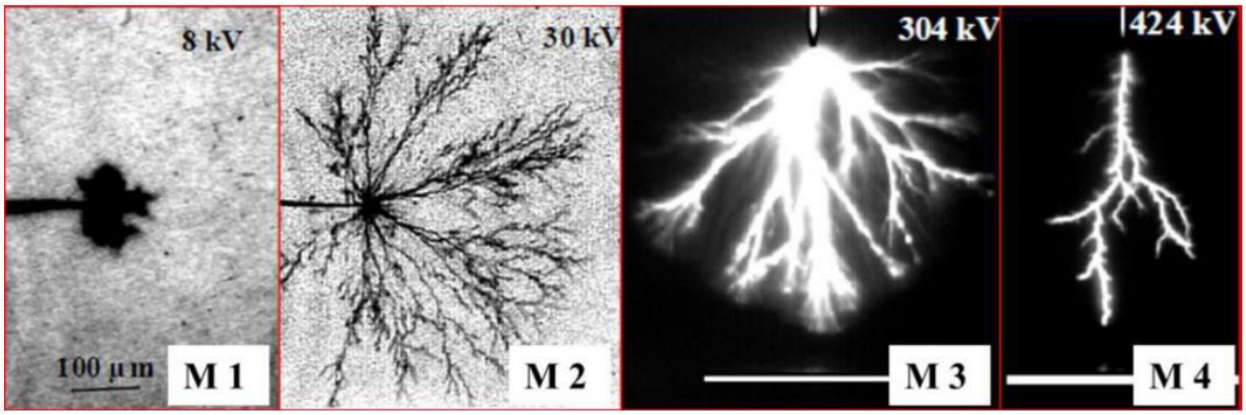

Figure 9.— Visualisation des modes de propagation d'un streamer [33]

- Les streamers lents appelés également « streamer primaire » apparaissent à des amplitudes faibles. Ils ont une longueur typique de l'ordre de la centaine de micromètres qui peuvent être très arborescente (Figure 9, image M2) ou hémisphérique (Figure 9, image M1). Ils ont une vitesse de propagation d'une centaine de m/s à quelques km/s.

- Les streamers rapides appelés également « streamer secondaire » apparaissent au-delà d'un certain seuil de tension (déterminé par la géométrie de chaque système). Ils sont plus rapides (10 à 100 km/s) et ont souvent des structures arborescentes (Figure 9, images M3 et M4).

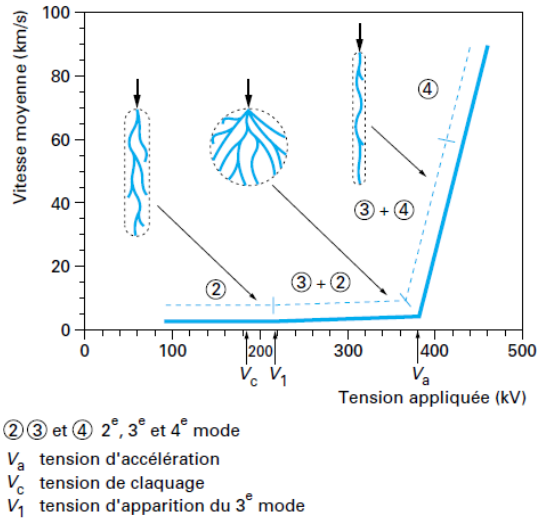

②③ et ④ 2e, 3e et 4e mode
V_a tension d'accélération
V_c tension de claquage
V_1 tension d'apparition du 3e mode

Figure 10.— Evolution de la vitesse moyenne des modes de propagation des streamers dans les liquides en fonction de la tension appliquée [20]

Une classification en quatre modes a été réalisée par Hebner et Lesaint [21] en catégorisant leur vitesse de propagation plus finement et leurs nombre de fronts ionisants (arborescence). (Figure 10)

Ce streamer est issu du transport des charges déposées durant le préclaquage par différents mécanismes d'injection de charge tels que l'émission d'électrons d'Auger [34]. Ces charges injectées, dans le cas d'un streamer lent, provoquent des avalanches électroniques dans les différentes bulles de gaz présentes ou directement dans le liquide.

Ce phénomène continue jusqu'à ce que la tension appliquée soit suffisante pour que la succession de bulles claque ou que le champ appliqué soit assez grande pour qu'un streamer rapide soit formé.

Le streamer rapide se propage par vaporisation de l'eau autour de lui jusqu'à atteindre l'autre électrode, ainsi des distances plus importantes peuvent être parcourues comparativement aux streamers lents [35].

3. Spark

Pour donner suite à cette décharge, la formation de plusieurs types de plasmas sont alors possibles :

- Une décharge partielle (semblable à une décharge corona) où seuls des streamers sont visibles.
- Une étincelle, « Spark » ou décharge électro hydraulique (canal conducteur sans équilibre thermique)
- Un arc (canal conducteur en équilibre ou proche de l'équilibre thermique)

Si la tension appliquée est insuffisante pour que le streamer puisse franchir l'espace inter électrodes, on se trouve dans le premier cas, la décharge ne peut pas créer un canal ionisé entre les deux électrodes [37].

Sinon, ce canal se crée et une étincelle est alors présente entre les deux électrodes, si ce canal est soumis à une impulsion de plus de 1 µs avec un courant important alors le plasma transitionne dans le régime d'arc.

Un continuum lumineux est alors observable causé par la désexcitation des espèces du plasma. Ce continuum est issu, en grande partie de la recombinaison électrons-ions, l'émission de Bremsstrahlung et l'émission de corps noir tandis que les raies d'émission atomique sont noyées dans le fond continue. [41] (Figure 11)

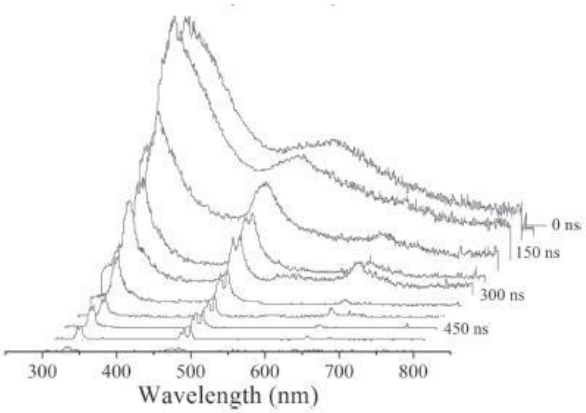

Figure 11.— Evolution de l'émission en fonction du temps pour des décharges de 200ns avec des électrodes en zinc dans de l'azote liquide [41]

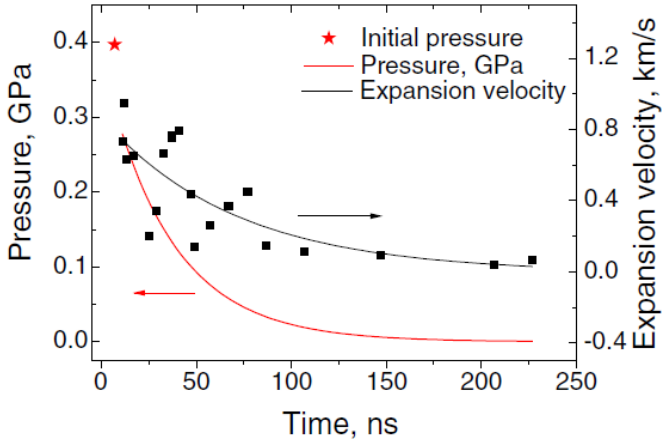

Figure 12.— Evolution de pression pour des décharges corona de 40ns (6kV) dans l'eau déionisée. [43]

La puissance instantanée reçue (de l'ordre du kW) ionise le milieu ce qui génère des ondes de pression par l'expansion du plasma dans le milieu [34]. Ces ondes de pression peuvent être étudiées afin de déterminer la pression au moment de la décharge. Ainsi, des estimations de quelques centaines de MPa sont obtenues dans l'eau déionisée. [42]

Cependant, il faut noter que cette pression évolue très rapidement par l'expansion et le refroidissement de la décharge : il est possible de passer d'une pression initiale de plusieurs centaines de MPa à quelques MPa en 200 ns. [43] (Figure 12)

4. L'après décharge

À la suite de la décharge, la tension devient nulle et le courant ne circule plus à travers le plasma d'une façon ordonnée, le plasma va se refroidir. Un puit de métal liquide s'est formé par effet joule à la surface des électrodes et par transfert thermique du plasma. La matière ablatée (sous forme de vapeur ou par éjection de gouttelette) est alors refroidie par expansion de la bulle de vapeur et se solidifie, une partie de la masse est alors redéposée sur les électrodes.[44]

En ce qui concerne la radiation, son intensité chute et le rayonnement observable passe d'un continuum à un spectre de raie issu des éléments du liquide et des électrodes (Figure 11) [34].

5. Cavitation

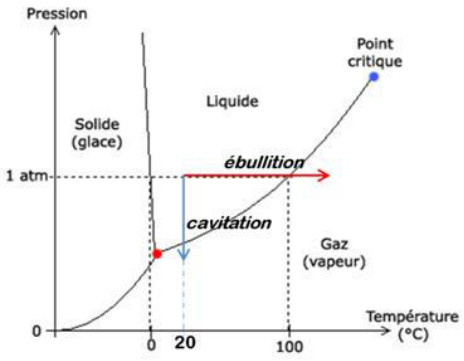

Figure 13.— Diagramme de phase de l'eau (Etat en fonction de la pression et de la température)

Lors de la décharge dans un liquide, le plasma issu du claquage vaporise une partie du liquide présent et une partie des électrodes. Ce gaz partiellement ionisé est donc entouré de liquide, une bulle est formée. Cette bulle de gaz a une pression supérieure à la pression ambiante avec un rayon faible de l'ordre de la centaine de micromètres : cette bulle est nommée bulle de cavitation [45] car elle va caviter (s'expandre puis se contracter) autour de la pression environnante. (Figure 13)

La bulle sous pression va donc s'étendre et sa pression diminue jusqu'à ce qu'elle soit égale à celle exercée par le liquide extérieur. Cependant, compte-tenu de l'inertie du phénomène, la bulle continue son expansion et sa pression diminue encore et devient inférieure à celle du liquide. L'expansion cesse finalement et la bulle va se contracter dû à sa sous-pressurisation, ce qui va avoir pour effet d'augmenter à nouveau la pression à l'intérieur. De même, du fait de l'inertie, la pression va à nouveau dépasser celle du liquide, causant une nouvelle expansion et ainsi de suite. Évidemment, le phénomène est amorti et le diamètre maximal de la bulle après chaque expansion va progressivement diminuer jusqu'à que sa pression interne soit à l'équilibre avec le milieu externe. (Figure 14)

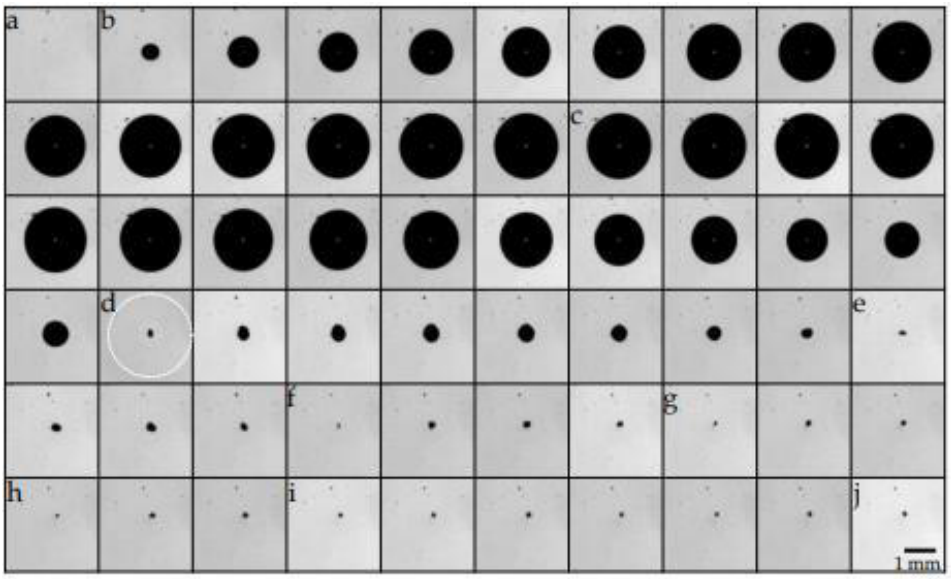

Figure 14.— Cavitation d'une bulle crée par pulse laser E= 9mJ, dt=5,56us [46]

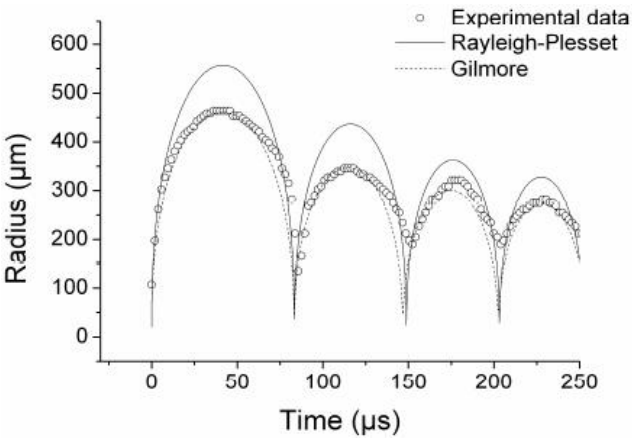

Figure 15.— Dynamique de la bulle de cavitation dans l'heptane avec des décharges de 500ns (10kV) [47]

Ces oscillations peuvent être décrites par l'équation de Rayleigh-Plesset qui décrit la dynamique d'une bulle gazeuse dans un liquide incompressible ou par l'équation de Gilmore si la compressibilité du liquide doit être prise en compte. C'est ce qui se produit quand la vitesse d'expansion de la bulle n'est pas négligeable par rapport à celle de la vitesse du son dans le liquide [37], [46], [47]. (Figure 15)

La dynamique de cette bulle est très lente par rapport à celle de la décharge (quelques centaines de microsecondes versus quelques centaines de nanosecondes) ce qui limitera la fréquence de répétition utilisable à 1 kHz lors de la synthèse des particules afin d'avoir des conditions de décharge similaire pour chaque décharge.

C. Les nanoparticules

Le terme « nanoparticules » désigne des objets dont les trois dimensions se situent à l'échelle nanométrique (entre 1 et 100 nm). Ils font partie de la catégorie des nanomatériaux définis par la Commission européenne en 2011 et par la norme ISO TS 8004-1.

Les nanomatériaux sont répartis en deux catégories [48] :

- Les **nano-objets** qui regroupent :
  - Les nanoparticules
  - Les nanofibres, nanotubes, nanofilament
  - Les nano-feuillets, nano-plaquette
- Les matériaux **nanostructurés :**
  - Les agrégats et agglomérats de nano-objet
  - Les nanocomposites
  - Les matériaux nanoporeux

Leurs applications dans de nombreux domaines sont liées à deux avantages : malgré leurs petites tailles, ces particules peuvent garder des propriétés similaires à celle de leurs matériaux massifs correspondant, mais en offrant un rapport surface/volume beaucoup plus important. Cela permet, par exemple, de réduire l'épaisseur d'un traitement de surface et par conséquent d'utiliser moins de matières premières [49].

Le second avantage est l'apparition de nouvelle propriété si le diamètre des nanoparticules est assez faible (propriétés catalytiques, des températures de fusion plus faible, …) [50].

Malgré leurs larges utilisations dans la vie quotidienne, celles-ci peuvent se révéler toxiques ; cependant chaque nanomatériau, même pour une composition identique, à un profil toxicologique propre. Il n'est pas possible d'émettre une hypothèse générale [48].

1. La synthèse des nanoparticules

La génération de nanoparticules est donc un enjeu, c'est pourquoi de nombreuses recherches sont réalisées dans ce domaine. De nombreux procédés existent, souvent efficaces sur un type précis de nanoparticules ou pour une composition fixée. Des procédés physiques, chimiques ou encore biologiques sont donc en compétition, dans l'exemple des nanoparticules d'argent [51], des méthodes telles que l'ablation laser, l'irradiation gamma/électronique, la réduction chimique ont été développées.

Nous prendrons l'exemple des nanoparticules d'argents qui sont les particules les plus étudiés dû aux nombreuses applications qui leurs sont attribuées. [52]

a. Réduction chimique

La réduction chimique est l'approche la plus commune pour générer des nanoparticules d'argent, elle s'effectue par des agents de réduction organique et inorganique tels que l'hydrogène ou le $NaBH_4$ avec du nitrate d'argent. (Figure 16)

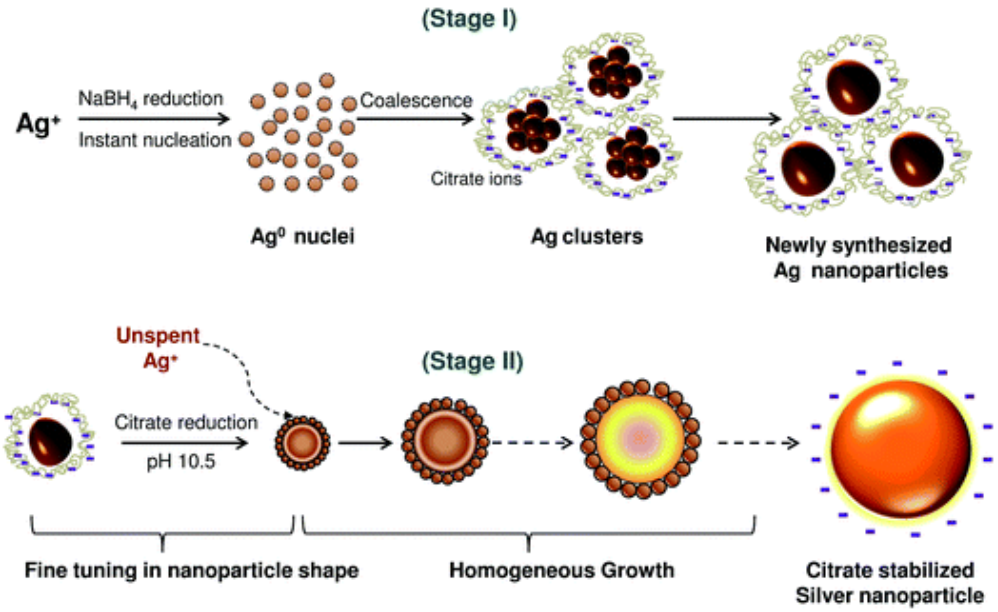

Figure 16.— Etapes de synthèse de nanoparticules de taille contrôlée par réduction au NaBH4 [53]

Dans le procédé ci-dessus, le $NaBH_4$ est utilisé comme réducteur primaire du nitrate d'argent tandis que le Trisodium Citrate (TSC) est utilisé comme réducteur secondaire et comme agent stabilisant.

Des étapes postérieures en changeant le PH de la solution peuvent être ajoutées afin de contrôler la taille et la forme des nanoparticules [53].

b. <u>Irradiation</u>

Des nanoparticules peuvent également être obtenues par différentes méthodes d'irradiation telles que l'irradiation laser/UV, par rayonnement micro-ondes ou par rayonnement gamma.

Les techniques basées sur l'irradiation, comme l'ablation laser, fonctionnent sans l'ajout de produits chimiques, potentiellement dangereux pour l'environnement (e.g. $NaBH_4$). Cependant la problématique de purification/récupération de ces particules est toujours présente.

Dans l'exemple de l'irradiation UV, il est possible de réaliser des nanoparticules d'argent à l'aide de chloramine T et de nitrate d'argent. (Figure 17)

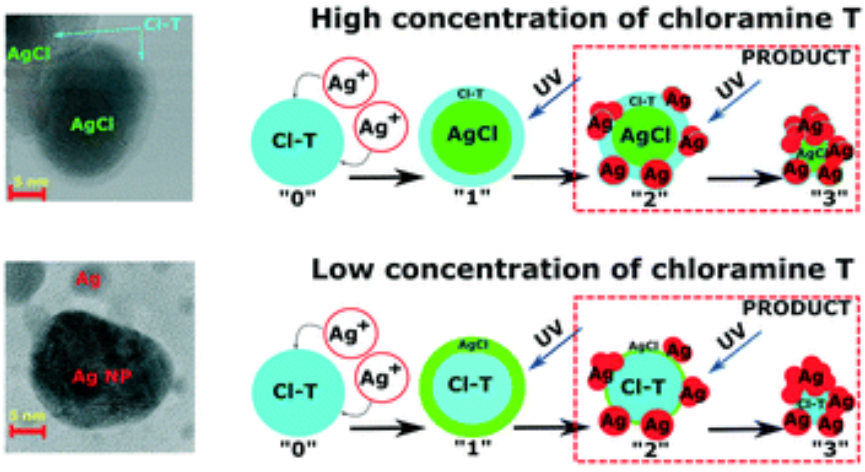

Figure 17.— Synthèse de nanoparticules d'argent par irradiation UV du nitrate d'argent et de chloramine T [53]

La concentration de chloramine T permet alors soit de générer des nanoparticules d'argent (basse concentration), soit une structure cristalline de AgCl (haute concentration). [55]

L'ablation laser fonctionne par l'irradiation d'un matériau désiré à partir d'un laser qui vaporise une partie du matériau dans la solution. Le principal avantage de cette méthode est l'absence d'agent chimique, ce qui permet d'obtenir des nanoparticules d'une grande pureté. (Figure 18)

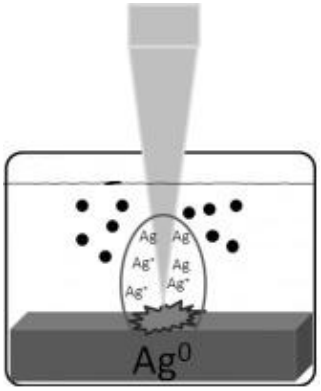

Figure 18.— Synthèse de nanoparticules par impact laser sur une cible constituée d'argent [55]

Le rendement de cette méthode est influencé par de nombreux paramètres tels que la longueur d'onde du laser ou encore la durée de l'impulsion. Ainsi avec des impulsions lasers femtosecondes, le rendement est plus faible, mais le diamètre des particules est moins dispersé que pour des impulsions lasers nanosecondes.

Le choix du solvant est également important, cela a un effet sur l'efficacité du processus, mais également sur les réactions chimiques qui peuvent avoir lieu entre les particules créées [55].

c. <u>Décharges électriques</u>

D'autres méthodes existent également, telles que les décharges hydroélectriques que nous étudierons ici. Ces décharges, comme les méthodes d'ablation par irradiation laser, ont pour avantage la possibilité de choisir le liquide dans lequel les particules seront déposées et ainsi permettre leurs récupérations ou leurs utilisations dans d'autres procédés simplement. Cependant, l'accessibilité de ces méthodes et leurs coûts sont également à prendre en compte pour démocratiser un procédé, c'est pourquoi, le choix de réaliser des décharges électriques dans les liquides s'est imposée : il est, en effet, relativement simple et moins coûteux de produire des nanoparticules par des décharges dans les liquides.

Dans un milieu gazeux, des éléments de réponse peuvent être trouvés sur l'influence des paramètres électriques sur les particules créées tels que la variation de la distribution en taille des particules par rapport à l'énergie déposée [56], le type de décharge [57], le type d'électrodes ou gaz [58]. Si dans les liquides le nombre de paramètres étudiés rend difficile

l'établissement d'une loi générale, pour de nombreux travaux, on note des similitudes avec les décharges dans les gaz.[59]

Bien que la synthèse de nanoparticule soit admise dans ce type de décharge (dans les liquides ou les gaz) et réalisé de façon relativement simple, l'étude des phénomènes de formations et les paramètres nécessaire à la synthèse de particules complexes de façon systématique reste encore mal maitriser. Cependant, des nanoparticules complexes, telles que des alliages métalliques [60] (Figure 19), des particules « core-shell » ou encore des particules ayant une nouvelle phase cristallographique, sont réalisables [61].

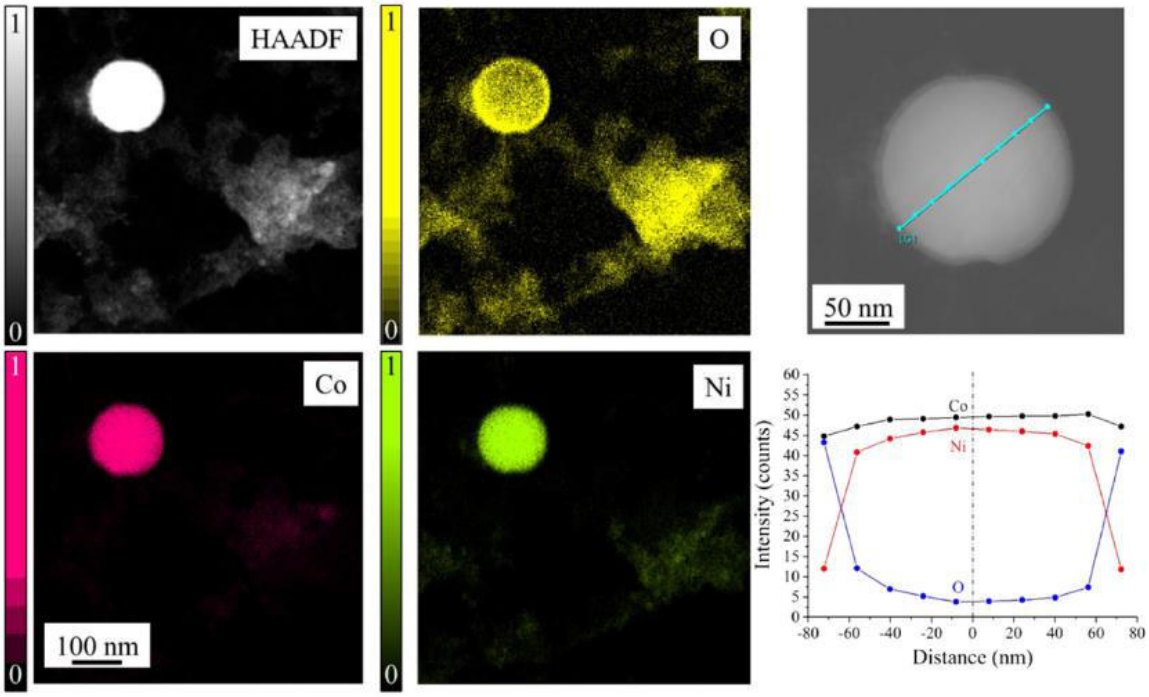

Figure 19.— Alliage cobalt-nickel d'une particule synthétisée à l'aide d'électrodes successivement en nickel puis en cobalt dans l'azote liquide [61]

Objectifs spécifiques du mémoire

À la suite de la revue scientifique réalisée à Toulouse (qui fût par la suite complété), l'objectif initial du projet de recherche fût de réaliser un dispositif expérimental économique et simple à mettre en œuvre afin de réaliser des décharges « Spark » dans un liquide diélectrique ; il s'agira du chapitre 2 p.35. Il s'agissait de réaliser des analyses élémentaires, à Toulouse, afin de lancer la collaboration sur le sujet de la synthèse de nanoparticules par ce type de procédée. Ainsi, il a été possible de réaliser des décharges similaires à ce qui se faisait déjà à l'université de Montréal.

Puis à la suite de mon arrivée à Montréal et à l'accès à un dispositif expérimental plus stable (dans l'énergie injectée ou la durée des décharges), des études plus poussées sur les paramètres plasma des décharges réalisées ont pu être réaliser. Ainsi, l'influence des paramètres électriques sur les caractéristiques du plasma sera mise en évidence par observation indirecte à l'aide d'un circuit équivalent du dispositif expérimental et par spectroscopie d'émission optique. Il est alors possible de remonter à une évolution temporelle de la température électronique : il s'agira du chapitre 3 p.43.

En annexe B (p.62.), grâce à des résultats préliminaires, il sera possible de constater que ces paramètres électriques n'ont que peu d'influence, sur la plage de variation choisie, sur les caractéristiques morphologiques des particules de cobalt et de nickel synthétisées par décharge « Spark » dans de l'eau déionisée. Les particules synthétisées sont alors analysées par microscope électronique à transmission et par spectroscopies d'absorption UV-Visible. Ces équipements sont facilement utilisable grâce à la proximité de l'école polytechnique de Montréal et de L'UdeM.

2.Alimentation impulsionnelle pour la génération de nanoparticules

Dans le premier chapitre, les décharges « Sparks » et les phénomènes de claquages ont été introduits. Dans ce chapitre, nous caractériserons les décharges produites par l'alimentation développée au LAPLACE par des mesures électriques et optiques. Le fonctionnement de cette alimentation, les schémas électriques et les améliorations réalisé sont disponibles dans l'annexe A de ce mémoire.

À partir de ces mesures électriques, le rendement de l'alimentation sera déterminé sur plusieurs points de fonctionnement. Tandis que les observations des changements sur les électrodes et la formation d'une bulle de « cavitation » nous permettrons de remonter à la masse ablatée et à la pression dans le milieu, respectivement. Les résultats sont présentés sous la forme d'une publication scientifique faisant l'objet d'une soumission au journal IEEE Transaction on Plasma Science. (TPS13044)

Dans cette publication, T. Merciris a participé à la mise au point du système expérimental, a réalisé l'ensemble des mesures, la majorité de l'analyse et la réaction du premier jet de l'article. Les co-auteurs ont participé à l'analyse des résultats et à la mise en place du système expérimental, à l'analyse des résultats et à la rédaction de l'article.

Simplified Spark Pulser for Nanoparticles Generation

Thomas Merciris, Ahmad Hamdan, Audren Dorval, and Flavien Valensi

Abstract— **This paper studies the possibility to design high voltage pulser to sustain spark discharges in dielectric liquid using cheap and simple design. A spark pulser based on a zero voltage switch oscillating circuit is used to power a high voltage transformer. Sparks are ignited between copper electrodes in deionized water. The influence of input voltage and electrode gap on voltage and delay before breakdown, deposited charge, and energy is discussed. The effect of a spark gap device is also studied. Discharge electric characteristics are used to determine the capacitance and inductance of generator, through modelling of the equivalent electrical circuit. The utilization of the pulser in nanoparticles synthesis is evaluated by estimating the electrode erosion rate. In addition, the cavitation bubble generated by the spark is used to determine pressure of the medium in which the spark and nanoparticles formation occur. Results show that the operation is similar to other setups.**

Index Terms— **zero voltage switch (ZVS), spark discharge, nanoparticles, deionized water, discharge circuit.**

I. Introduction

Electrical discharges in dielectric liquids are studied since multiple decades, but their understanding is difficult and depends on numerous parameters [1]. The generation of nanoparticles by sustaining DC arcs in liquids is efficient and low-cost. Multiple electrical circuit architectures can be used to generate high voltage spark discharges. The use of a capacitive discharge allows to produce high voltage pulses shorter than one microsecond at few hundreds of Hertz ([2], [3]). On the other hand, DC power supplies with the assistance of a high voltage switch permit to have pulses of few nanoseconds ([4], [5]) with frequency up to the kHz range. Then the initial investment for nanosecond discharge can be high due to constrain on high voltage switch [6]. The possibility to use low cost components and simple architecture generator is studied in this paper. High voltage is produced using a Zero Voltage Switching (ZVS) flyback converter to drive a high voltage transformer. The cost of this system is limited thanks to not use a commercial high voltage power supply. Some components can be issued from recycled parts. The performances in terms of output signal, discharge energy, and synchronization are discussed. The utilization of the pulser in nanoparticles synthesis is considered from electrode erosion rate, and pressure estimation in the cavitation bubble generated by the spark is made.

II. Experimental setup

A. Power Supply

High voltage pulses are obtained using a high voltage transformer which primary coil is driven by an oscillating circuit, powered with DC voltage (Figure 1). The high voltage transformer T1 is a recycled part from a cathode ray tube power board (the cost of a new part, such as the model fbt40734 manufactured by Thomson, is about 40 $). The primary winding is remade with insulated cable with two 6 turn coils connected with a central point. Both parts of the winding are made in opposite orientation so the magnetic field have the same direction.

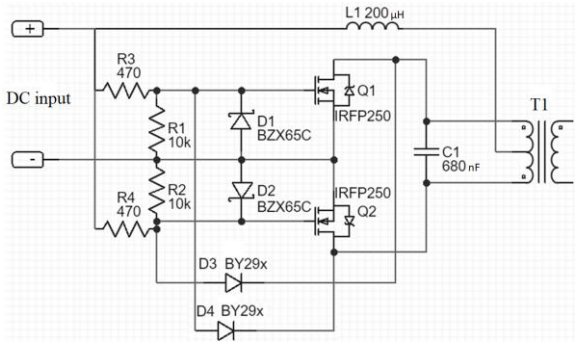

Fig. 1. Shematic representation of Zero Voltage Switch (ZVS) including oscillating circuit (at the left) and high voltage transmformer T1 (at the right)

The working frequency of the oscillator has to match that of the high voltage transformer. In order to tune easily this frequency, a ZVS flyback driver is used. Initially developed by Vladimiro Mazzilli [7], it is based on two MOSFETs (IRFP 250) and a LC oscillating circuit. The choice of the inductance

Submitted on April 2nd, 2020

T. Merciris is with the Groupe de physique des plasmas, Département de Physique, Université de Montréal, C.P. 6128, Succ. Centre-ville, Montréal, Québec H3C 3J7, Canada (e-mail: thomas.merciris@umontreal.ca).

A. Hamdan is with the Groupe de physique des plasmas, Département de Physique, Université de Montréal, C.P. 6128, Succ. Centre-ville, Montréal, Québec H3C 3J7, Canada (e-mail: ahmad.hamdan@umontreal.ca).

A Dorval is with the Université de Toulouse, LAPLACE (Laboratoire Plasma et Conversion d'Energie) 118 route de Narbonne F-31062 Toulouse Cedex 9, France

F Valensi is with the Université de Toulouse, LAPLACE (Laboratoire Plasma et Conversion d'Energie) 118 route de Narbonne F-31062 Toulouse Cedex 9, France (e-mail: valensi@laplace.univ-tlse.fr).

L_1 and the capacity C_1, setting the oscillation frequency, is set to $L_1 = 200$ µH and $C_1 = 680$ nF. This circuit, thanks to MOSFET switching at 0 V, does not have significant Joule loss. The cost of electronic components is about 10 $

For this study, a tunable DC power supply from AIM & Thurlby Thandar Instruments (model QPX600DP) is used to power the oscillating circuit. DC input voltage U_{DC} is adjustable between 15 and 50 V. Since the first oscillations after powering up the oscillator produce more energetic discharges, the power is repetitively commutated by a switch, with adjustable frequency.

B. Setup

The global setup is presented in Figure 2. The formation of the cavitation bubble by the discharge (as reported in [8]) is observed by shadowgraph method with a high speed camera Photron AX100 (up to 500 000 frames/s). Current and voltage are measured at the input of the ZVS using a LF 205-S current probe manufactured by Lem and a 10073C voltage probe manufactured by Agilent, respectively. For the high voltage output a TT HVP 2739 voltage probe from Testec and a 4100 Pearson current probe are used. Data are recorded using a 250 MHz oscilloscope (DSO6054A) with the software Keysight BenchVue 3.7; the oscilloscope is also used to trigger the high-speed camera.

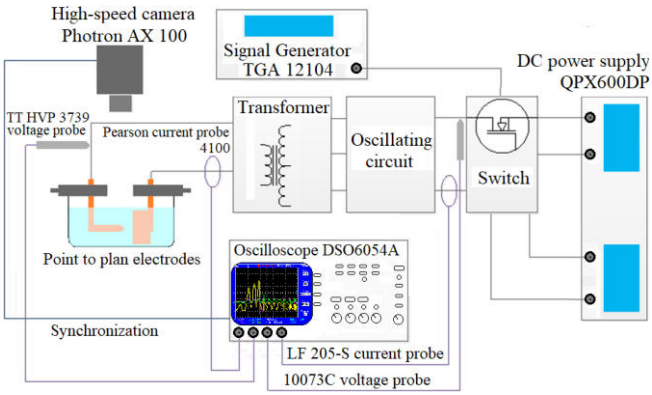

Fig. 2. The schematic diagram of the global setup

A pin to plane configuration is used. Both electrodes are made of copper. The ground plane electrode, which is the cathode, consists in a cylinder with radius of 1.75 cm, polished using abrasive paper (up to P2400). Electrode surface erosion is observed using a Keyence VHX 1000E microscope. The anode is also cylindrical with a diameter of 6 mm (length of 4 cm) but has a conical end, as shown on the left part of Figure 3. The electrode gap e_g can be adjusted using micrometric displacement tables. Discharges are realised in deionized water.

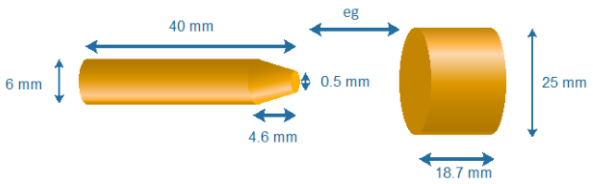

Fig. 3. The schematic diagram of electrode system

C. Data processing

The data from the oscilloscope are processed with numerical filters to remove all electromagnetic high frequency noise. The bandwidth is chosen to correspond to that of the probes.

For each experimental condition, ten acquisitions are made due to the low repeatability of measurement. An average of these measurements is done, the obtained variance is used to determine our uncertainties. They are mainly associated to the stochastic variation of breakdown voltage (and thus breakdown delay), but includes also measurement uncertainties.

III. Results

A. Breakdown process

When electrodes are separated by an insulating material (such as air), voltage increases gradually after each pulse of the circuit, until breakdown voltage is reached. But for electrodes in water some charges can leak between them and the voltage decreases notably on the fall edge. Even if this charge leak can reduce the voltage breakdown of water (that is higher than that of air) the voltage drop is so strong that the result is a detrimental effect. In addition, conductivity measurements after 10 tests show no clear modification. Since the voltage remains higher than at the beginning of the pulse, when the next pulse delivered by the generator occurs, the maximal voltage is higher. The result is an oscillating voltage (with frequency corresponding to the oscillating circuit frequency), the maximal value increasing gradually from one pulse to another. Breakdown occurs when voltage becomes sufficient, but unlike in air the value is not constant for a given configuration. An example is shown in Figure 4 for five tests (Test 0 to Test 4) executed in the same experimental conditions.

For a given pulse the high voltage is sustained only during a short period (a few µs). It is even possible that no breakdown occurs although the voltage is relatively high; this is due to the random presence of seed electrons to initiate the discharge [8]. They are produced by cosmic radiation, natural radioactivity (that cannot be predicted for the experiment duration), and can also come from the random presence of low-density regions or ions (from impurities) close to the pin electrode.This explains why variable number of pulses (from 2 to 6 in fig 4) is needed to have breakdown. Such a stochastic process results in variable breakdown voltage (from 4.2 to 5.6 kV). In order to quantify this variable duration, the time between the first voltage rise (first oscillation) and the breakdown is calculated for each test. This parameter is later called “breakdown delay”.

After the first discharge (at t = 0), the conditions change strongly since a cavitation bubble (see part G) is formed and discharge can take place in a gaseous environment. Excited species are present and no high voltage (below 1 kV) is needed for breakdown. As a result, successive voltage rises and drops can be visualized, corresponding to low voltage discharges. The frequency of these secondary discharges (> 1 Mhz) is not constant, it corresponds to oscillation of a circuit including the strongly variable impedance of the gas/liquid medium. Indeed, the discharges lead to increase of the conductivity of the medium and current flow is possible. This low current leak (below 0.1 A) leads to low erosion rate: when no discharge

occur, the only ablation process is electrochemical reactions (metal atoms turn into ions and leave the electrodes) that cause negligible effect for the considered duration. In addition, joule heating from the resulting ionic current in water is too low to cause metal melting or vaporization. This erosion mode is not the goal of the developed setup is type of process. On the other hand, the secondary discharges can cause erosion through plasma etching, but their contribution will be far much smaller than that of the first discharge.

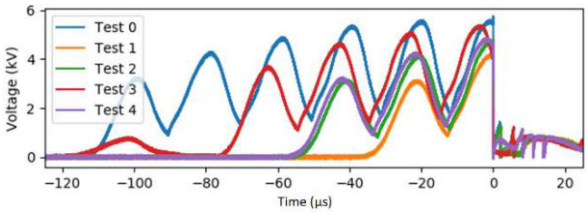

Fig. 4. Evolution of the high voltage output before and after the discharge.

Once breakdown occurs, current oscillation in a pseudo periodic damped mode occurs, with a frequency of 24 MHZ corresponding to the RLC discharge circuit including the plasma impedance. The corresponding discharge then occurs with oscillating current. With comparable circuit impedance, one can observe that the higher the breakdown voltage, the higher the resulting current. Current maximal values varies from 2.4 to 3.7 A, as seen in Figure 5. As a result, some variations in discharge energy can be observed. Discharge maximal power can be estimated to 200 W but the uncertainty is high, due to the low precision of the voltage probe at low voltage (below 100 V).

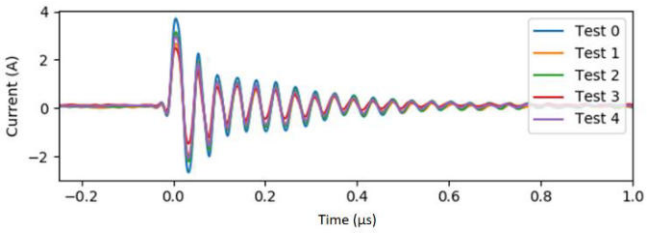

Fig. 5. Measured current for underwater discharges (U_{DC} = 50V / e_g = 0.2mm) before and after breakdown (at t = 0).

One can observe that the discharge will be sustained during ≈ 500ns, however the plasma changes a lot due to the large variation of current (and pressure). The plasma density, electronics density and temperature are not constants. [5][13]

B. Characterization of the discharge circuit

In order to study the pulser characteristics, the high voltage part has been modelled, as seen in Figure 6.

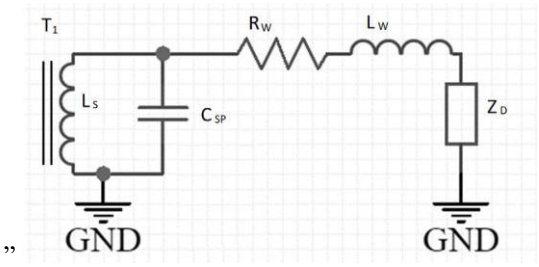

Fig. 6. Discharge equivalent circuit

The discharge equivalent circuit includes the secondary coil of the high voltage transformer T_1, the wires connecting the transformer to the electrodes, and the electric discharge itself. The transformation ratio of T_1 is 122. The resistance R_W and the inductance L_W correspond to the connecting wires. Since the inductance of the discharge (a few nH) is negligible when compared to that of the cables (a few µH), only a resistive component Z_D is considered for the discharge. The transformer secondary coil can be modelled by only a parasite capacity C_{SP}, the inductance being neglected due to its high impedance. It corresponds not only to the capacitance between each spire of the secondary coil of the transformer, but also to the capacitance of the high voltage probe (≈ 4pF), and the capacitance between the aluminum support and the high voltage electrode. C_{SP} should be in theory a fixed value for a given transformer and setup. It is not directly measured but is calculated from measured deposited energy.

According to previous works [9], the deposited charge on the electrode is the most relevant factor for nanoparticle synthesis efficiency. It can be calculated from integration of instantaneous current i(t) over discharge time. On the other hand, it can be related to the energy E stored in the capacitance (C_{SP}) according to the relation $E = ½ C_{SP} * V_B^2$, with V_B is the breakdown voltage. In order to check if C_{SP} was dependent of experimental parameters, it has been calculated for different experimental conditions (air and deionized water, various electrode gap e_g and DC input voltage U_{DC}), using values for deposited energy averaged over 10 measurements in each case. It appears that for all conditions, the value does not significantly change: 12 ± 3 pF, as shown in Figure 7. Some variation is always present due to moment when the breakdown appends (when the transformer primary supplies current). Also, one can note that the uncertainties in water are larger than those reported in air. However, those calculations show that the pulses are relatively stable in time after successive discharges for all cases.

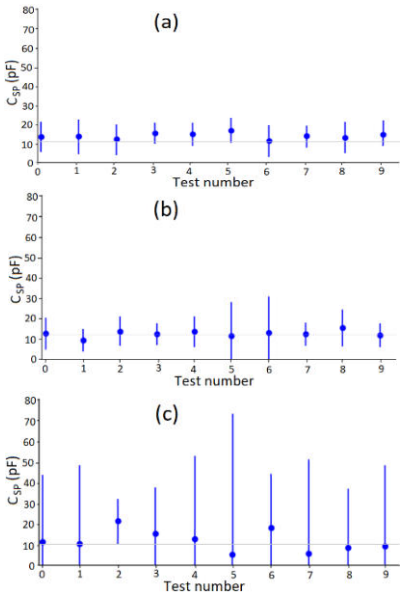

Fig. 7. Evolution of the calculated capacitance over successive disharges: (a) air, e_g = 0.5mm, U_{DC} = 20 V; (b) air, e_g = 1.0 mm, U_{DC} = 20 V; (c) water, e_g = 0.2mm, U_{DC} = 50 V

From these results, one concludes that the capacitance C_{SP} depends mainly on the transformer characteristics, while it has low influence on the deposited charge. The considered capacitance corresponds in each case to the average value (indicated by the grey line in Figure 7).

On the other hand, by a least-square method (Figure 8), it is possible to estimate the inductance needed to obtain a similar discharge current with the theoretical response of an RLC circuit from a step input:

$$\frac{d^2i(t)}{dt^2} + \frac{R}{L}\frac{di(t)}{dt} + \frac{i(t)}{LC} = 0$$

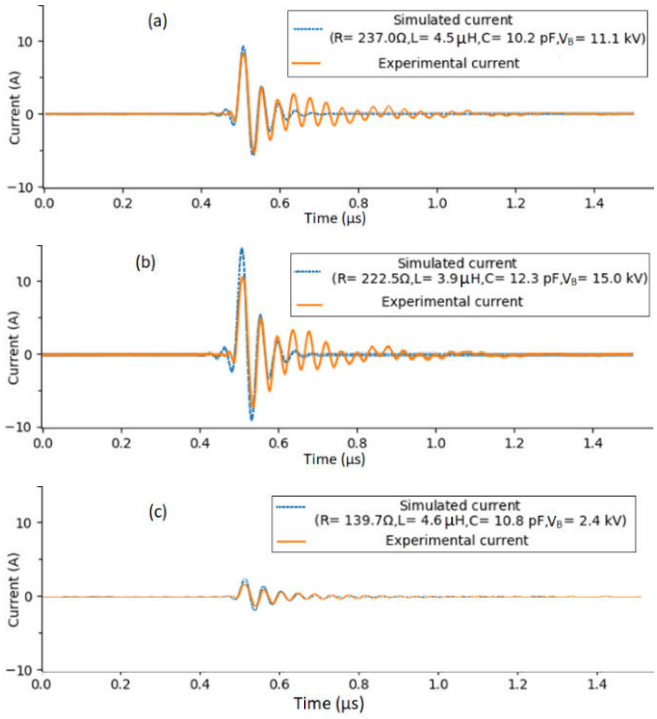

Fig. 8 Least-square method to determined RLC parameter on current discharge : (a) air, e_g = 0.5mm, U_{DC} = 20 V; (b) air, e_g = 1.0 mm, U_{DC} = 20 V; (c) water, e_g = 0.2mm, U_{DC} = 50 V

A value of ≈ 4 µH is deducted for the inductance cable. The capacitance deduced from the least-square method (10 to 12 pF) is in good agreement with the results calculated from deposited energy (see Fig. 7), which confirms the validity of the calculation. However, the breakdown voltage seems to be less than expected (15 kV vs. 17 kV, measured for air discharge with e_g = 1mm) and may be justified by an attenuation from the current probe used.

Moreover, in air discharge, the high voltage part of the pulser cannot be approached by the same value of RLC due to a large variation of resistance during discharge extinction causing a loss in the plasma channel temperature [10].

The determination of the RLC parameters is then not perfect since it is not possible to get simulated current that match exactly experimental data. This is mainly due to the non-stationary behaviour of the plasma, with variable RLC values. While simulated maximal current exceeds measured current, the three first simulated oscillations fit reasonably real current shape. In the case of discharge in water strong discrepancy only occur after the fifth half pseudo period.

C. *Influence of input voltage U_{DC}.*

The influence of input voltage U_{DC} on deposited charge, deposited energy, breakdown voltage, and breakdown delay is presented in Figure 9.

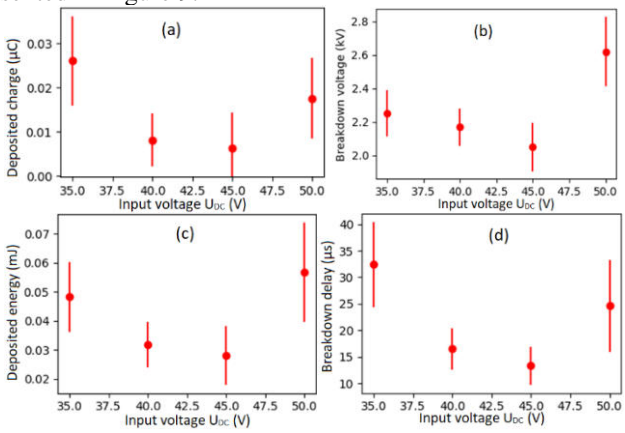

Fig. 9 Influence of circuit input voltage U_{DC} on discharge electric parameter: a) deposited charge; b) breakdown voltage; c) deposited energy; d) breakdown delay with a 0.2mm gap

The deposited energy is calculated using the following formula:

$$E = \int u(t)i(t)dt$$

Error bars correspond to uncertainties due to the probabilistic aspect of the breakdown that occurs differently for the same experimental conditions. In spite of these high uncertainties a pattern seems to appear. All parameters decrease as input voltage increases from 35 to 45 V, but they increase again for the voltage of 50 V. This could be interpreted as follows. For an input voltage around 35 V, there is not enough energy to reach the breakdown voltage after the first oscillation of the ZVS driver. The delay is then always superior to 25 µs (corresponding the first pulse duration). Then voltage increases slowly, cycle after cycle until the discharge can occur. Voltage at breakdown can be then high. For higher input voltage the probability of breakdown at first cycle increases.

For U_{DC} = 45 V, average breakdown delay is minimal (a duration of 10 to 15 µs corresponds to the half of one pulse, thus maximal voltage and optimal initiation). Since the discharge initiates at the first cycle, breakdown voltage remains low. When the input voltage further increases (U_{DC} = 50 V), the probability of breakdown failure at first cycle can be high again. This could be due to a sharper voltage rise (higher maximal value for similar pulse duration), hence a shorter time when the voltage is maximal. The first oscillation can then fail to lead to breakdown, requesting a second pulse to get it. As a result, delay can again be high, and since higher voltage is obtained for each single pulse, breakdown voltage can reach much higher value.

In terms of synchronization and operation duration, the value of U_{DC} = 45 V could be preferable, since only one pulse is needed to reach breakdown. But if one wants to maximize the deposited charge, which is an essential factor for nanoparticle synthesis,

the value of 35 V is preferable, since higher charge (and energy, see figures 9b and c) can be reach while the input energy is minimal (42 mJ in a period of 350µs). At higher voltage (U_{DC} = 50 V) deposited charge is also high, but the input energy is higher (83 mJ in a period of 350µs) thus a smaller efficiency than with U_{DC}=35V. The voltage range [35-45 V] is considered more interesting for nanoparticles synthesis.

D. *Influence of electrode gap e_g*

The increase of e_g induces an increase of the liquid total resistance between the two electrodes and thus higher voltage is needed to reach breakdown. To study this effect, two gap values (0.2 mm and 0.3 mm) are studied. The influence on deposited charge, deposited energy, breakdown voltage, and breakdown delay is presented in Figure 10.

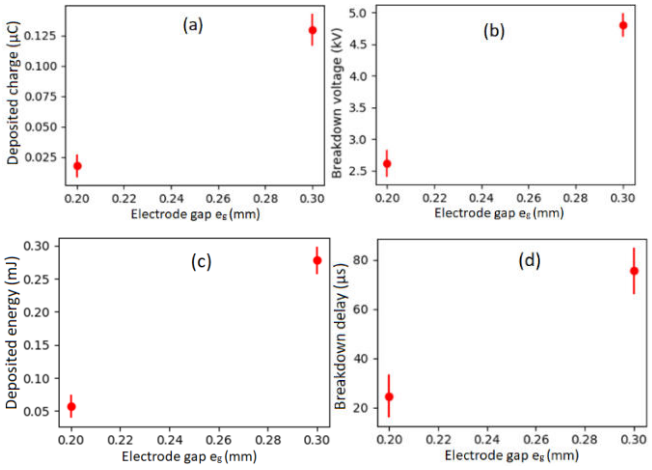

Fig. 10 Influence of circuit electrodes gap e_g on discharge electric parameter: a) deposited charge; b) breakdown voltage; c) deposited energy; d) breakdown delay for U_{DC} = 50 V.

It appears that for the studied range, the higher the electrode gap, the higher the efficiency and the deposited charge. When the gap is increased by 50%, the deposited charge (and thus, the deposited energy), the breakdown voltage, the breakdown delay and the efficiency are respectively increased by 500%, 100%, 300%, and 30%.

At longer e_g, the breakdown delay is relatively long since more alimentation cycles on the primary side of the transformer are needed to obtain sufficient voltage on the secondary side to allow the discharge to happen. A longer delay implies a greater accumulation of energy and charges before the breakdown.

E. *Voltage control using a spark gap*

In order to limit the power loss in the medium separating the electrodes, the influence of a spark gap (in air) has been studied. It is constituted of two metallic screws in an insulating holder placed in air, connected in serial with the high voltage pulser. The position of the screws can be changed to set the gap g_s. Breakdown must occur first in air before the circuit is closed and current can flow in the liquid between the electrodes. By adjusting the gap g_s it is possible to set variable threshold values for this to happen. The noticeable effect observed was the augmentation of the deposited charge for an augmentation of the spark gap length. The deposited charge increases proportionally with the gap, from 0.1 to 0.4 µC when gap increases from 4 to 15 mm. For larger gap however saturation occurs, with no more charge increase. This can be due to the limitation of the high voltage supply that can deliver up to 20 kV with the chosen parameters. These results show that the use of a spark gap is an easy way to increase breakdown voltage and thus deposited charge, which is favorable to high nanoparticles generation yield.

F. *Ablated mass*

The utilization of the pulser in nanoparticles synthesis is studied through the measurement of electrodes erosion rate. Since the ablated mass was not large enough to be measured directly with a precision balance, a volume estimation is made from geometric characteristics of impact craters on the cathode surface. Mass is calculated considering density of copper. Since such measurement is not possible on the anode (it is not possible to get well enough polished surface on a conical tip) the total ablated mass is estimated considering that the erosion at the anode corresponds to 70% of the ablated mass on the cathode [11]. This difference is due to the fact that positive ions impacting the cathode has stronger etching effect than elections impacting the anode. The cathode ablated volume is calculated considering that impacts correspond to spherical cups. The depth is set at 0.5 µm for all impacts: this average value is consistent with observed structures and the depth reported previously for comparable discharge energy [8]. The repartition of impact diameters for 26 discharges is presented in Figure 11.

An average mass of 0.30 ng is ablated on the copper cathode, leading to total ablation of 0.51 ng considering both electrodes. According to thermodynamic calculation, the energy needed to cause total fusion of this mass corresponds to 0.5% of the available electrical energy (0.06 mJ for the considered experimental conditions). This includes energy for heating up to melting temperature, and fusion energy per mass unit. And if one consider total vaporization (adding energy for heating to boiling temperature and vaporization energy) the ratio rises up to 5.1%.

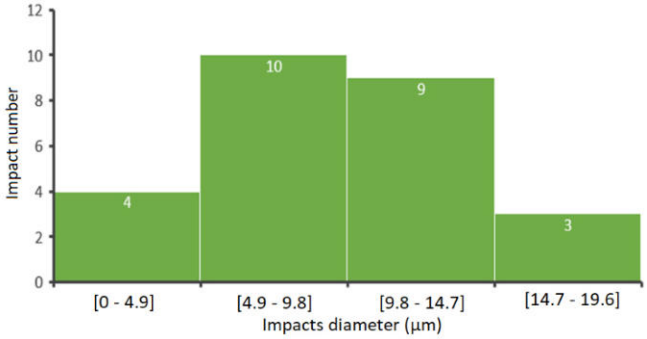

Fig. 11 Distribution of impacts diameters (U_{DC} = 50V – e_g =0.2mm)

Current results do not allow determination of the part of vaporized part out of melted part. However, results from literature indicate values of a few percent [12]. If one assumes that all ablated mass is melted and 10% of it is vaporized, one can estimate that 4% of electric energy is dissipated through material erosion. The other 96% of electric energy are dissipated through material heating and radiation losses. In term of nanomaterial production, this can be considered as the efficiency of the system. In order to get more information about

this, future work will focus on nanoparticle size and shape distribution study.

G. Determination of the discharge pressure

The formation of a cavitation bubble by the spark provides a way to estimate its pressure, which is an important parameter to characterize the process. The size of the bubble (growth and collapse, with successive oscillations) can be measured as a function of time through high speed imaging. An extract of an obtained sequence of images is showed in Figure 12.

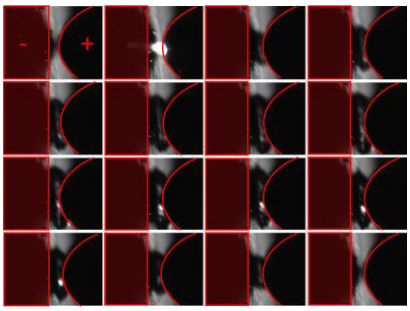

Fig. 12 Bubble shadowgraphy: Δt = 10 µs, image size: 3 by 2 mm (e_g = 0.2 mm, U_{DC} = 50 V). Discharge is visible second picture.

The shape of the bubble is not spheroidal due to the proximity of the electrodes. However to facilitate the study the volume is determined considering a sphere of an equivalent volume, yielding the corresponding radius. The Rayleigh-Plesset equation is then used to determine the initial pressure of the bubble [5]:

$$\ddot{R}R + \frac{3}{2}\dot{R}^2 = \frac{1}{\rho}\left(P_0\left(\frac{R_0}{R}\right)^{3\gamma} + P_v - \frac{2\sigma}{R} - 4\mu\frac{\dot{R}}{R} - P(t)\right) \quad (1)$$

$R, \dot{R}, \ddot{R}$ are respectively the radius of the bubble, the first, and second derivative over time of the radius. ρ is the mass density of the liquid. σ is the surface tension and μ is the viscosity. P_0, P_v, and $P(t)$ are the pressure at a long distance from the bubble, the saturated vapor pressure and the pressure of the liquid on the bubble over time. Here, the bubble is treated as an adiabatic system. The pressure inside the bubble can be therefor written as follows:

$$P_B(t) = P_0\left(\frac{V_0}{V(t)}\right)^{\gamma} \quad (2)$$

V_0 and $V(t)$ are respectively the volume of the bubble at equilibrium, and the volume of the bubble over time. γ is set equal to 1.4 to represent a diatomic gas. The assumption of an adiabatic system does not consider the energy losses with the environment, and the remanence of the spark discharge during the first tens of nanoseconds. To estimate the solution of the differential equation, a fourth- and fifth-order Runge-Kutta method is used with the following set of parameters: $\rho = 997\ kg.m^{-3}$, $\sigma = 0.8\ N.m^{-1}$, $P_v = 2300\ Pa$, $P_0 = P(t) = 10^5 Pa$, $\mu = 425\ mPa.s$, $R_0 = 255\ \mu m$, $R(t=0) = 78\ \mu m$, $\dot{R}(t=0) = 268\ m.s^{-1}$. The results of the calculation of radius, pressure, and experimental data are represented in Figure 13.

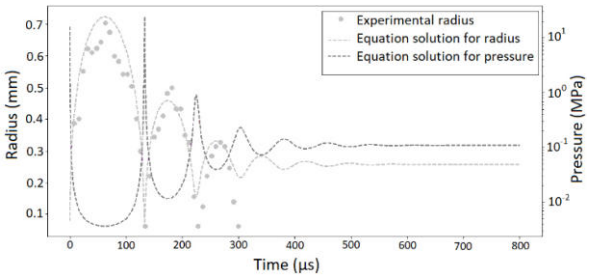

Fig. 13 Bubble radius (experimental and calculated) and calculated pressure (e_g = 0. 3mm, U_{DC} = 50 V)

The simulation is in a good agreement with the experiment. Some uncertainties are present due to the non-spherical shape of the bubble and the fact that the Rayleigh-Plesset model does not consider energy transfers. The initial pressure obtained is $15.9\ MPa$, which is in the same range of value reported in heptane (dynamics of bubbles created by plasma in heptane for micro gap conditions) [8].

This estimation of pressure shows that our design recreates condition of pressure compatible with the generation of nanoparticles.

Those particles are created inside this gas bubble, thus the pressure inside will have an influence on the distribution size of the particles [14, 16] or the crystal composition, for example anisotropic growth of particles [15]. The bubble size and behaviour are also related to discharge parameters, size is larger with higher DC input U_{DC} and electrode gap e_g. In general, the higher the deposited energy, the higher the bubble size.

IV. Conclusion

The utilization of a ZVS driver to power a high voltage transformer connected to immerged electrodes showed the possibility to get erosion pattern similar to what is observed in literature. This confirms the interest of this cheap and simple configuration for study of nanoparticles synthesis conditions. Further work will be needed to get a complete comparison with other setup (such commercially available spark pulser), in particular concerning the possibility to control the deposited energy and the performances optimization.

The study of the equivalent discharge circuit show that it can be simplified as a capacitive discharge, and the inductive aspect of the high voltage transformer is not dominant. Optimal working conditions are found for input voltage U_{DC} in the range 35-45 V. Estimation of ablated mass yields to an efficiency of 4% from total input energy.

As expected, the less efficient part is the high voltage transformer, which is not designed to work at this frequency and have a high iron losses (due to its ferrite core). Moreover, only one of the secondary windings is used: unused windings may lead to additional losses.

Further investigations will be needed to better characterize the erosion pattern and the obtained nanoparticles. The influence of other electrode materials (aluminum, molybdenum) and dielectric liquids will also be considered.

ACKNOWLEDGMENTS

The authors wish to thank Gilles Charles, from GREMI laboratory, for his help in developing the ZVS circuit ant the high voltage power supply.

REFERENCES

[1] P. Bruggeman and C. Leys, “Non-thermal plasmas in and in contact with liquids,” J. Phys. Appl. Phys., vol. 42, no 5, p. 053001, mar. 2009.

[2] E. Hontañón, J. M. Palomares, M. Stein, X. Guo, R. Engeln, H. Nirshl, and F. E. Kruis, “The transition from park to arc discharge and its implications with respect to nanoparticle production,” J. Nanopart Res 15 – p.1957, 2013.

[3] N. S. Tabrizi, M. Ullmann, V. A. Vons, U. Lafont, and A. Schmidt-Ott, “Generation of nanoparticles by spark discharge,” J. Nanopart. Res. 11 - p315-332, 2009.

[4] A. Hamdan, H. Kabbara, C. Noel, J. Ghanbaja, A. Redjaimia, and T. Belmonte, “Synthesis of two-dimensional lead sheets by spark discharge in liquid nitrogen,” Particuology 40 p.152-159, 2018.

[5] A. Hamdan, C. Noel, F. Kosior, G. Henrion, and T. Belmonte, “Dynamics of bubbles created by plasma in heptane for micro-gap conditions,” J. Acoust. Soc. Am., vol. 134, no 2, p. 991-1000, aug. 2013.

[6] T. Charinpanitkul, K. Kanjanaprapakul, N. Leelaviwat, N. Kurukitkoson, and K.-S. Kim, “Effect of arc current on characteristics of nanocarbons prepared by cryogenic arc discharge method,” J. Ind. Eng. Chem., vol. 16, no 6, p. 912-917, 2010.

[7] D. Ahmad Hapidin, I. Saleh, M. M. Munir, and K. Khairurrijal, “Design and Development of a Series-configuration Mazzilli Zero Voltage Switching Flyback Converter as a High-voltage Power Supply for Needleless Electrospinning,” Procedia Eng., vol. 170, p. 509-515, dec. 2017.

[8] A. L. Kupershtokh, E. I. Palchikov, D. I. Karpov, I. Vitellas, D. P. Agoris, and V. P. Charalambakos, “Stochastic model of breakdown initiation in dielectric liquids,” J. Phys. Appl. Phys., vol. 35, no 23, p. 3106-3121, dec. 2002.

[9] A. Hamdan, C. Noel, F. Kosior, G. Henrion, and T. Belmonte, “Impacts created on various materials by micro-discharges in heptane: Influence of the dissipated charge,” J. Appl. Phys., vol. 113, no 4, 2013.

[10] J. Andrea, P. Besdel, O. Zirn, and M. Bournat, “The electric arc as a circuit component », *IECON 2015 - 41st Annual Conference of the IEEE Industrial Electronics Society*, 2015, p. 003027-003034.B. O.

[11] B.O. Meuller et al., “Review of Spark Discharge Generators for Production of Nanoparticle Aerosols,” Aerosol Sci. Technol., vol. 46, no 11, p. 1256-1270, nov. 2012.

[12] F. Lago, J. J. Gonzalez, P. Freton, and A. Gleizes “A numerical modelling of an electric arc and its interaction with the anode: Part I. The two-dimensional model,” J. Phys. D: Appl. Phys. 37 p. 883–897, 2004.

[13] Y. Luo, A. M. Lietz, S. Yatom, M. J. Kushner, et P. J. Bruggeman, « Plasma kinetics in a nanosecond pulsed filamentary discharge sustained in Ar–H 2 O and H 2 O », Journal of Physics D: Applied Physics, vol. 52, no 4, p. 044003, janv. 2019, doi: 10.1088/1361-6463/aaeb14.

[14] J. Tomko et al., « Cavitation bubble dynamics and nanoparticle size distributions in laser ablation in liquids », Colloids and Surfaces A: Physicochemical and Engineering Aspects, vol. 522, p. 368 372, juin 2017, doi: 10.1016/j.colsurfa.2017.03.030.

[15] M. Trad et al., « Synthesis of Ag and Cd nanoparticles by nanosecond-pulsed discharge in liquid nitrogen », Frontiers of Chemical Science and Engineering, vol. 13, no 2, p. 360 368, juin 2019, doi: 10.1007/s11705-019-1802-7.

[16] L. Yu. Fedorov, I. V. Karpov, A. V. Ushakov, et A. A. Lepeshev, « Influence of pressure and hydrocarbons on carbide formation in the plasma synthesis of TiC nanoparticles », Inorganic Materials, vol. 51, no 1, p. 25 28, janv. 2015, doi: 10.1134/S0020168515010057.

3.Détermination d'un circuit équivalent pour les décharges dans l'eau : Évolution temporelle de la densité et température électronique

Dans le chapitre précédant, une simulation RLC permettait de réaliser une reproduction approximative du courant traversant le milieu plasma. À la suite du changement de système expérimental pour la suite de la collaboration entre l'UdeM et UT3 et afin d'améliorer le modèle du canal plasma pour comprendre les conditions de synthèses des nanoparticules, un nouveau circuit équivalent fût développé.

Dans ce chapitre, nous allons donc réaliser un circuit équivalent pour reproduire le courant de la décharge en utilisant un modèle de la conductivité de la colonne plasma et des mesures spectroscopiques afin d'obtenir une image de la température et de la densité électronique en fonction du temps. Les résultats seront présentés sous la forme d'une publication scientifique qui fait l'objet d'une soumission dans le journal IEEE Transaction on Plasma Science. (TPS13269)

À la différence du système toulousain, la haute tension va monter très rapidement (≈ 5 ns) ce qui ne va pas permettre la formation de microbulle dans l'eau déionisée. Cette différence va avoir une influence sur la dynamique du signal électrique mesuré (inductance plus grande). Le reste de décharge peut être très similaire avec des durées de décharges aux alentours de 500 ns et de 5 kV.

Dans cette publication, T. Merciris a réalisé la conception et la programmation du script Julia utilisé, la majorité de l'analyse ainsi que la rédaction initiale de l'article. Les co-auteurs ont participé à l'analyse des résultats et à la rédaction de l'article.

Determination of the electrical circuit equivalent to a pulsed discharge in water: assessment of the temporal evolution of electron density and temperature

Thomas Merciris, Flavien Valensi, Ahmad Hamdan

***Abstract*— Pulsed electrical discharges in dielectric liquids are intensively studied due to the wide range of applications in which they are implicated. Despite the simplicity of the experimental manipulation of these discharges, the underlying fundamental physics is relatively complex. In this study, we use the electrical characteristics, voltage and current, of pulsed discharges in water (various applied voltage and pulse width conditions) to determine the equivalent electrical circuit of the plasma. Based on a Mayr-type model, the plasma resistance is time dependent, but the inductance is not. Considering that plasma resistivity also depends on electron density and temperature (Spitzer formula), the temporal evolution of these two parameters were also determined.**

***Index Terms*— Electron density, electron temperature, equivalent electrical circuit, plasma inductance, plasma in-water, spark discharge.**

I. Introduction

OVER the past few decades, electrical discharges in dielectric liquids have been extensively studied [1–3] due to their effectiveness in several applications, including water treatment [4–6], electrical discharge machining (EDM) [7–9], nanomaterial synthesis [10–12], and high voltage breakers and transformers [13–15], among others. The fundamentals and mechanisms underlying dielectric breakdown have been investigated experimentally [16,17] and theoretically [18,19]. In general, two theories have been proposed to describe plasma ignition in dielectric liquids: the bubble theory and the direct ionization theory. The former is based on the assumption that the discharge is generated within gaseous bubbles formed in the vicinity of the electrode needle. These bubbles are produced due to the local evaporation of the liquid under the effect of Joule heating [20,21], or due to the electrostrictive forces in the inhomogeneous electric field [16,22]. The direct ionization theory, on the other hand, assumes that the ionization process in liquids is similar to that in dense gas-phase plasma [18]. Knowing that the physical phenomena implicated by the two theories are highly sensitive to the waveform of the applied voltage (mainly the rise time and the magnitude) and to the properties of liquid (mainly its polar or non-polar nature), some discharges conform to the bubble theory, while others are better described by the direct ionization theory.

The temporal and spatial dynamics of dielectric liquid breakdown are relatively rapid, resulting in initiation and propagation times of the plasma channel that are in the range of pico and nanoseconds, respectively [23–25]. Moreover, discharges in liquids are characterized by low reproducibility due to the modification of the electrode's characteristics (geometry and local chemical composition) as well as the solution properties (electrical conductivity and composition) [26,27]. This impedes the study of temporal plasma evolution, even using equipment with (sub-)nanosecond resolution. To overcome this limitation, the temporal evolution must be studied using various discharges at different delays. Despite its advantages, this method cannot be used to reliably assess the variations in plasma properties (dimension, electron temperature, density, etc.). Instead, it provides average values during a particular temporal period [23,24].

On the other hand, the evolution of the electrical characteristics of the plasma, such as current and voltage, may be precisely and easily resolved using one single discharge. As such, the electrical properties of discharges in dielectric liquids are often reported in literature [19,28,29]. In general, authors use these properties to estimate the energy, power, or charge of the discharge [26,32]. However, they usually do not comment on certain common features, such as the oscillation behaviors of current and voltage [23,30,31,33].

This study investigates the current and voltage characteristics of electrical discharges (spark mode) generated in water using high voltage pulses with varying amplitudes and widths. Using the acquired data, the equivalent electrical circuit of the plasma

This research was funded by the Natural Sciences and Engineering Research Council of Canada (NSERC) under award number RGPIN-2018-04869. The authors thank the Fonds de Recherche du Québec – Nature et Technologie (FRQ-NT) and the Canada Foundation for Innovation (CFI) for funding the research infrastructure.

T. M. is with the Groupe de physique des plasmas, Département de Physique, Université de Montréal, 1375 Avenue Thérèse-Lavoie-Roux, Montréal, H2V 0B3, Québec, Canada (e-mail: thomas.merciris@umontreal.ca).

F. V. is with Université de Toulouse, LAPLACE (Laboratoire Plasma et Conversion d'Energie), 118 route de Narbonne, F-31062 Toulouse Cedex 9, France (e-mail: valensi@laplace.univ-tlse.fr).

A.H. is with the Groupe de physique des plasmas, Département de Physique, Université de Montréal, 1375 Avenue Thérèse-Lavoie-Roux, Montréal, H2V 0B3, Québec, Canada (e-mail: ahmad.hamdan@umontreal.ca)

is determined, and the relation between plasma channel resistance and electron density or temperature is assessed. Finally, the temporal evolution of the plasma properties is provided.

II. Experimental Setup and Data Pre-Processing

A. *Experimental setup*

The experimental setup used herein (Figure 1) is composed of two copper electrodes (10 cm length, 2 mm diameter, and 99.99% purity; Goodfellow) vertically mounted on a micrometer positioning system (gap distance fixed at ~50 µm) and immersed in 10 mL deionized water (initial conductivity ~3 µS/cm) contained within a quartz cell (inner and outer diameters of 8 and 10 mm, respectively). The upper electrode is mechanically polished to a curvature radius of ~10 µm, and it is connected to a pulsed positive-polarity power source (NSP 120-20-P-500-TG-H, Eagle Harbor Technologies) that supplies voltage with adjustable magnitudes and pulse widths. In this study, the tested magnitude and pulse width were 5, 10, 15, and 20 kV and 100, 200, 300, 400, and 500 ns, respectively. The lower electrode is polished to a plane surface and connected to the ground. The voltage and current of the discharge generated between the two electrodes were measured using a high-voltage probe (P6015A, ×1000, 75 MHz; Tektronix) and a current monitor (6585, 0.5 V/A, 200 MHz; Pearson), respectively. Finally, the voltage and current waveforms were acquired using an oscilloscope (MSO54, 2 GHz, 6.25 GS/s; Tektronix).

We used a monochromator (Acton 2750) to acquire emission spectra, and the intensity of each optical transition was recorded by an ICCD camera (PI-MAX from Princeton Instruments). Light emission measurements were carried out using the 600 lines/mm grating blazed in the visible range. The synchronization between the ICCD camera and the voltage pulse is ensured using delay generator (Quantum Composers Plus 9518 Pulse Generator). The camera integration time was fixed to 20 ns and, to ensure high signal-to-noise ratio, each spectrum is an average of 250 events. Note that the emission is not spatially resolved but averaged over the gap.

B. *Data pre-processing*

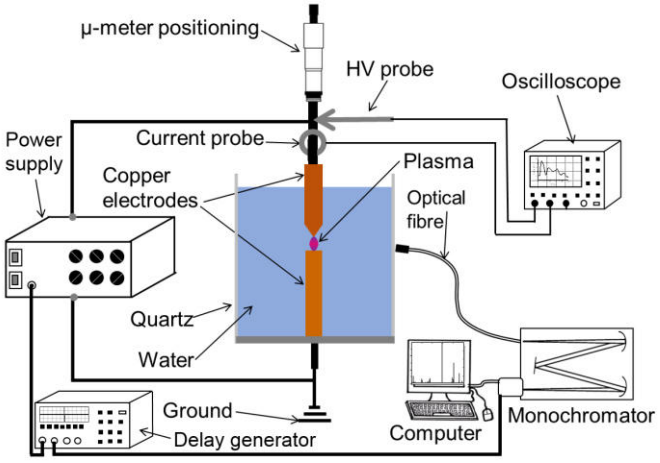

Fig. 1. Scheme of the experimental setup.

The use of pass-band probes to record electrical waveforms results in the generation of appreciable noise due to electromagnetic perturbations. Such noise implicates significant error in the numerical solutions of differential equations (see Section 3). To overcome this problem, the experimental raw data was filtered using a low-pass, third order, Butterworth filter with a cut-off frequency of 75 MHz. A typical example of filtered current and voltage waveforms is presented in Figure 2. Although the application of this filter slightly modifies the data, in particular during the abrupt change of current and voltage (i.e., breakdown), such modifications do not significantly influence the determined values of different parameters.

To correct for the temporal delay between current and voltage waveforms, the data corresponding to a misfired discharge (20% of all discharges in this study) were also acquired. The term misfired discharge describes the situation wherein a discharge does not occur between the electrodes even though the system is supplied with a high voltage pulse. This happens when free electrons, ions, and voids are lacking in the gap. Under such conditions, the inter-electrodes distance may be treated as capacitance, and the measured current is only capacitive, i.e., proportional to the time derivative of the voltage. In this case, the temporal delay between voltage and current waveforms aligns the current with the derivative of the voltage.

III. Determination of the Equivalent Electrical

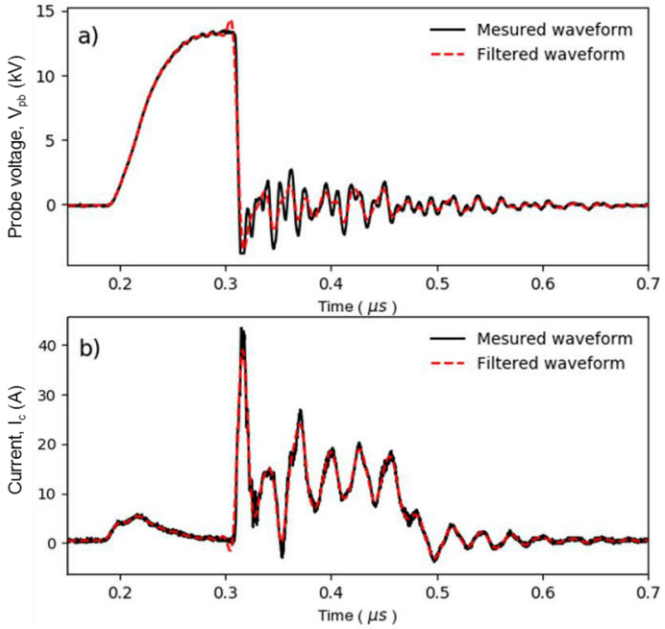

Fig. 2. Typical (a) voltage and (b) current waveforms with and without filtration (applied voltage = 15 kV and pulse width = 300 ns).

Circuit

A. *Equivalent circuits of various parts in the setup*

To determine the equivalent electrical circuit of a nanosecond discharge in water, it is important to consider all the components of the setup, including the pulser, the electrodes, and the probes. The circuit corresponding to the pulser is given by the manufacturer, and it is presented as C1 in

Fig. 3 (R_{sa} and C_a are the resistor and the capacitance of the pulser). The electrical cables connecting the power supply to the electrodes and the voltage probe connected to the pin electrode are referred to as C2 and C3, respectively. R_w and L_w in C2 are respectively the resistor and inductance of the cables, while R_{pb} and C_{pb} in C3 are respectively the resistor and the capacitance of the voltage probe. Meanwhile, the electrode and gap circuit are referred to as C4. The symbols L_e and R_e correspond to the electrode inductance and resistor, respectively, whereas C_g is the capacitance of the water-filled gap separating the two electrodes. C5 presents the plasma circuit that is composed of an inductance (L_p) and a resistor (R_p) connected in series. The resistor R_l represents liquid resistance, and it is connected in parallel to the plasma channel equivalent circuit.

B. *Mathematical description of the circuit using Kirchhoff's laws*

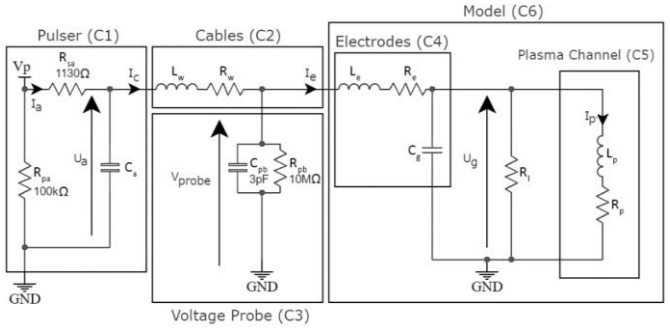

Fig. 3. Equivalent electrical circuit of the experimental setup.

To complete the mathematical description of our system, Kirchhoff's laws, mesh and nodal rules, were applied to the equivalent circuits C1-C6. Considering that our primary goal is to describe the plasma channel, the mesh rule was first applied to C5. The resulting relationship between *Rp*, *Lp*, *Ip*, and *Ug* is given in (1),

$$U_g(t) = R_p(t)I_p(t) + L_p d_t(I_p(t)) \quad (1)$$

where d_t is the time derivation operation, I_p is the plasma current, and U_g is the plasma voltage across the gap. The successive application of the nodal and mesh rules to other circuits in the system lead to various differential equations, as shown in Fig. 4.

The coupled differential equations presented in Fig. 4 comprise several unknown parameters, some of which can be determined indirectly. For instance, C_g is estimated based on the acquired current and voltage waveforms of a misfired discharge (15.6 pF). The same waveforms are also used to determine $V_p(t)$ according to (2),

$$V_p(t) = U_a(t) + R_{sa}\big(I_e(t) + C_a d_t(U_a(t))\big) \quad (2)$$

where $U_a(t)$ is given by:

$$U_a(t) = V_{probe}(t) + L_w d_t I_e(t) \quad (3)$$

R_{sa} and C_a are constants that depend on the pulser, whereas L_w is the inductance of the wire. These parameters, along with L_e, are needed to determine R_p and L_p; however, other parameters such as R_l (> 1 MΩ), R_e (< 10 mΩ), and R_w (< 10 mΩ) are assumed to be too high or too low, and thus, their influence on R_p and L_p is neglected.

To simplify the problem, we suppose that L_p and C_g do not change with time, and that only R_p is time dependent. This assumption is commonly applied in the development of a model that describes the plasma channel of an electrical arc [37–39]. Previously, several models [30,40] had been developed to describe the temporal dynamics of plasma resistance in nanosecond gas discharges, based on the Braginskii theory [41]. This theory suggests that the discharge creates a narrow channel heated by Joule effect. Under the effects of rapidly increasing temperature and pressure, this channel expands. Eventually, the temperature stabilizes due to hydrodynamic (associated with expansion) and radiative cooling, resulting in an approximately constant electrical conductivity of the conducting channel. Braginskii's theory applies well to the channel dynamics observed initially during discharge. However, it fails in predicting plasma behavior over long periods of time, particularly during the extinction phase. In this study, a Mayr-type [42] model was used to study R_p based on the temporal evolution of plasma conductance ($G_p(t)$) given in (4),

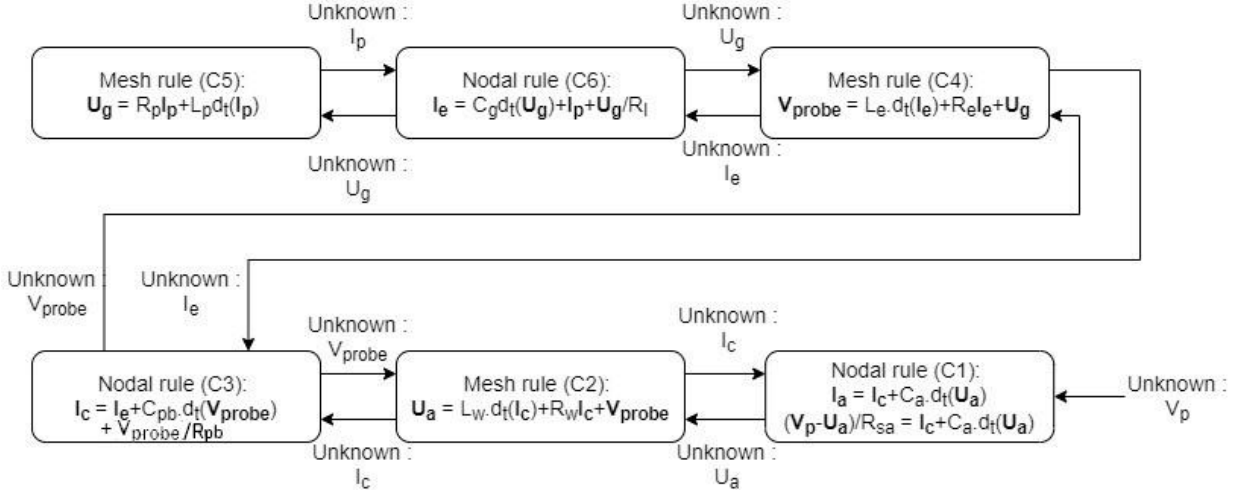

Fig. 4. Flowchart diagram of the differential equations determined for the equivalent circuits shown in Fig. 3.

$$d_t G_p(t) = \frac{G_p(t)}{\tau}\left(\frac{I_p(t)^2}{G_p(t)P} - 1\right) \quad (4)$$

where P and τ refer to the "cooling power" and "time constant", respectively.

C. *Description of the numerical method*

The numerical values of the model parameters were determined by solving the system of differential equations based on the DifferentialEquation.jl module of Julia 1.2 [43]. Considering that the problem is "stiff", it is not recommended to use the computationally expensive explicit methods. The Rosenbrock23 solver [44] was used to calculate the parameters under the condition that the callback on G_p cannot be negative.

The recorded current waveform of the plasma discharge was used to validate the values of the calculated parameters. By minimizing the difference between the simulated and measured currents, the model parameters, particularly L_p and $G_p(t)$, were optimized. Considering the non-smooth aspect of the minimization function (oscillating pattern) and to ensure that a global minimum is reached, the "Particles Swarm" minimization method was used instead of the traditional least square gradient-based method. Figure 5 presents a descriptive flowchart of the program and resolution pathways applied herein.

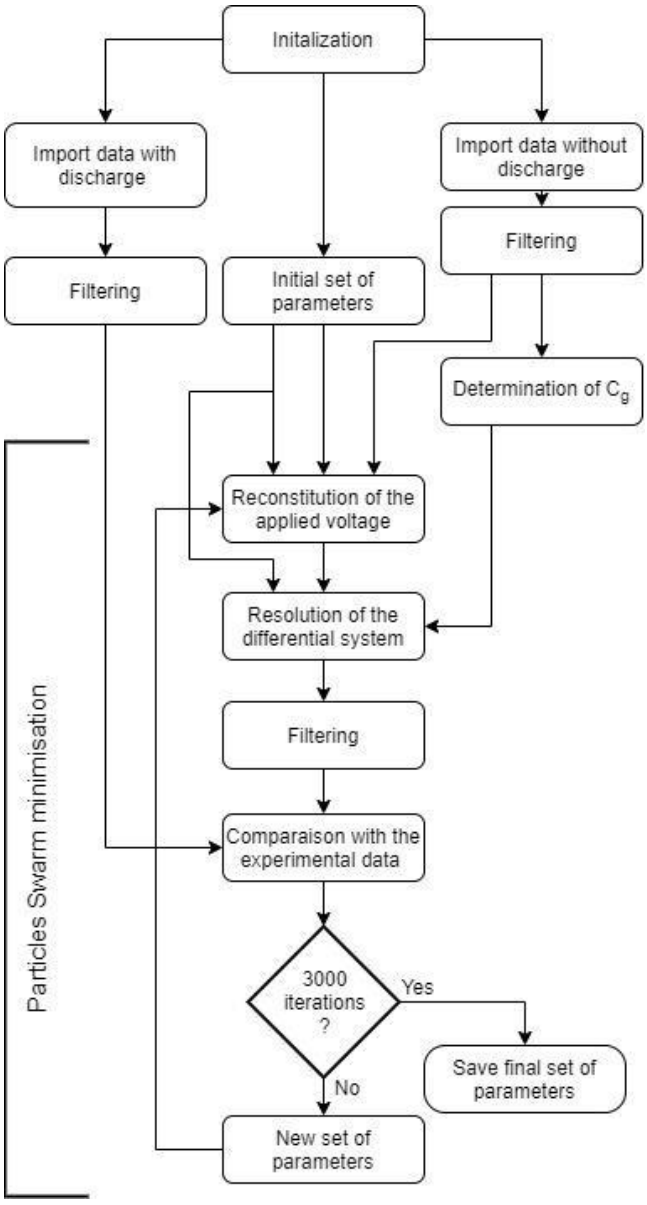

Fig. 5. Flowchart of the program and resolution pathways.

IV. Results

A. *Determination of the equivalent circuit parameters*

The electrical characteristics of discharges generated at various voltage and pulse width conditions were analyzed. The electrical connections, electrode geometry, and gap distance were kept relatively constant during each experiment, with minor variations in the latter two parameters due to electrode erosion. These variations do not affect the electrical waveforms, and thus, they can be neglected. L_w and L_e were estimated theoretically and calculated using our model. The optimal calculated values (L_w = 3.73 µH and L_e = 0.28 µH) were found to be similar to the theoretically ones (L_w = 3.01 µH and L_e = 0.21 µH), which confirms the accuracy of our model. As for C_g, its optimal value was found to be 15.6 pF, irrespective the investigated discharge conditions. The R_{sa} value determined herein (0.94 kΩ) is slightly lower than that available in the pulser datasheet (1.1 kΩ).

Compared to the measured current waveforms, the waveforms simulated at an applied voltage of 15 kV and at pulse widths of 200 and 400 ns are similar, with analogous capacitive currents between 0.2 and 0.3 µs (Fig. 6). Globally, the model yields good prediction of the discharge current. The first discharge peak is slightly underestimated, but the oscillating patterns are correctly predicted, especially for longer

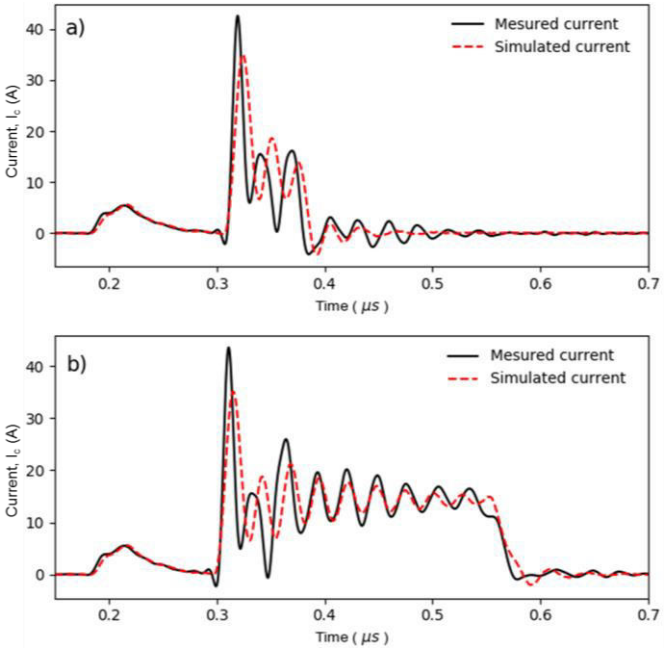

Fig. 6. Simulated and measured current waveforms: a) applied voltage = 15 kV, pulse width = 200 ns and b) applied voltage = 15 kV, pulse width = 400 ns.

pulse widths.

The model developed herein was also used to predict discharge voltage. Figure 7b compares the measured and simulated voltage waveforms determined using the current parameters optimized at 15 kV applied voltage and 300 ns pulse width (Fig. 7a). In general, the predicted voltage profile agrees well with the experimental counterpart. It is worth noting that the voltage waveform can also be used as model input. When tested under several conditions, the voltage values predicted using this waveform were improved; however, the current predictions were of inferior quality. Considering that the plasma-related values R_p and L_p are not significantly affected by voltage, only the current waveforms were used as an input parameter in the model, which renders the simulation more cost effective.

The plasma inductance values determined using simulated data collected under varying discharge conditions are presented in Table I. Note that only the applied voltage was varied, since

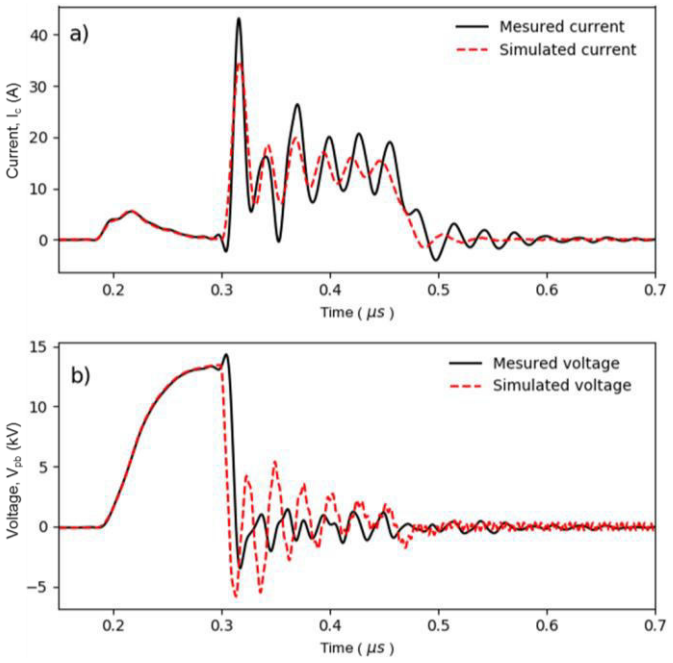

Fig. 7. a) Simulated and measured current waveforms at an applied voltage of 15 kV and pulse width of 300 ns. b) Comparison between the measured voltages and those predicted using the model parameters optimized in a).

plasma inductance is independent of discharge pulse width. The obtained results demonstrate that inductance decreases with increasing voltage up to 15 kV. Beyond this value, the inductance of the plasma remains constant at 1.27 µH. The highest inductance of 1.66 µH is recorded at 5 kV. Compared to previously reported values of plasma inductance for discharge in air (order of nH) [34,45], the inductance values determined herein are relatively high (order of µH). The discrepancy may be related to variations in the plasma properties of gas and liquid discharges. Indeed, discharges in liquid are characterized by high pressures (tens of bars) and electron densities (10^{17}-10^{19} cm^{-3}), compared to atmospheric pressure discharges (electron density < 10^{17} cm^{-3}). Since L_p is assumed to be time-independent, the calculated values are taken to be the temporal averages. In addition to applied voltage, plasma inductance also depends on the geometric dimensions of the plasma channel, especially its diameter [45].

Figure 8 presents the temporal evolution of plasma conductance under varying conditions of applied voltage and shows that it exhibits an oscillating pattern similar to that of the

TABLE I
PLASMA INDUCTANCE PREDICTED BY THE MODEL AT VARYING CONDITIONS OF APPLIED VOLTAGE.

Applied voltage (kV)	5	10	15	20
Plasma inductance (µH)	1.66	1.36	1.27	1.27

current waveform. Initially, conductance rapidly increases to 0.1 S, then it oscillates with an overall slight decrease, until it reaches ~0.01 S. Upon discharge extinction, plasma conductance falls exponentially to zero. The oscillating behavior of plasma conductance may be attributed to temporal variations in plasma properties (plasma diameter, electron temperature, or electron density). This aspect is further discussed in a subsequent section of the study. As in the case of inductance, the conductance of the plasma is independent of discharge pulse width.

Plasma conductance is also dependent on two unknown parameters τ and P. The calculated values of these parameters are summarized in Table II. P and τ increase significantly from

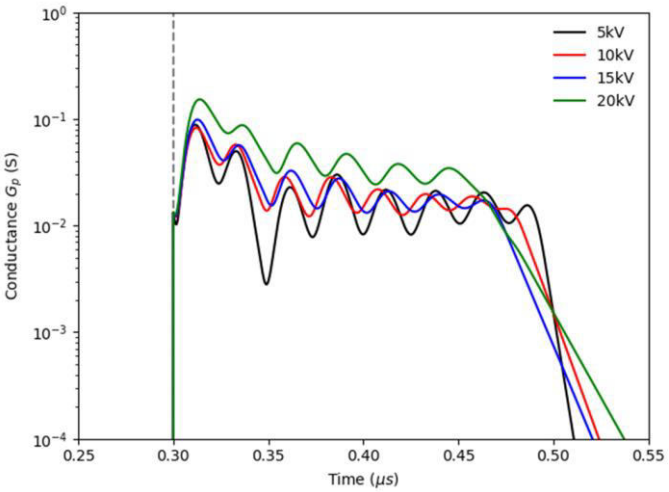

Fig. 8. Temporal evolution of plasma conductance under varying conditions of applied voltage (pulse width = 500 ns). The dashed line indicates the breakdown.

~1 to ~20 kW and from 3.9 to 13.6 ns, respectively, with increasing applied voltage between 5 to 20 kV. Parameter P represents the average power of the plasma during the discharge period, and thus, it is expected to increase under higher applied voltage conditions. As for τ, it corresponds to the time required for the plasma to reach equilibrium, and so, it is also expected to increase with increasing discharge voltage, due to higher current peaks. The τ values determined at 5 and 20 kV are ~10 ns different, which is indicative of fast plasma dynamics and high sensitivity to the applied voltage.

TABLE II
VARIATION OF P AND T, PARAMETERS USED IN THE PLASMA CONDUCTANCE MODEL, AS A FUNCTION OF APPLIED VOLTAGE.

Applied voltage (kV)	5	10	15	20
P (W)	1003	4589	11852	19943
τ (ns)	3.9	8.8	10.2	13.6

B. *Plasma properties derived from the model*

The plasma conductance (or resistance) predicted by the model was used to estimate certain properties that could not be determined experimentally, such as the temporal evolution of electron temperature. Assuming that the plasma is a homogeneous cylinder, G_p is related to plasma resistivity (ρ_p) via (5) [48],

$$\rho_p = \frac{\pi r_p^2}{G_p h} \tag{5}$$

where r_p and h are the radius (m) and length (m) of the plasma, respectively. The resistivity is also related to electron temperature (T_e) and density (n_e), and assuming a Maxwellian distribution, this relation can be expressed using the Spitzer formula given in (6) [49],

$$\rho_p = \frac{\sqrt{2m_e}e^2 * Z_{eff}}{12\pi^{3/2}\varepsilon_0^2 T_e^{3/2}} \ln\left(\frac{{T_e}^{3/2}}{\sqrt{\pi}e^3 n_e^{1/2}}\right) * F(Z_{eff}) \tag{6}$$

where m_e is the electron mass (kg), e is the electron charge (C), Z_{eff} is the effective ionic charge ($Z_{eff} = 1$), and $F(Z_{eff})$ is given by:

$$F(Z_{eff}) = \frac{1+1.198*Z_{eff}+0.222*{Z_{eff}}^2}{1+2.966*Z_{eff}+0.753*{Z_{eff}}^2} \tag{7}$$

It is worth noting that Spitzer formula implies Coulomb collisions, and therefore electron-neutral collisions are neglected. This assumption could be valid once the breakdown is reached, but not in the ignition phase. where the electron neutral collisions are of importance.

So far, it is not clear whether the r_p parameter in (5) corresponds to the impact radius (evidence of plasma surface interaction) or to the plasma emission radius. In general, the impact radius depends on discharge parameters [46, 47], and under conditions similar to those investigated herein, this radius is typically 10 µm [26]. The plasma emission radius, on the other hand, is estimated at 100 µm, based on time resolved imaging [23]. In this study, the calculations were performed using both radii, r_p = 10 and 100 µm.

As for the electron density, it was experimentally measured using optical emission spectroscopy. The emission profiles are highly sensitive to plasma conditions, including temperature (Doppler broadening), pressure (van der Waals broadening), and the density of charged species (Stark broadening). Considering that the Hα line is clearly evident in the spectra recorded herein, and that the Stark broadening of this line is well documented [50–52], the temporal evolution of Hα emission (integration time = 20 ns, 250 averaged discharges) was used to determine the electron density of the plasma. The results illustrated in Fig. 9a show that the Hα line exhibits relatively strong broadening (> 5 nm), with the Stark broadening ($\Delta\lambda_{Stark}$) being the most dominant contributing factor. To estimate $\Delta\lambda_{Stark}$, the spectral data was fitted to a Lorentzian profile, as shown in Fig. 9b. Finally, the estimated value of $\Delta\lambda_{Stark}$ was used to calculate n_e at various times during discharge, according to (8) [50],

$$\Delta\lambda_{Stark}(nm) = 0.549\left(\frac{n_e(m^{-3})}{10^{23}}\right)^{0.67965} \tag{8}$$

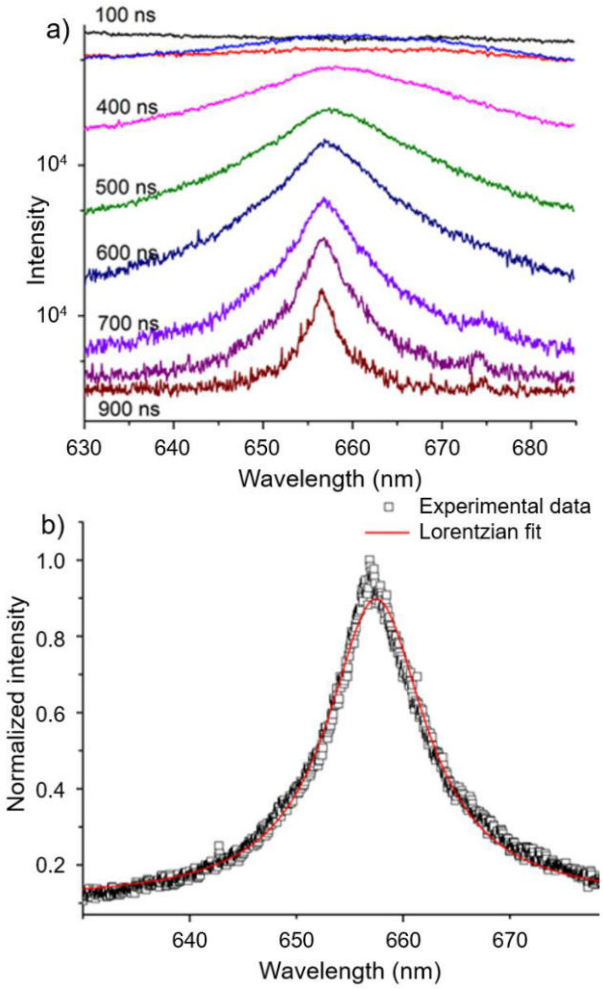

Fig. 9. a) Evolution of Hα line as a function of time. b) Lorentzian fit of the 700 ns Hα line.

Considering that during the first 300 ns of discharge the spectra are dominated by continuum radiation, n_e was determined based on data collected between 400 and 900 ns only. Overall, the electron density continuously decreases from 271×10^{23} m^{-3} at 400 ns to 15×10^{23} m^{-3} at 900 ns. Such relatively high values can only be achieved under high pressure conditions, which further supports our assumption that the pressure is in the order of tens of bars; these values are in agreement with values already reported in literature [7–8]. However, since the contribution of n_e to ρ_p is determined according to $\ln(n_e{}^{-1/2})$, then high electron densities will have

an insignificant influence on plasma resistivity, as shown in Table III, for n_e values in the range of 15.1-271.6 $\times 10^{23}$ m^{-3}, $\ln(n_e^{-1/2})$ varies between -29.3 and -27.8. This indicates that influence of n_e temporal-variation can be neglected. The value considered in further calculations is 271×10^{23} m^{-3}.

TABLE III
TEMPORAL VARIATION OF ELECTRON DENSITY.

Time (ns)	400	500	600	700	800	900
n_e ($\times 10^{23}$ m^{-3})	271.6	147.1	83.9	44.1	26.6	15.1
$\ln(n_e^{-1/2})$	-29.3	-28.9	-28.7	-28.4	-28.1	-27.8

The electron temperature was calculated at different times using the two values of plasma radius discussed above (10 and 100 µm), and the resulting temporal evolution of T_e is presented in Fig. 10. Initially, T_e rapidly increases to a peak value of ~25 eV (10 µm radius) or 1.2 eV (100 µm radius). Considering that previous studies on similar discharges report electron temperatures less than 5 eV [31, 53, 54], it seems that the emission dimension of the plasma (100 µm) is more suited for T_e calculation than the impact dimension (10 µm). This is consistent with experimental studies on plasma emission imaging, e.g., [23], as well as on simulation study, e.g., [55], showing that the plasma radius is about 100 µm, relatively larger than the impact radius (about 10 µm). After the initial increase, T_e exhibits an oscillating behavior with a decreasing slope, a dynamic that is similar to the current waveform. The temporal evolution of the plasma radius was assessed using a constant T_e value of 0.75 eV ((5) and (6)). As shown in Fig. 10c, r_p increases rapidly to a maximum of 115-145 µm at ~0.32 µs (i.e., 20 ns after breakdown), then it decreases while oscillating, like T_e.

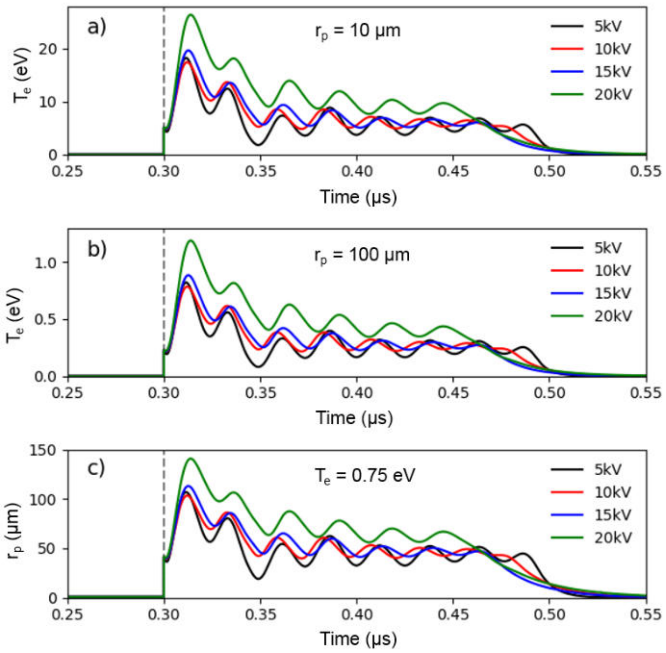

Fig. 10. Temporal evolution of electron temperature at a) r_p = 10 µm and b) r_p = 100 µm (applied voltage = 5, 10, 15, and 20 kV, pulse width = 500 ns). c) Temporal evolution of plasma radius at T_e = 0.75 eV (applied voltage = 5, 10, 15, and 20 kV, pulse width = 500 ns). The dashed line indicates the breakdown.

Interestingly, the acquisition of the plasma radiation using a photomultiplier (PM), simultaneously with the electrical characteristics, shows oscillation behavior that is synchronized with the current (shifted by ~25 ns), Fig. 11. Such an oscillation of the radiation clearly indicates that the plasma kinetics (excitation, deexcitation, etc.) change, and such a change can be related to oscillation of the electron temperature already observed in Fig. 10b; the oscillation of electron temperature can be associated to the formation of space charge in the plasma.

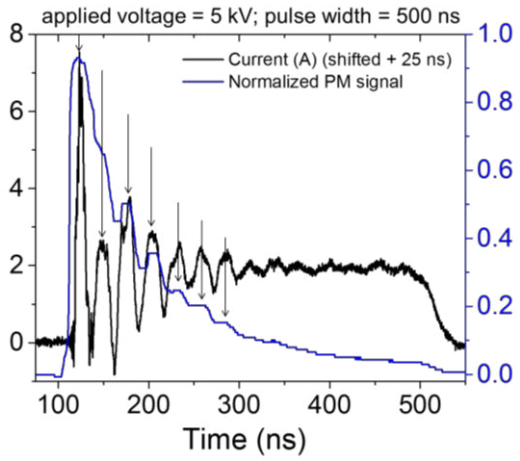

Fig. 11. Electrical current waveform and its correspondence PM signal acquired for a discharge at an applied voltage of 5 kV and pulse width of 500 ns.

Considering that the parameters of pulsed plasmas, such as radius, electron temperature, and electron density, vary with time, it is extremely difficult to study these plasmas experimentally or theoretically. Moreover, the assumption of cylindrical symmetry in the plasma channel is far from real, seeing that plasma emissions are generally spherical-like [23]. The homogeneity of T_e and n_e inside the plasma is also doubtful due to the coexistence of multiple interfaces (plasma-electrode, plasma-water, plasma-vapor, etc.), as well as to space charge, electron-ion recombination, and nanoparticles. In light of these limitations, the Spitzer formula (7) that assumes a Maxwellian distribution is probably not well adapted for the analysis of discharges in liquid. At this stage, our study shows that the equivalent electrical circuit of a spark discharge in water maybe of interest as it provides temporal evolution of plasma properties at a time-scale unachievable experimentally. Therefore, to further develop this field of research, it becomes crucial to establish a plasma model that considers the various physical phenomena reported in spark discharges, such as streamer ignition, branching, charge creation, and dynamic changes in the distribution function. On the other hand, the exclusion of high electron temperature corresponding to r_p = 10 µm from our calculations is yet another limitation, especially considering that the electron energy distribution acquired under micro gap conditions shows electrons with energies as high as ~35 eV [56]. To the best of our knowledge, the temporal evolution of electron temperature in plasmas in liquid has not yet been reported, and only the average values are available. However, Inoue et al. [31] have recently demonstrated that the

spatial distribution of electron temperature varies with time. Despite the differences in experimental setups and discharge conditions, the study reports T_e values around 1 eV, with oscillating behavior during discharge. This agrees well with our results.

V. Conclusion

In this study, we investigate the equivalent electrical circuit of a spark discharge in water induced by a pulsed high voltage. The electrical characteristics of this discharge (current and voltage) were experimentally determined under various conditions of applied voltage and pulse width and used to theoretically calculate plasma properties such as inductance and resistance. These properties were optimized by minimizing the difference between the simulated and experimental electrical current values.

The inductance of the cylindrical plasma channel was assumed to be time independent, and its average value was used to study the temporal evolution of plasma resistivity, according to a Mayr-type model. Considering that resistivity depends on electron temperature and density (Spitzer formula), the evolution of these parameters as a function of time was also assessed. However, the influence of electron density (measured experimentally) on plasma resistivity was taken to be insignificant, and so, only the temporal variation in electron temperature was analyzed. The obtained results demonstrate that electron temperature is highly dependent on plasma radius, with the impact radius (~10 µm) yielding a peak value of approximately ~25 eV. The plasma emission radius (~100 µm), on the other hand, results in an electron temperature of ~1.2 eV; this value is more realistic because it is comparable to values reported in literature. Electron temperature oscillates as a function of time, probably due to the formation of space charges. Similar oscillations are also detected in the radiation emitted by the plasma acquired using a PM.

Our approach in determining some plasma properties based on an equivalent electrical circuit is approximative, at best. Nevertheless, the results reported herein demonstrate that the temporal evolution of electrical current can be directly related to variations in plasma properties, mainly to electron temperature.

References

[1] Kolb J F, Joshi R P, Xiao S and Schoenbach K H 2008 Streamers in water and other dielectric liquids *Journal of Physics D: Applied Physics* **41** 234007

[2] Beroual A 1993 Electronic and gaseous processes in the prebreakdown phenomena of dielectric liquids *Journal of Applied Physics* **73** 4528–33

[3] Lesaint O, Gournay P and Tobazeon R 1991 Investigations on transient currents associated with streamer propagation in dielectric liquids *IEEE Transactions on Electrical Insulation* **26** 699–707

[4] Horikoshi S and Serpone N 2017 In-liquid plasma: a novel tool in the fabrication of nanomaterials and in the treatment of wastewaters *RSC Adv.* **7** 47196–218

[5] Hamdan A, Liu J-L and Cha M S 2018 Microwave Plasma Jet in Water: Characterization and Feasibility to Wastewater Treatment *Plasma Chem Plasma Process* **38** 1003–20

[6] Hamdan A, Profili J and Cha M S 2020 Microwave Plasma Jet in Water: Effect of Water Electrical Conductivity on Plasma Characteristics *Plasma Chem Plasma Process* **40** 169–85

[7] Descoeudres A, Hollenstein C, Demellayer R and Wälder G 2004 Optical emission spectroscopy of electrical discharge machining plasma *J. Phys. D: Appl. Phys.* **37** 875–882

[8] Descoeudres A, Hollenstein C, Wälder G and Perez R 2005 Time-resolved imaging and spatially-resolved spectroscopy of electrical discharge machining plasma *J. Phys. D: Appl. Phys.* **38** 4066–4073

[9] Huang X and Huang R 2017 Application of Underwater Electric Discharge Machining in Nuclear Power Plant 2017 25th International Conference on Nuclear Engineering (American Society of Mechanical Engineers Digital Collection)

[10] Belmonte T, Hamdan A, Kosior F, Noël C and Henrion G 2014 Interaction of discharges with electrode surfaces in dielectric liquids: application to nanoparticle synthesis *J. Phys. D: Appl. Phys.* **47** 224016

[11] Glad X, Profili J, Cha M S and Hamdan A 2020 Synthesis of copper and copper oxide nanomaterials by electrical discharges in water with various electrical conductivities *Journal of Applied Physics* **127** 023302

[12] Hamdan A, Kabbara H, Noël C, Ghanbaja J, Redjaimia A and Belmonte T 2018 Synthesis of two-dimensional lead sheets by spark discharge in liquid nitrogen *Particuology* **40** 152–9

[13] Rietz E B 1953 Operating Mechanisms for High-Capacity High-Voltage Oil Circuit Breakers [includes discussion] *Transactions of the American Institute of Electrical Engineers. Part III: Power Apparatus and Systems* **72** 256–63

[14] Chandrasekar S and Montanari G C 2014 Analysis of partial discharge characteristics of natural esters as dielectric fluid for electric power apparatus applications *IEEE Transactions on Dielectrics and Electrical Insulation* **21** 1251–9

[15] Forster E O 1993 Partial discharges and streamers in liquid dielectrics-the significance of the inception voltage *IEEE Transactions on Electrical Insulation* **28** 941–6

[16] Shneider M N, Pekker M and Fridman A 2012 Theoretical study of the initial stage of sub-nanosecond pulsed breakdown in liquid dielectrics *IEEE Transactions on Dielectrics and Electrical Insulation* **19** 1579–82

[17] Seepersad Y, Pekker M, Shneider M N, Fridman A and Dobrynin D 2013 Investigation of positive and negative modes of nanosecond pulsed discharge in water and electrostriction model of initiation *J. Phys. D: Appl. Phys.* **46** 355201

[18] Starikovskiy A, Yang Y, Cho Y I and Fridman A 2011 Non-equilibrium plasma in liquid water: dynamics of generation and quenching *Plasma Sources Science and Technology* **20** 024003

[19] Starikovskiy A 2013 Pulsed nanosecond discharge development in liquids with various dielectric permittivity constants *Plasma Sources Sci. Technol.* **22** 012001

[20] Fujita H, Kanazawa S, Ohtani K, Komiya A, Kaneko T and Sato T 2014 Initiation process and propagation mechanism of positive streamer discharge in water *Journal of Applied Physics* **116** 213301

[21] Li X D, Liu Y, Zhou G Y, Liu S W, Li Z Y and Lin F C 2017 Subsonic streamers in water: initiation, propagation and morphology *J. Phys. D: Appl. Phys.* **50** 255301

[22] Pekker M and Shneider M N 2015 Pre-breakdown cavitation nanopores in the dielectric fluid in the inhomogeneous, pulsed electric fields *J. Phys. D: Appl. Phys.* **48** 424009

[23] Hamdan A, Marinov I, Rousseau A and Belmonte T 2013 Time-resolved imaging of nanosecond-pulsed micro-discharges in heptane *J. Phys. D: Appl. Phys.* **47** 055203

[24] Ceccato P H, Guaitella O, Gloahec M R L and Rousseau A 2010 Time-resolved nanosecond imaging of the propagation of a corona-like plasma discharge in water at positive applied voltage polarity *J. Phys. D: Appl. Phys.* **43** 175202

[25] Marinov I, Starikovskaia S and Rousseau A 2014 Dynamics of plasma evolution in a nanosecond underwater discharge *J. Phys. D: Appl. Phys.* **47** 224017

[26] Hamdan A, Noel C, Kosior F, Henrion G and Belmonte T 2013 Impacts created on various materials by micro-discharges in heptane: Influence of the dissipated charge *Journal of Applied Physics* **113**

[27] Hamdan A, Noël C, Ghanbaja J, Migot-Choux S and Belmonte T 2013 Synthesis of platinum embedded in amorphous carbon by micro-gap discharge in heptane *Materials Chemistry and Physics* **142** 199–206

[28] Simeni M S, Baratte E, Zhang C, Frederickson K and Adamovich I V 2018 Electric field measurements in nanosecond pulse discharges in air over liquid water surface *Plasma Sources Sci. Technol.* **27** 015011

[29] Rond C, Desse J M, Fagnon N, Aubert X, Er M, Vega A and Duten X 2018 Time-resolved diagnostics of a pin-to-pin pulsed discharge in water: pre-breakdown and breakdown analysis *Journal of Physics D: Applied Physics* **51** 1–11

[30] Babicky V, Clupek M and Lukes P 2017 Determination of electrical characteristics of nanosecond discharge in liquid *2017 IEEE 19th International Conference on Dielectric Liquids (ICDL)* 2017 IEEE 19th International Conference on Dielectric Liquids (ICDL) pp 1–4

[31] Inoue K, Takahashi S, Sakakibara N, Toko S, Ito T and Terashima K 2020 Spatiotemporal optical emission spectroscopy to estimate electron density and temperature of plasmas in solution *J. Phys. D: Appl. Phys.*

[32] Miron C, Zhuang J, Balcerak M, Holub M, Kruth A, Quade A, Sava I, Weltmann K-D and Kolb J F 2016 Cobalt Containing Polyimide Films Treated by Nanosecond Pulsed Electrical Discharges in Water *IEEE Transactions on Plasma Science* **44** 2708–14

[33] Šimek M, Pongrác B, Babický V, Člupek M and Lukeš P 2017 Luminous phase of nanosecond discharge in deionized water: morphology, propagation velocity and optical emission *Plasma Sources Sci. Technol.* **26** 07LT01

[34] Belinger A, Naudé N, Cambronne J P and Caruana D 2014 Plasma synthetic jet actuator: electrical and optical analysis of the discharge *Journal of Physics D: Applied Physics* **47** 345202

[35] Kao C C and Shih A J 2006 Sub-nanosecond monitoring of micro-hole electrical discharge machining pulses and modeling of discharge ringing *International Journal of Machine Tools and Manufacture* **46** 1996–2008

[36] Asad A B M A, Islam M T, Masaki T, Rahman M and Wong Y S 2018 Analysis of micro-EDM electric characteristics employing plasma property *CIRP Journal of Manufacturing Science and Technology* **20** 36–50

[37] Park K-H, Lee H-Y, Asif M, Lee B-W, Shin T-Y and Gu C-W 2017 Assessment of various kinds of AC black-box arc models for DC circuit breaker *2017 4th International Conference on Electric Power Equipment - Switching Technology (ICEPE-ST)* 2017 4th International Conference on Electric Power Equipment - Switching Technology (ICEPE-ST) pp 465–9

[38] Ohtaka T, Kertész V and Paul Smeets R P 2018 Novel Black-Box Arc Model Validated by High-Voltage Circuit Breaker Testing *IEEE Transactions on Power Delivery* **33** 1835–44

[39] Mahajan N S, Patil K R and Shembekar S M 2013 Electric Arc model for High Voltage Circuit Breakers Based on MATLAB/SIMULINK **1** 7

[40] Hussey T W, Davis K J, Lehr J M, Roderick N F, Pate R C and Kunhardt E 1999 Dynamics of nanosecond spark-gap channels *Digest of Technical Papers. 12th IEEE International Pulsed Power Conference. (Cat. No.99CH36358)* 12th International Pulsed Power Conference vol 2 (Monterey, CA, USA: IEEE) pp 1171–4

[41] Braginskii S I 1958 THEORY OF THE DEVELOPMENT OF A SPARK CHANNEL vol VOLUME 34(7), NUMBER 6 (SOVIET PHYSICS JETP)

[42] Schavemaker P H and Slui L van der 2000 An improved Mayr-type arc model based on current-zero measurements [circuit breakers]

[43] J B Stefan Karpinski, Viral Shah, Alan Edelman, et The Julia Language *https://julialang.org/*

[44] ODE Solvers · DifferentialEquations.jl *https://docs.juliadiffeq.org/stable/solvers/ode_solve/*

[45] Persephonis P, Vlachos K, Georgiades C and Parthenios J 1992 The inductance of the discharge in a spark gap *Journal of Applied Physics* **71** 4755–62

[46] Hamdan A, Audinot J-N, Noel C, Kosior F, Henrion G and Belmonte T 2013 Interaction of micro-discharges in heptane with metallic multi-layers *Applied Surface Science* **274** 378–91

[47] Hamdan A, Audinot J-N, Migot-Choux S, Noel C, Kosior F, Henrion G and Belmonte T 2013 Interaction of Discharges in Heptane with Silicon Covered by a Carpet of Carbon Nanotubes *Advanced Engineering Materials* **15** 885–92

[48] Heaney M 2003 Electrical Conductivity and Resistivity *Electrical Measurement, Signal Processing, and Displays* pp 7–1 to 7

[49] Kuritsyn A, Yamada M, Gerhardt S, Ji H, Kulsrud R and Ren Y 2006 Measurements of the parallel and transverse Spitzer resistivities during collisional magnetic reconnection *Physics of Plasmas* **13** 055703

[50] Gigosos M A, González M Á and Cardeñoso V 2003 Computer simulated Balmer-alpha, -beta and -gamma Stark line profiles for non-equilibrium plasmas diagnostics *Spectrochimica Acta Part B: Atomic Spectroscopy* **58** 1489–504

[51] Gigosos M A, Fraile J and Torres F 1985 Hydrogen Stark profiles: A simulation-oriented mathematical simplification *Phys. Rev. A* **31** 3509–11

[52] Gigosos M A and Cardeñoso V 1996 New plasma diagnosis tables of hydrogen Stark broadening including ion dynamics *J. Phys. B: At. Mol. Opt. Phys.* **29** 4795–4838

[53] Namihira T, Sakai S, Yamaguchi T, Yamamoto K, Yamada C, Kiyan T, Sakugawa T, Katsuki S and Akiyama H 2007 Electron Temperature and Electron Density of Underwater Pulsed Discharge Plasma Produced by Solid-State Pulsed-Power Generator *IEEE Transactions on Plasma Science* **35** 614–8

[54] Dobrynin D, Seepersad Y, Pekker M, Shneider M, Friedman G and Fridman A 2013 Non-equilibrium nanosecond-pulsed plasma generation in the liquid phase (water, PDMS) without bubbles: fast imaging, spectroscopy and leader-type model *J. Phys. D: Appl. Phys.* **46** 105201

[55] Hamdan A, Kosior F, Noel C, Henrion G, Audinot J-N, Gries T and Belmonte T 2013 Plasma-surface interaction in heptane *Journal of Applied Physics* **113** 213303

[56] Go, D.B. and Venkattraman, A., 2014. Microscale gas breakdown: ion-enhanced field emission and the modified Paschen's curve. *J. Phys. D: Appl. Phys.* **47**(50) 503001.

Conclusion

Ce mémoire s'est principalement intéressé aux décharges « Spark » dans les liquides diélectriques. La caractérisation électrique de ces décharges, leurs analyses détaillées, couplées et la réalisation d'un circuit équivalent, nous permet de déterminer des paramètres plasma tels que l'évolution temporelle de la température électronique. Cependant, la physique de ces plasmas est très complexe et nécessite des études simultanées sur les conditions de pression, température et densité. Ceci est un 1er pas dans la connaissance des conditions expérimentales lors de la synthèse de nanoparticules par décharges impulsionnelles dans des liquides diélectriques.

Les contributions apportées durant cette maîtrise sont les suivantes :

- Le développement d'une alimentation pulsée à bas prix permettant des décharges dans l'eau distillée avec des tensions appliqués ≈ 2.5 kV et une dynamique RLC durant la décharge d'une durée d'environ 500 ns.
- Le développement d'un circuit équivalent pour le système électrique à l'Université de Montréal expliquant les signaux électriques observés par une inductance plasma non-négligeable et une résistance qui évolue dans le temps. Après avoir lié la résistivité du plasma à la température et à la densité électronique, nous étions capables de proposer une évolution temporelle de la température électronique, sachant que la densité électronique est déterminée expérimentalement.

Ce projet qui porte sur la compréhension des décharges électriques dans les liquides et leurs applications à la synthèse de nanoparticules est terminé pour ma part, cependant des étudiants successifs vont continuer à explorer la physique des plasmas dans ces conditions particulière.

Il est également à noter que l'étude des particules ainsi créées avec des conditions reproductibles (système à l'UdeM) est présente en annexe et porte sur la capacité à produire des oxydes de cobalt ou de nickel via des décharges dans l'eau.

Références bibliographiques

[1] J. Jeevanandam, A. Barhoum, Y. S. Chan, A. Dufresne, et M. K. Danquah, « Review on nanoparticles and nanostructured materials: history, sources, toxicity and regulations », *Beilstein J Nanotechnol*, vol. 9, p. 1050-1074, avr. 2018, doi: 10.3762/bjnano.9.98.

[2] Y. Qing *et al.*, « Potential antibacterial mechanism of silver nanoparticles and the optimization of orthopedic implants by advanced modification technologies », *Int J Nanomedicine*, vol. 13, p. 3311-3327, juin 2018, doi: 10.2147/IJN.S165125.

[3] J.-F. Hochepied, « Évaluation des risques liés aux nanomatériaux | Anses - Agence nationale de sécurité sanitaire de l'alimentation, de l'environnement et du travail », *ANSES*, sept. 21, 2016. https://www.anses.fr/fr/content/%C3%A9valuation-des-risques-li%C3%A9s-aux-nanomat%C3%A9riaux (consulté le juin 21, 2019).

[4] INRA, « Additif alimentaire E171 : les premiers résultats de l'exposition orale aux nanoparticules de dioxyde de titane », janv. 20, 2017. http://presse.inra.fr%2FCommuniques-de-presse%2FAdditif-alimentaire-E171 (consulté le juin 21, 2019).

[5] S. A. Billings, F. M. Boland, et H. Nicholson, « Electric arc furnace modelling and control », *Automatica*, vol. 15, n° 2, p. 137-148, mars 1979, doi: 10.1016/0005-1098(79)90065-7.

[6] F. Yang *et al.*, « Low-voltage circuit breaker arcs—simulation and measurements », *Journal of Physics D: Applied Physics*, vol. 46, n° 27, p. 273001, juill. 2013, doi: 10.1088/0022-3727/46/27/273001.

[7] J.-J. J. Hajjar et R. Reif, « Characteristics of thin film transistors fabricated in polysilicon films deposited by plasma enhanced chemical vapor deposition », *Journal of Electronic Materials*, vol. 19, n° 12, p. 1403-1409, déc. 1990, doi: 10.1007/BF02662830.

[8] Q. H. Trinh, Md. M. Hossain, S. H. Kim, et Y. S. Mok, « Tailoring the wettability of glass using a double-dielectric barrier discharge reactor », *Heliyon*, vol. 4, n° 1, p. e00522, janv. 2018, doi: 10.1016/j.heliyon.2018.e00522.

[9] T. G. Klämpfl *et al.*, « Cold Atmospheric Air Plasma Sterilization against Spores and Other Microorganisms of Clinical Interest », *Appl Environ Microbiol*, vol. 78, n° 15, p. 5077-5082, août 2012, doi: 10.1128/AEM.00583-12.

[10] O. Eichwald *et al.*, « Titre : Etude d'un réacteur de post-décharge d'azote en flux dédié à la décontamination de l'instrumentation médicale. Application à la détermination des probabilités de recombinaison hétérogène de l'azote atomique », p. 188.

[11] Plasmaprometeo, « Plasma », *Plasmaprometeo*, mars 07, 2013. http://www.plasmaprometeo.unimib.it/?page_id=20 (consulté le juin 21, 2019).

[12] K. Wiesemann, « A Short Introduction to Plasma Physics », p. 38.

[13] « Magnétostatique ». https://www.f-legrand.fr/scidoc/docmml/sciphys/elecmag/magnetostat/magnetostat.html (consulté le juin 25, 2020).

[14] Yu. K. Kurilenkov et A. A. Valuev, « The Electrical Conductivity of Plasma in Wide Range of Charge Densities », *Beiträge aus der Plasmaphysik*, vol. 24, n° 3, p. 161-171, 1984, doi: 10.1002/ctpp.19840240304.

[15] V. E. Fortov, I. T. ÎAkubov, et A. G. Khrapak, *Physics of strongly coupled plasma*. Oxford: Oxford University Press, 2006.

[16] A. Kuritsyn, M. Yamada, S. Gerhardt, H. Ji, R. Kulsrud, et Y. Ren, « Measurements of the parallel and transverse Spitzer resistivities during collisional magnetic reconnection », *Physics of Plasmas*, vol. 13, n° 5, p. 055703, mai 2006, doi: 10.1063/1.2179416.

[17] J. Sengupta, « Carbon Nanotube Fabrication at Industrial Scale », in *Handbook of Nanomaterials for Industrial Applications*, Elsevier, 2018, p. 172-194.
[18] V. Malka, J. Faure, Y. A. Gauduel, E. Lefebvre, A. Rousse, et K. T. Phuoc, « Principles and applications of compact laser–plasma accelerators », *Nature Physics*, vol. 4, n° 6, p. 447-453, juin 2008, doi: 10.1038/nphys966.
[19] C. Douat, « Etude d'un micro-jet de plasma à pression atmosphérique », janv. 2016. doi: 10.13140/RG.2.1.3041.8001.
[20] A. Tilmatine, « MECANISMES DE CLAQUAGE DES ISOLANTS GAZEUX ». University of Sidi-Bel-Abbes, Consulté le: juin 21, 2019. [En ligne]. Disponible sur: https://www.univ-sba.dz/fsi/downloads/ETL437-Chapitre_3.pdf.
[21] R. Tobazéon, « Préclaquage et claquage des liquides diélectriques », p. 39, 1997.
[22] A. Fridman, A. Chirokov, et A. Gutsol, « Non-Thermal Atmospheric Pressure Discharges », *Journal of Physics D: Applied Physics*, vol. 38, p. R1, janv. 2005, doi: 10.1088/0022-3727/38/2/R01.
[23] R. LANDFRIED, « Contribution à l'Étude de la Transition Décharge Luminescente - Arc Électrique dans l'Air et l'Argon au Voisinage de la Pression Atmosphérique », STiT2, 2011.
[24] L. P. Babich et T. V. Loiko, « Generalized Paschen's Law for Overvoltage Conditions », *IEEE Transactions on Plasma Science*, vol. 44, p. 3243-3248, 2016, doi: 10.1109/TPS.2016.2629022.
[25] Université de Genève, « LOI DE PASCHEN ». Université de Genève, janv. 10, 2019, Consulté le: juin 21, 2019. [En ligne]. Disponible sur: https://www.unige.ch/sciences/physique/tp/tpi/Liens/Protocoles/Loi_de_Paschen_19.pdf.
[26] L. B. Loeb et J. M. Meek, « The Mechanism of Spark Discharge in Air at Atmospheric Pressure. I », *Journal of Applied Physics*, vol. 11, n° 6, p. 438-447, juin 1940, doi: 10.1063/1.1712792.
[27] L. B. Loeb et J. M. Meek, « The Mechanism of Spark Discharge in Air at Atmospheric Pressure. II », *Journal of Applied Physics*, vol. 11, n° 7, p. 459-474, juill. 1940, doi: 10.1063/1.1712796.
[28] H. Raether, « Die Entwicklung der Elektronenlawine in den Funkenkanal », p. 26.
[29] A. B. M. A. Asad, M. T. Islam, T. Masaki, M. Rahman, et Y. S. Wong, « Analysis of micro-EDM electric characteristics employing plasma property », *CIRP Journal of Manufacturing Science and Technology*, vol. 20, p. 36-50, janv. 2018, doi: 10.1016/j.cirpj.2017.09.005.
[30] V. Lj. Marković, S. R. Gocić, et M. K. Radović, « Breakdown probability and influence on breakdown delay », *The European Physical Journal Applied Physics*, vol. 6, n° 3, p. 303-307, juin 1999, doi: 10.1051/epjap:1999188.
[31] D. Yan, D. C. Bian, F. Ren, Z. Q. Yin, J. C. Zhao, et S. Q. Niu, « Study on Breakdown Delay Characteristics Based on High-voltage Pulse Discharge in Water with Hydrostatic Pressure », *Journal of Power Technologies*, vol. 97, n° 2, p. 89-102, juill. 2017.
[32] G. Fan, H. Shi, L. Weixi, et X. Yanzhao, « The breakdown time delay and jitter of different cathode materials under nanosecond pulse in N2 », in *2017 1st International Conference on Electrical Materials and Power Equipment (ICEMPE)*, Xi'an, China, mai 2017, p. 525-528, doi: 10.1109/ICEMPE.2017.7982187.
[33] C. L. da Silva et V. P. Pasko, « Dynamics of streamer-to-leader transition at reduced air densities and its implications for propagation of lightning leaders and gigantic jets », *Journal of Geophysical Research: Atmospheres*, vol. 118, n° 24, p. 13,561-13,590, 2013, doi: 10.1002/2013JD020618.
[34] Ahmad Hamdan, « Microdécharges dans l'heptane liquide : caractérisation et applications au traitement local des matériaux et à la synthèse de nanomatériaux », Thèse doctorat, Université de Lorraine, 2013.
[35] P. Bruggeman et C. Leys, « Non-thermal plasmas in and in contact with liquids », *Journal of Physics D: Applied Physics*, vol. 42, n° 5, p. 053001, mars 2009, doi: 10.1088/0022-3727/42/5/053001.
[36] S. Théoleyre, « Techniques de coupure en moyenne tension », p. 29, 1999.

[37] H. Kabbara, « Élaboration de nanoparticules par décharges spark nanosecondes dans des liquides diélectriques: compréhension des mécanismes élémentaires et synthèse de composites », Université de Lorraine.
[38] A. Starikovskiy, Y. Yang, Y. I. Cho, et A. Fridman, « Non-equilibrium plasma in liquid water: dynamics of generation and quenching », *Plasma Sources Science and Technology*, vol. 20, n° 2, p. 024003, avr. 2011, doi: 10.1088/0963-0252/20/2/024003.
[39] V. I. Ushakov, Éd., *Impulse breakdown of liquids*. Berlin ; New York: Springer, 2007.
[40] Y. Seepersad, D. Dobrynin, M. Pekker, M. N. Shneider, et A. Fridman, « To the electrostrictive mechanism of nanosecond-pulsed breakdown in liquid phase », p. 9.
[41] T. Belmonte, H. Kabbara, C. Noël, et R. Pflieger, « Analysis of Zn I emission lines observed during a spark discharge in liquid nitrogen for zinc nanosheet synthesis », *Plasma Sources Science and Technology*, vol. 27, n° 7, p. 074004, juill. 2018, doi: 10.1088/1361-6595/aacee2.
[42] D. Oshita, S. H. R. Hosseini, Y. Miyamoto, K. Mawatari, et H. Akiyama, « Study of underwater shock waves and cavitation bubbles generated by pulsed electric discharges », *IEEE Transactions on Dielectrics and Electrical Insulation*, vol. 20, n° 4, p. 1273-1278, août 2013, doi: 10.1109/TDEI.2013.6571444.
[43] I. Marinov, S. Starikovskaia, et A. Rousseau, « Dynamics of plasma evolution in a nanosecond underwater discharge », *J. Phys. D: Appl. Phys.*, vol. 47, n° 22, p. 224017, mai 2014, doi: 10.1088/0022-3727/47/22/224017.
[44] J. Tomko *et al.*, « Cavitation bubble dynamics and nanoparticle size distributions in laser ablation in liquids », *Colloids and Surfaces A: Physicochemical and Engineering Aspects*, vol. 522, p. 368-372, juin 2017, doi: 10.1016/j.colsurfa.2017.03.030.
[45] T. Belmonte, « Synthèse ultrarapide de nanoparticules par claquage dans des liquides diélectriques », *Reflets de la physique*, n° 51, p. 22-27, déc. 2016, doi: 10.1051/refdp/201651022.
[46] C. Mauger, Q. Leclere, et P. Coupé, « Caractérisation optique et acoustique d'une bulle générée par focalisation laser », p. 10, 2015.
[47] A. Hamdan, C. Noel, F. Kosior, G. Henrion, et T. Belmonte, « Dynamics of bubbles created by plasma in heptane for micro-gap conditions », *The Journal of the Acoustical Society of America*, vol. 134, n° 2, p. 991-1000, août 2013, doi: 10.1121/1.4812255.
[48] INRS, « Nanomatériaux, nanoparticules. Terminologie et définitions - Risques - INRS », *INRS*, août 08, 2014. http://www.inrs.fr/risques/nanomateriaux/terminologie-definition.html (consulté le juin 24, 2019).
[49] W. Zhang, L. Meyrat, T. Kesavan, et F. Mahjoub, « À quoi servent les nanoparticules ? – Les nanoparticules dans l'alimentation », *Les nanoparticules dans l'alimentation*, 2017. index.html (consulté le juin 21, 2019).
[50] A. Cros-Gagneux, « Nanocristaux luminescent de phosphure d'indium : synthèse et chimie de surface », Université Toulouse III - Paul Sabatier, France.
[51] S. Iravani, H. Korbekandi, S. V. Mirmohammadi, et B. Zolfaghari, « Synthesis of silver nanoparticles: chemical, physical and biological methods », *Res Pharm Sci*, vol. 9, n° 6, p. 385-406, 2014.
[52] H. D. Beyene, A. A. Werkneh, H. K. Bezabh, et T. G. Ambaye, « Synthesis paradigm and applications of silver nanoparticles (AgNPs), a review », *Sustainable Materials and Technologies*, vol. 13, p. 18-23, sept. 2017, doi: 10.1016/j.susmat.2017.08.001.
[53] S. Agnihotri, S. Mukherji, et S. Mukherji, « Size-controlled silver nanoparticles synthesized over the range 5–100 nm using the same protocol and their antibacterial efficacy », *RSC Advances*, vol. 4, n° 8, p. 3974-3983, 2014, doi: 10.1039/C3RA44507K.
[54] A. Radoń et D. Łukowiec, « Silver nanoparticles synthesized by UV-irradiation method using chloramine T as modifier: structure, formation mechanism and catalytic activity », *CrystEngComm*, vol. 20, n° 44, p. 7130-7136, nov. 2018, doi: 10.1039/C8CE01379A.

[55] D. Oseguera-Galindo, R. Machorro-Mejia, N. Bogdanchikova, et J. Mota-Morales, « Silver nanoparticles synthesized by laser ablation confined in urea choline chloride deep-eutectic solvent - ScienceDirect », mars 2016, doi: https://doi.org/10.1016/j.colcom.2016.03.004.
[56] B. O. Meuller *et al.*, « Review of Spark Discharge Generators for Production of Nanoparticle Aerosols », *Aerosol Science and Technology*, vol. 46, n° 11, p. 1256-1270, nov. 2012, doi: 10.1080/02786826.2012.705448.
[57] E. Hontañón *et al.*, « The transition from spark to arc discharge and its implications with respect to nanoparticle production », *Journal of Nanoparticle Research*, vol. 15, n° 9, sept. 2013, doi: 10.1007/s11051-013-1957-y.
[58] N. S. Tabrizi, « Generation of nanoparticles by spark discharge », University of Tarbiat Modarres, Tehran University of Leeds, Leeds, Iran, 2009.
[59] K.-H. Tseng, J.-L. Chiu, H.-L. Lee, C.-Y. Liao, H.-S. Lin, et Y.-S. Kao, « Preparation of Ag/Cu/Ti Nanofluids by Spark Discharge System and Its Control Parameters Study », *Advances in Materials Science and Engineering*, mars 10, 2015. https://www.hindawi.com/journals/amse/2015/694672/ (consulté le juin 26, 2020).
[60] M. Trad, A. Nominé, C. Noël, J. Ghanbaja, M. Tabbal, et T. Belmonte, « Evidence of alloy formation in CoNi nanoparticles synthesized by nanosecond-pulsed discharges in liquid nitrogen », *Plasma Processes and Polymers*, vol. n/a, n° n/a, p. e1900255, doi: 10.1002/ppap.201900255.
[61] X. Glad, J. Profili, M. S. Cha, et A. Hamdan, « Synthesis of copper and copper oxide nanomaterials by electrical discharges in water with various electrical conductivities », *Journal of Applied Physics*, vol. 127, n° 2, p. 023302, janv. 2020, doi: 10.1063/1.5129647.
[62] D. A. Hapidin, I. Saleh, M. M. Munir, et Khairurrijal, « Design and Development of a Series-configuration Mazzilli Zero Voltage Switching Flyback Converter as a High-voltage Power Supply for Needleless Electrospinning », *Procedia Engineering*, vol. 170, p. 509-515, janv. 2017, doi: 10.1016/j.proeng.2017.03.081.

ANNEXES

A. « Pulser » Laplace

Le dispositif de base disponible au LAPLACE est réalisé à base d'un circuit résonnant constitué d'une bobine haute tension « THT » alimentée par un circuit oscillant, lui-même alimenté par une source continue (tension secteur redressée et lissée). Un autotransformateur permet de régler la valeur de la tension en entrée, et donc la tension de sortie.

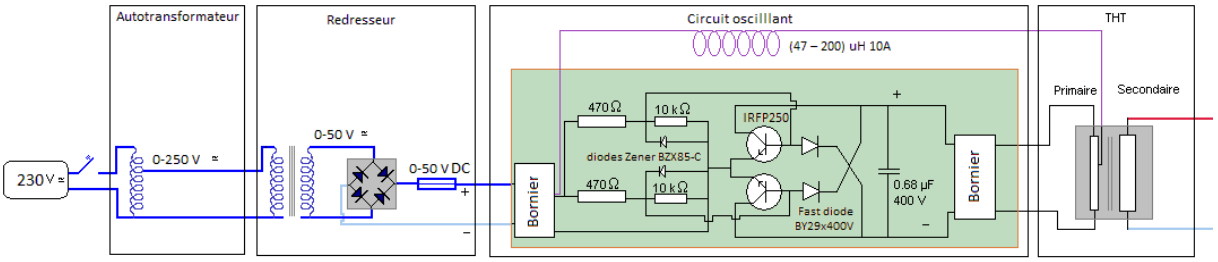

Figure 1.— Circuit électronique initialement présent au LAPLACE

L'alimentation étant déjà sur le site du Laplace et fonctionnelle, les composants utilisés sont connus à l'exception de la bobine THT qui est issue du recyclage. Les caractéristiques mesurées de la bobine THT sont récapitulées dans le Tableau 1 et la Figure 2 présente le schéma électrique du transformateur équivalent (Schéma de Kapp) :

Tableau 1.— Caractéristiques de la bobine THT

Imperfections	**Valeurs à 250kHz**
Reluctance du circuit magnétique ($L_{1)}$	750µH
Fuites de flux (l_s)	Non mesurable : considéré nul
Pertes fer	128,9 Ω (Très importante)
Pertes cuivre (Effet Joule)	Non mesurable : considéré nul

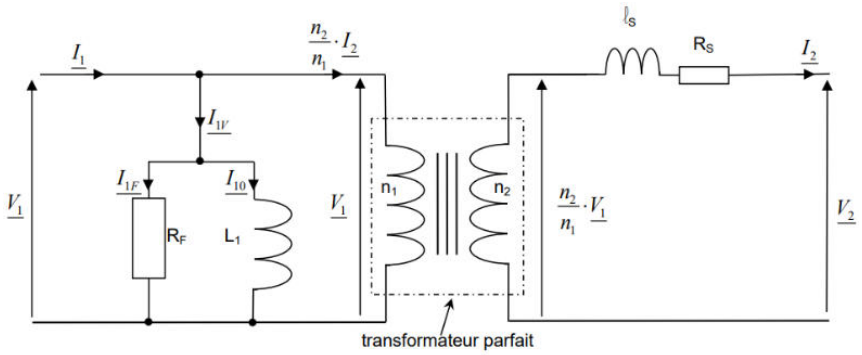

Figure 2.— Schéma de Kapp (Equivalent à un transformateur réel)

Le principe de fonctionnement de ce circuit oscillant repose sur les oscillations du circuit LC composé par une capacité et le bobinage primaire d'un transformateur.

Les oscillations démarrent quand la tension est appliquée, le courant traverse les deux bobinages du primaire et passe dans le drain des mosfet. Au même moment, une tension supérieure à V_{gs} est appliquée sur la base (« gate ») des mosfets. Ceux-ci sont alors passant. Cependant, les composants n'étant pas identiques, l'un des deux commute plus rapidement que le second, et par conséquent plus de courant passe par ce mosfet et par son enroulement primaire associé. Moins de courant est alors disponible pour le second mosfet et son enroulement : celui-ci se bloque. Le circuit LC vient alors d'être alimenté et la tension aux bornes de la capacité va devenir sinusoïdale [62].

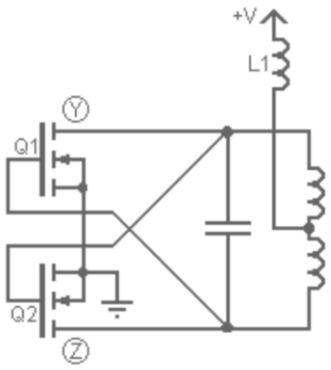

Figure 3.— Schéma simplifié de fonctionnement

Si Q1 est le premier à être devenu passant alors la tension au point Y est proche de 0 tandis que la tension au point Z augmente puis diminue sur la 1ère période d'oscillation du circuit LC. Quand la tension atteint Z, le courant dans le mosfet Q1 est drainé et il se ferme.

Sa fréquence de fonctionnement est donc donnée par la formule suivante : $f = \frac{2}{2\pi\sqrt{LC}}$. Soit, dans notre montage, $f \approx 30kHz$.

Sa conception permet la commutation des mosfet à une tension V_{gs} nulle, ce qui permet de limiter les pertes électriques de commutation par effet Joule.

Son désavantage est le fait qu'il s'agit d'un circuit en résonance et par conséquent la fréquence des impulsions générées est fixée par les valeurs de la capacité et de l'inductance des bobines. Cependant, vu que la charge du secondaire n'est pas stable, celle-ci va varier.

Le montage est alimenté par un pont de diode qui redresse le signal de 50 V (pic) issue d'un transformateur 220 V/35 V et vient charger le condensateur de lissage de 470 µF.

1. Modification du système expérimental

Le service électronique du LAPLACE a réalisé une commande actionnant un commutateur afin de limiter le nombre de décharges. Cela permet de couper l'alimentation en courant continu du circuit résonant afin de l'arrêter après un délai réglable avec précision. De plus, il est apparu que la première impulsion étant plus énergétique, c'est celui-ci qui est la plus intéressante pour l'application souhaitée. En effet plus l'énergie déposée (et la puissance instantanée) est grande plus la vaporisation des électrodes est importante [58].

Le circuit est donc composé de deux parties (puissance et commande) reliées entre elles par une fibre optique afin de limiter les interférences électriques.

La partie commande et constituée d'un module Arduino qui fut remplacé par la suite par un générateur de signaux (le rayonnement électromagnétique perturbant la commande de l'Arduino). Celui-ci alimente un émetteur pour fibre optique commandant un commutateur par réception du signal lumineux (voir Figure 4).

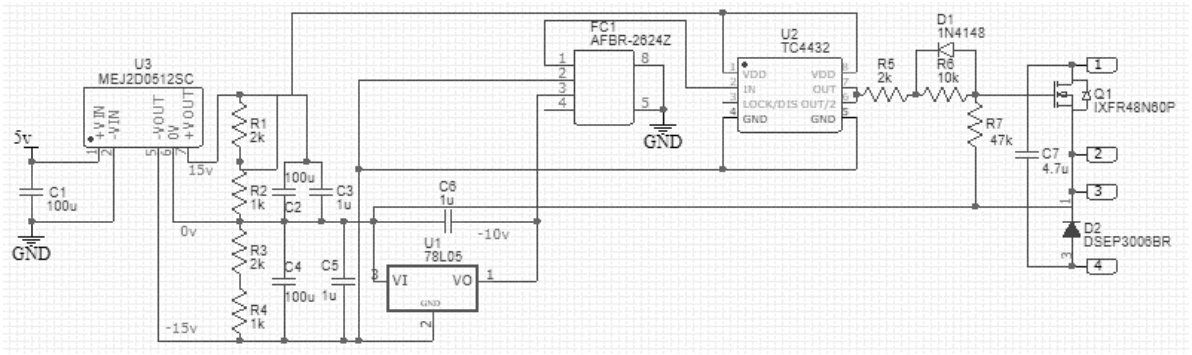

Figure 4.— Circuit électronique de commutation développée par le service électronique du LAPLACE et Gilles Charles (GREMI de l'Université d'Orléans, site de Bourges)

Pour finir, l'alimentation continu du circuit oscillant est changée par une alimentation de laboratoire afin de garantir une tension d'alimentation constante. (Précédemment le filtrage de la tension « secteur » fût sous-estimée causant un fonctionnement périodique à 50Hz (fréquence secteur Europe).

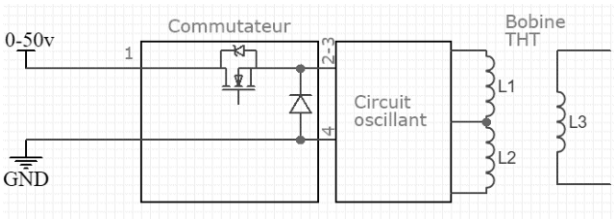

Figure 5.— Schéma simplifié de la commutation

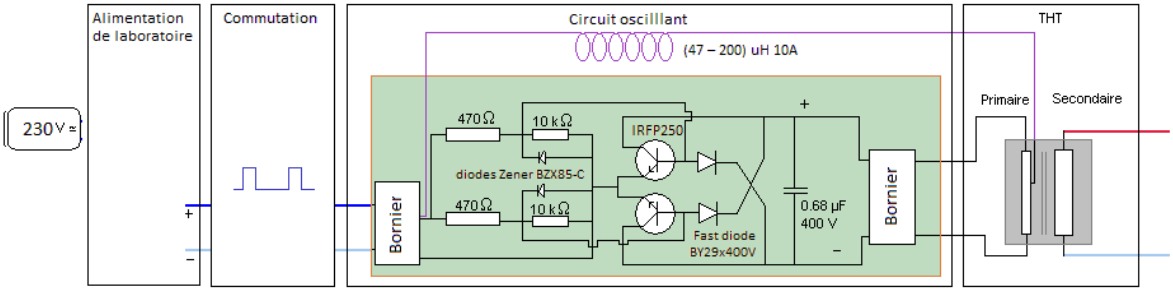

Figure 6.— Schéma du système actuel présent au LAPLACE (Toulouse)

B. Synthèse d'oxide de Cobalt et de Nickel dans un film d'oxide de Cobalt par décharge « Spark » dans l'eau déionisée

Les décharges dans les liquides étant maintenant mieux comprises, la synthèse de nanoparticules complexes à l'aide de décharge « Spark » dans les liquides peut être envisagée.

Dans ce chapitre, nous allons démontrer la possibilité de réaliser des complexes nanostructurés de nickel et de cobalt ainsi que leurs oxydes. Le choix de ces métaux est dû à leurs propriétés magnétiques qui leurs permettent des utilisations moderne dans l'imagerie médical ou des formes de stockage magnétique de données. La composition de ces structures sera analysée à l'aide d'un microscope électronique à transmission et par spectroscopies.

Dans cette publication, T. Merciris a réalisé la synthèse des particules à l'aide du montage expérimental précédemment étudiée dans le chapitre 3, la majorité de l'analyse ainsi que la rédaction initiale de l'article. Les co-auteurs ont participé à l'analyse des résultats et à la rédaction de l'article. Cette publication n'est pas complétement terminée.

Synthesis of nickel and cobalt oxides nanoparticles by pulsed underwater spark discharges

Thomas Merciris[1,3], Minsuk Cha[2], Flavien Valensi[3], and Ahmad Hamdan[1,*]

[1] Groupe de physique des plasmas, Département de Physique, Université de Montréal, C.P. 6128, Succ. Centre-ville, Montréal, Québec, H3C 3J7, Canada

[2] King Abdullah University of Science and Technology (KAUST), Physical Science and Engineering Division (PSE), Clean Combustion Research Center (CCRC), Thuwal 23955, Saudi Arabia

[3] Université de Toulouse, LAPLACE (Laboratoire Plasma et Conversion d'Energie), 118 route de Narbonne, F-31062 Toulouse Cedex 9, France

* Corresponding author: Email: ahmad.hamdan@umontreal.ca

Keywords: Spark discharge, plasma in-water, nanoparticles, cobalt, nickel

ABSTRACT

Synthesis of nanoparticles by efficient and ecological techniques is highly needed. Among various synthesis techniques, electrical discharges in liquids exhibit high potential to efficiently produce nanoparticles based on a controlled erosion of the electrodes. In this study, by sustaining spark discharges in water between Co-Co or Ni-Ni electrodes, Co or Ni (and their oxides) nanoparticles are synthesized. The use of Co-Ni or Ni-Co produced Co and Ni nanoparticles with a majority dominated by the nature of the anode pin. The produced nanoparticles are thoroughly characterized using transmission electron microscope. Although the synthesis of Co-Ni nanoalloys was not confirmed under the various investigated discharge conditions of pulse width (100 and 500 ns) and voltage amplitude (5 and 20 kV), core-shell nanoparticles are observed among the Ni-and Co nanoparticles. The as-synthesized nanoparticles are also characterized by UV-VIS absorption spectroscopy, and direct optical band gaps of the nanomaterials are determined.

1. INTRODUCTION

During the last few decades, the field of nanoscience is rapidly expanding, as it gets involved more and more in many areas of everyday life, such those of food science [1,2], data storage [3,4], medical [5,6], and many others [7,8]. One of the challenges in nanoscience field is the development of ecological, efficient, and selective synthesis processes.

There are multiple processes to produce nanomaterials that can be classified in two categories: top-down and bottom-up. Top-down approach implicates the breaking down of macroscopic material to nanoscale level (miniaturization), and they include mechanical ball milling, laser ablation, electrical discharge machining, etc. [9–14]. Meanwhile, the bottom-up approach relies on building nanomaterials from atoms and molecules, such as molecular self-assembly [15], atomic layer deposition [16], and other techniques [17–21].

Pulsed electrical spark discharges in dielectric liquids, which can be considered as top-down process, seem to fulfill the requirements of an ecological and efficient process [22,23]. Such a process is based on the application of pulsed high voltage between metal electrodes immersed in a dielectric liquid. The plasma created by a pulsed electrical discharge dissociates the liquid and locally heats the electrode surfaces, leading to the evaporation of matter in the plasma, as well as the ejection of melted droplets in liquid. The potential of such a synthesis technique is demonstrated over the last decade, and various nanomaterials were synthesized. Briefly, discharges in water produced oxides [24], while nanocomposite materials are produced when discharges are sustained in hydrocarbon liquids [13]. Metal nanomaterials are also produced when discharges are sustained in liquid nitrogen [25,26]. The unique plasma properties of spark discharges in liquids, such as high temperature, high pressure, and reduced lifetime [27] are the unique keys of the process as compared with other physical or chemical processes. Moreover,

novel phase of nanomaterial, synthesized by discharges in liquid nitrogen between lead electrodes, is recently reported [28,29].

Several reports have investigated the potential of in-liquid discharges to synthesize nanoalloys. For example, Kabbara et al. [30–32] have studied the capacity of synthesising several alloys, such as Cu-Ag, Cu-Zn, and Si-Sn, by sustaining discharges in liquid nitrogen. The reported results show that mixture of individual nanomaterials, particles of an element decorated by other, or nanoalloys with small quantity, are produced. Other recent study [33] that deals with discharges between Co and/or Ni electrodes in liquid nitrogen has showed the feasibility to synthesize Co-Ni nanoalloys, but such nanoparticles were found very scarce, as compared with others Ni and Co nanoparticles synthesized in the process.

In this study, we investigate the production of Co and Ni nanomaterials (and their oxides) by sustaining discharges in deionized water. This system of material is chosen because it has potential in various fields, such as catalysis [34–39], magnetic material [40–42], semi-conductor [43–45], and bio-sensor [46–50]. Four electrode configurations are tested: Ni-Ni, Co-Co, Ni (anode) - Co (cathode), and Co (anode) - Ni (cathode). Moreover, in each electrode configuration, several set of applied voltage and pulse width are tested. The produced nanoparticles are characterized by transmission electron microscope as well as by UV-Vis absorption spectroscopy.

2. EXPERIMENTAL SETUP AND CHARACTERIZATIONS

2.1. Discharge cell and conditions

A schematic of the experimental setup is shown in Figure 1. We used a nanosecond positive polarity pulsed power supply (NSP 120-20-P-500-TG-H, Eagle Harbor Technologies) to generate spark discharges between two electrodes immersed in deionized water. The power supply is

adjustable in magnitude and pulse width, and the tested values of magnitude were 5 and 20 kV, while the tested values of pulse width were 100 and 500 ns. The discharge is sustained during 10 minutes at a repetition rate of 50 Hz.

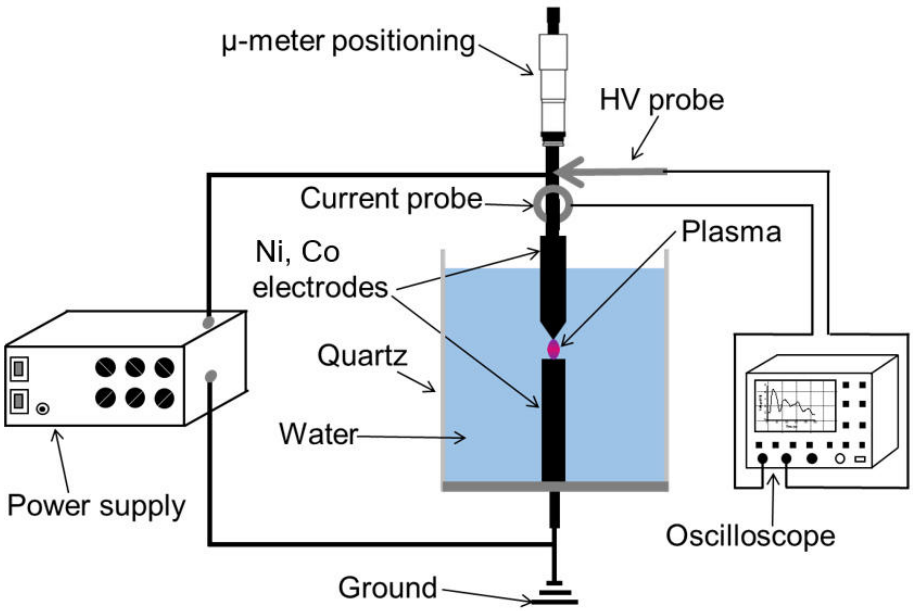

Figure 1 : Experimental setup

To produce Co and Ni nanostructures, four electrode configurations (anode-cathode) are tested: Ni-Ni, Co-Co, Ni-Co, and Co-Ni. Nickel electrodes have a length and diameter of 10 cm and 2 mm, respectively, and cobalt electrodes have a length and diameter of 5 cm and 2 mm, respectively; both electrodes have purity of 99.99% (from Goodfellow). In each configuration, the electrodes are vertically mounted on a micrometer positioning system and are distanced by ~50 µm. The anode is mechanically polished to have a curvature radius of ~10 µm, and the cathode (the ground) is also mechanically polished to have a plane surface. The discharges are conducted in a quartz cell with a length of 5 cm and an inner / outer diameter of 8 /10 mm. The cell is filled with 10 mL of deionized water (initial water conductivity ~3 µS/cm).

2.2. Nanostructures characterization

The synthesized nanostructures are analysed using TEM (Transmission Electron Microscopy) JEOL JEM-2100F operated at 200 kV. Samples of water solution in which the synthesized nanostructures are collected, sonicated for 5 minutes, and dropcasted in TEM Cu-grids endowed with a lacey C-film (from Electron Microscopy Science). Information on the nanostructures were derived via bright field TEM imaging, Electron Dispersive Spectroscopy (EDS), and Selected Area Electron Diffraction (SAED).

The SAED patterns were analyzed using a radial integration technique based on the use of an ImageJ plugin to generate the *Radial Profile Plot* [51] [24]. Briefly, the plugin integrates the pixel intensities of the diffraction pattern over concentric circles of different radii, defined from the center of the diffraction pattern, before dividing the resulting sum by the number of pixels forming each respective circle. This plot generates a spectrum equivalent to an XRD spectrum. To compare the measured distances with the theoretical ones, we used the NBS circular 539 [52] or the NBS monograph 25 [53]. Figure 2a and b respectively shows typical SAED pattern (acquired for nanostructures synthesized by discharges in Ni-Ni) and the generated spectrum.

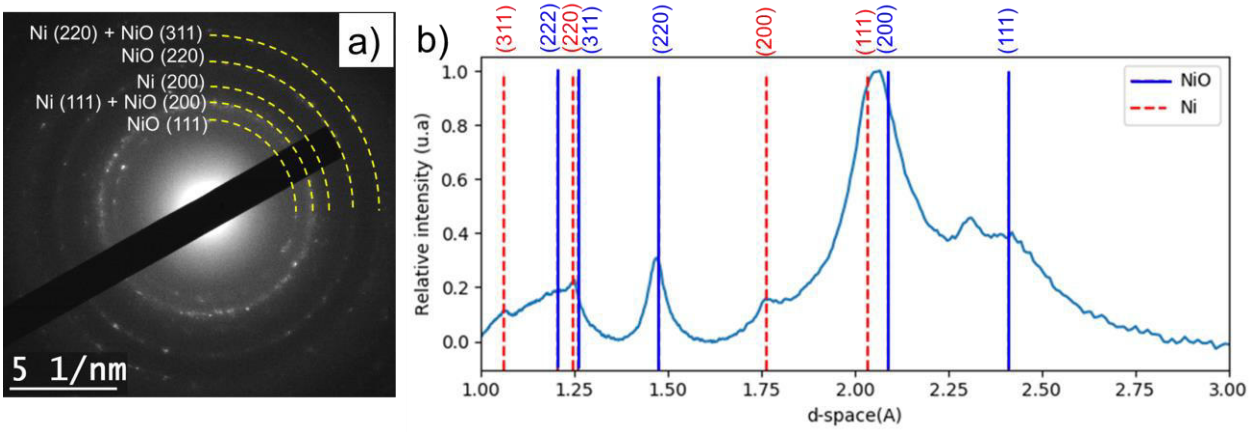

***Figure 2**: a) SAED pattern from TEM measurement from a Ni sample at 5kV_100ns and identification of the crystal from circular ring corresponding to the crystal D_Space. b) Relative intensity of the different crystals (Ni and NiO) from the NBS circular 539 volume 1. c) Radial profile of the experimental SAED pattern.*

As we will refer to interplanar distances along the manuscript, a list of the theoretical interplanar distances of the expected material (Ni, NiO, Co, CoO, and Co_3O_4) are shown in Table 1.

***Table 1**: theoretical interplanar distances of the expected material (Ni, NiO, Co, CoO, and Co_3O_4).*

Ni		NiO		Co		CoO		Co3O4	
d (Å)	**plan**	**d (Å)**	**plan**	**d (Å)**	**plan**	**d (Å)**	**plan**	**d (Å)**	**plan**
2.03	111	2.09	200	2.05	111	2.13	200	2.44	311
1.76	200	2.41	111	1.77	200	2.46	111	2.86	220
1.25	220	1.48	220	1.07	311	1.51	220	1.43	440
1.06	311	1.26	311	1.25	220	0.95	420	1.56	511
0.81	331	0.93	420	1.02	222	1.28	311	2.02	400
0.79	420	0.85	422			1.23	222	0.93	751

We also used UV-VIS absorption spectroscopy (Agilent, Cary 5000 UV-Vis-NIR) to identify the surface plasmon resonance of the as-synthesized particles in solution. We applied Tauc plot method on the UV-VIS spectra to evaluate the direct band gap energy of the synthesized material and its dependence on the various discharge conditions.

3. RESULTS

3.1. Ni-Ni configuration

Discharges between Ni electrodes in water are expected to produce Ni and NiO nanostructures. We explored the two-limit conditions of discharge conditions: high voltage / long pulse width (20 kV / 500 ns) and low voltage / short pulse width (5 kV / 100 ns). A low-resolution

TEM image of the synthesized Ni-based nanostructures are shown in Figure 3a. In this figure, one identifies three distributions of nanoparticles: the first one accounts the particles that have diameter between 50 and 150 nm (Figure 3a), the second one accounts the particles that have diameter between 10 and 50 nm (Figure 3d) , and the third one accounts the particles that have diameter < 10 nm (Figure 3e). A typical individual particle of the first distribution is shown in Figure 3b. Such a particle has a shell of a few nanometers and, furthermore, one identifies a sheet-like at the nanoparticle's surface (see the zoom in Figure 3b). Figure 3c shows another similar particle, on which we performed atomic-resolution scan as well as EDS analysis in two zones: close to the core (eds1) and close to the shell (eds2). The EDS spectra are dominated by Ni lines, although other lines (O, Cu, and C) are detected; Cu originates from the copper TEM grid, C originates from the carbon film on the grid, and O can originate from the grid as well as from the nanoparticle's shell that is expected to be oxidized. On the other hand, the measurement of the distances performed on atomic-resolution TEM shows that the interplanar distance is around 1.78 Å that corresponds to (200) reflection plan of Ni.

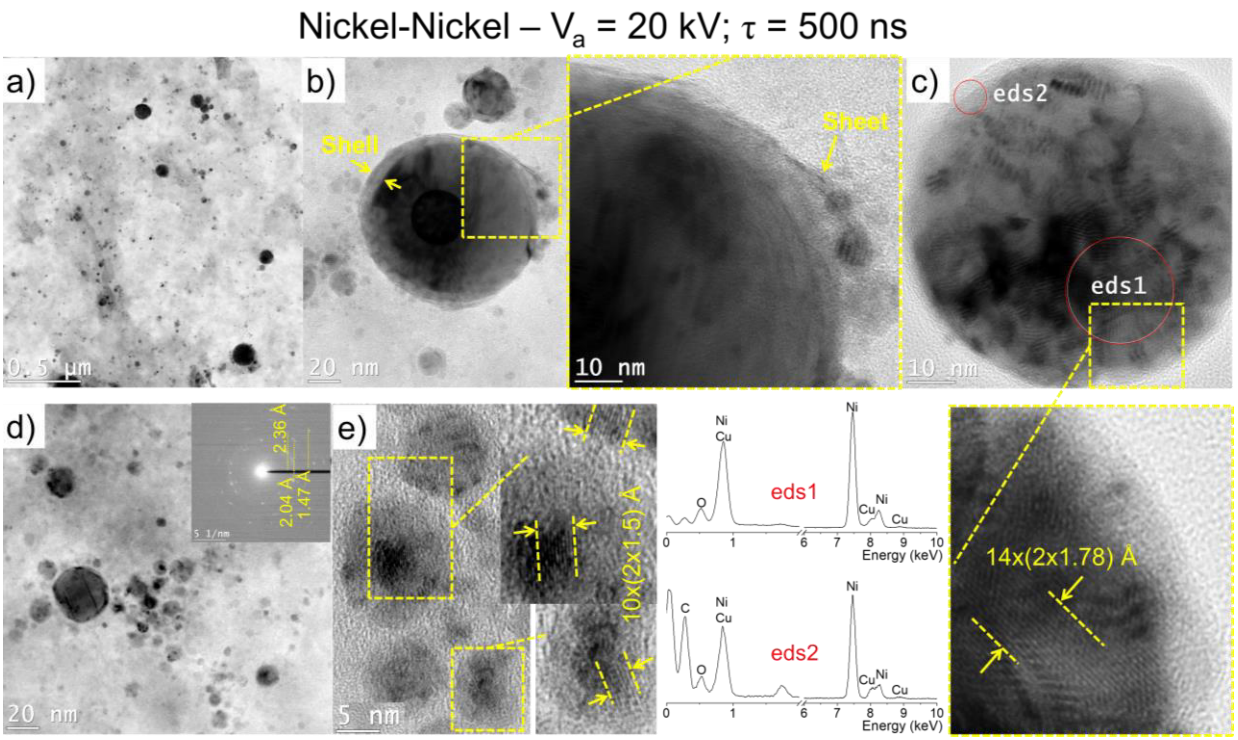

Figure 3 : Nickel and nickel oxide nanoparticles formed with 20kV-500 ns pulses.

As for the nanoparticles with diameter between 10 and 50 nm, shown in Figure 3d-e, the electron diffraction pattern (inset) as well as the measured interplanar distances converge towards NiO structure.

In the case of the 5 kV / 100 ns discharge, although the same distributions (mentioned previously) are identified, the overall synthesis yield is reduced, which is expected. A typical particle of the larger distribution is shown in Figure 4a. In the same figure, one can also identifies a square-shape nanoparticle that has a length of about 60 nm. In Figure 4b, one shows an object that seems to be an agglomeration of ultrasmall nanoparticles. In Figure 4c, we show a sample of the smaller nanoparticles. The insets of this figure show zooms on particles that have diameters about 10 nm: particle 1 seems not to have a shell, but tiny particles around; particle 2 is a particle with a square shape, and the core-shell appearance seems to be a superimposition of two particles;

particle 3 has a typical core-shell structure. As compared with the case of 20 kV / 500 ns, one remarks that the probability to produce nanoparticles that have diameter < 10 nm, regarding the others, is relatively high at low voltage and short pulse width. This may provide a hint on the control of size distribution using the current discharge technique.

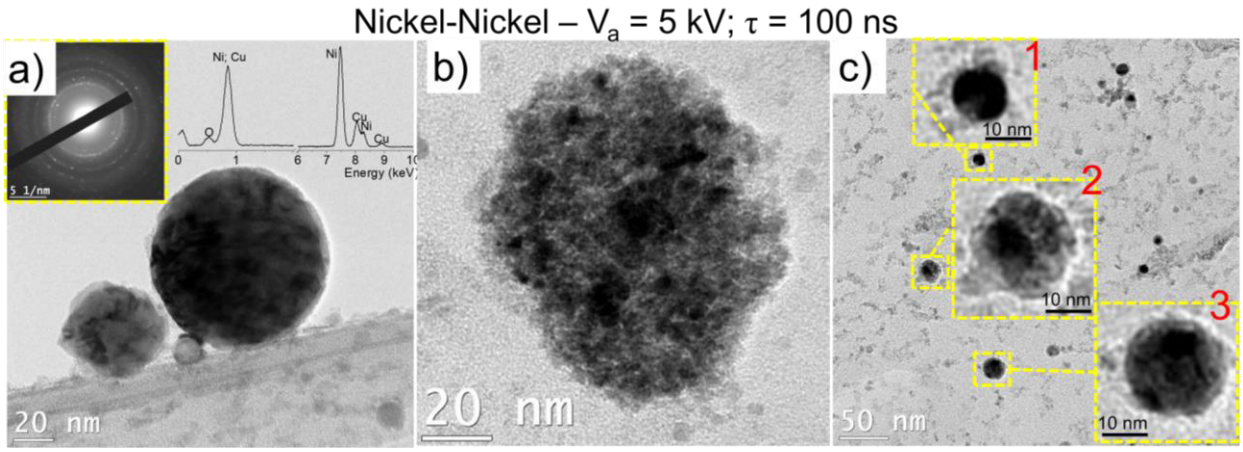

Figure 4 : Nickel and nickel oxide nanoparticles formed with 5kV-100 ns pulses

SAED patterns are further processed to produce a spectrum using the method describes in Section 2.2. Overall, the spectra of SAED pattern performed on large areas, such as Figure 3a, are very well fitted using the Ni and NiO lines. However, the particles that exhibit a film-like, such as Figure 3b, show an additional peak (Figure 5) at ~2.5 Å that can be attributed to nickel hydroxide α-$Ni(OH)_2$ [39,54,55]. Under our discharge conditions, it is not surprising to synthesize such nickel hydroxide particles, because discharge in water effectively produce oxidative species including OH, O, H, and H_2O_2.

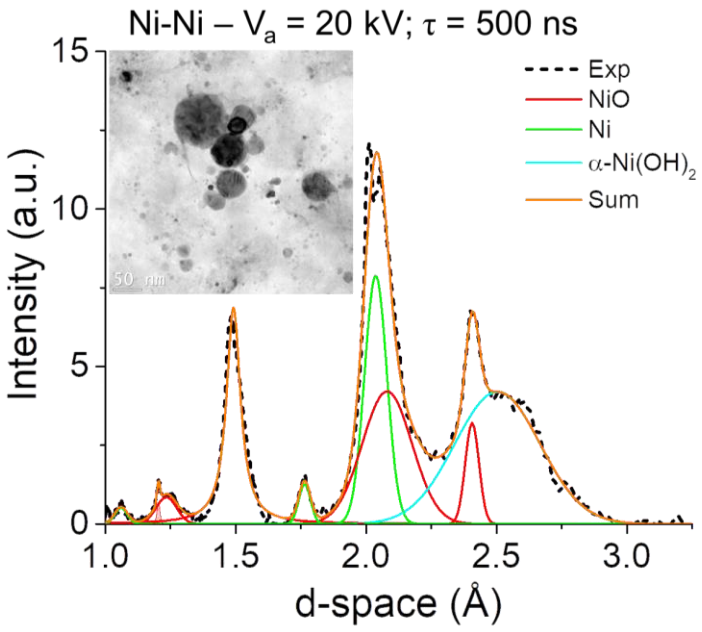

Figure 5: SAED pattern of the nickel sample (20kV / 500ns)

3.2. Co-Co configuration

In the case of Co-Co discharges under 20 kV / 500 ns, one identifies three particles distributions (50-150 nm, 10-50 nm, and < 5 nm), similar to the case of Ni-Ni discharges. A low-resolution TEM image in Figure 6a indicates that the smallest particles are dominating, and the EDS analysis performed on the same area shows Co and O, among the other elements coming from the grid. Similar EDS spectrum is obtained after local analysis on a particle of 150 nm diameter (Figure 6b). High resolution imaging of such a particle shows that it exhibits on its right-bottom a shell of a few nanometers, while at the top-left of the particle is surrounded by the smaller particles. Such kind of nanoparticles decorating a relatively larger particle are already observed and referred as gauzes [56] [33]. The non-homogeneity of the gauze (right-bottom vs. top-left) can be related to the dynamics of the ejected particles in solution, while the pressure at the front is relatively higher that that at the rear. High resolution TEM performed on the particle's core leads to an interplanar distance of 1.05 Å which represent the plan (222) of Co, while the interplanar

distance measured on the particle peripheral is 1.56 Å, which may be attributed to the (511) plan of Co_3O_4.

Figure 6e shows a typical particle of a diameter of 40 nm that appears to have a core-shell structure. High-resolution imaging on this particle shows that both the core and the shell have close interplanar distances (1.31 and 1.32 Å) which may be related to (220) plan of Co and (201) plan of $Co(OH)_2$ [57]. Finally, Figure 6g shows the typical very small nanoparticles that are Co_3O_4 as the SAED shows (see below).

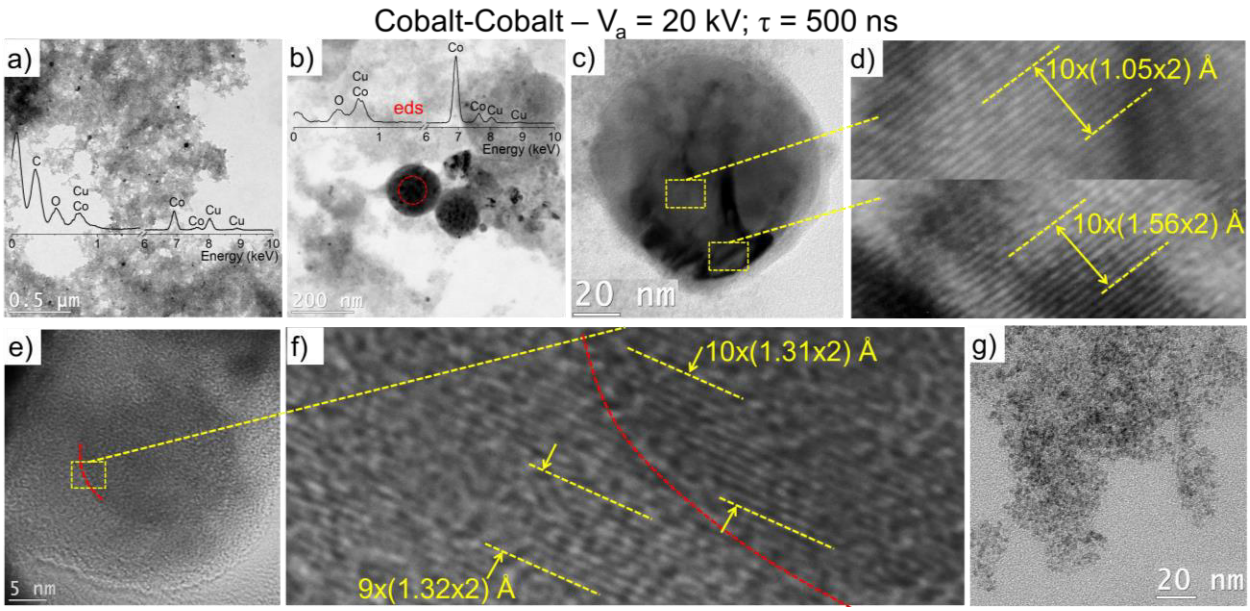

Figure 6 : Cobalt and cobalt oxide nanoparticles formed with 20kV-500 ns pulses

Co-based nanoparticles synthesized at 5 kV / 100 ns are shown in Figure 7. Nanoparticle distributions similar to those reported in the case of 20 kV / 500 ns are identified, but because the synthesis yield is smaller, the very small particles appear as porous film (Figure 7b-c). Unlike the previous conditions, the larger particle (Figure 7b) does not exhibit a shell. This may be related to

the dynamic (e.g., lower speed) of the ejected particle. However, the particle with diameter of 10 nm (Figure 7d) show an important shell of about 5 nm that is probably composed of $Co(OH)_2$.

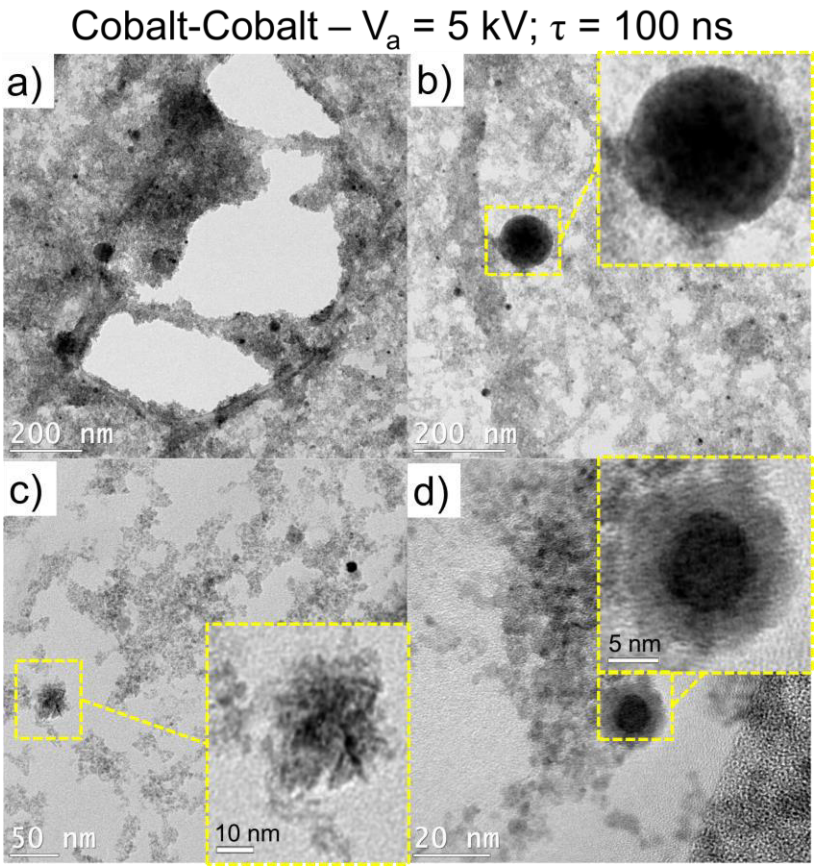

Figure 7 : Cobalt and cobalt oxide nanoparticles created formed with 5kV-100 ns pulses

Similar to the case of Ni nanoparticles, the spectra of SAED pattern performed on large areas, such as Figure 7a, are very well fitted using the Co and Co_3O_4 lines. The presence of a $Co(OH)_2$ (001) reflection plan at 4.7Å is also confirmed [58].

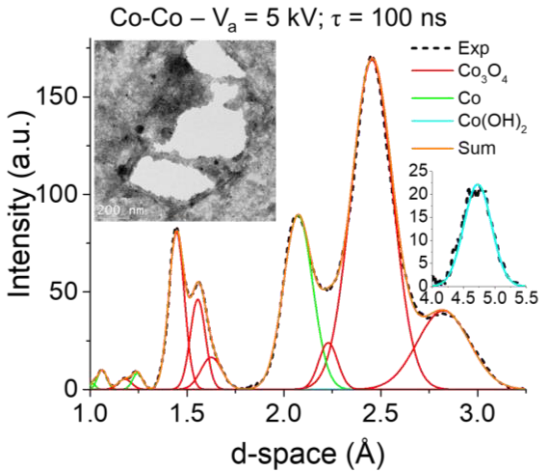

Figure 8 : SAED pattern of the cobalt sample (5kV_100ns)

3.3. Ni (anode) -Co (cathode) configuration

The use of two different electrodes, Ni anode and Co cathode, is to investigate the feasibility of synthesizing Ni-Co nanoalloys. In Figure 9 we show various nanoparticles synthesized at 20 kV / 500 ns. Global EDS analysis (Figure 9a) shows signatures of Co and Ni, among others. This confirm that erosion of both electrodes has occurred. Other EDS analysis is locally performed on various particles, and the results are shown in Figures 9b-c. The EDS analysis was performed on four individual particles that have diameter between 50 and 100 nm, and the corresponding spectra are shown in Figure 9c. Spectrum of particle #1 shows Ni but not Co. Particles #2, #3, and #4 show an intense Ni peak and low intensity of Co peak. Analysis on zone #5, where particles have a diameter < 10 nm, shows great Co peak and small Ni peak. From these analyses, one deduces that, under this condition of 20 kV / 500ns, the particles that have a diameter < 10 nm are made of cobalt oxide, while the particles that have a diameter > 10 nm are made of nickel oxide. Also, it was possible to identify particles with diameter > 10 nm that are made of Co, but they are very scarce.

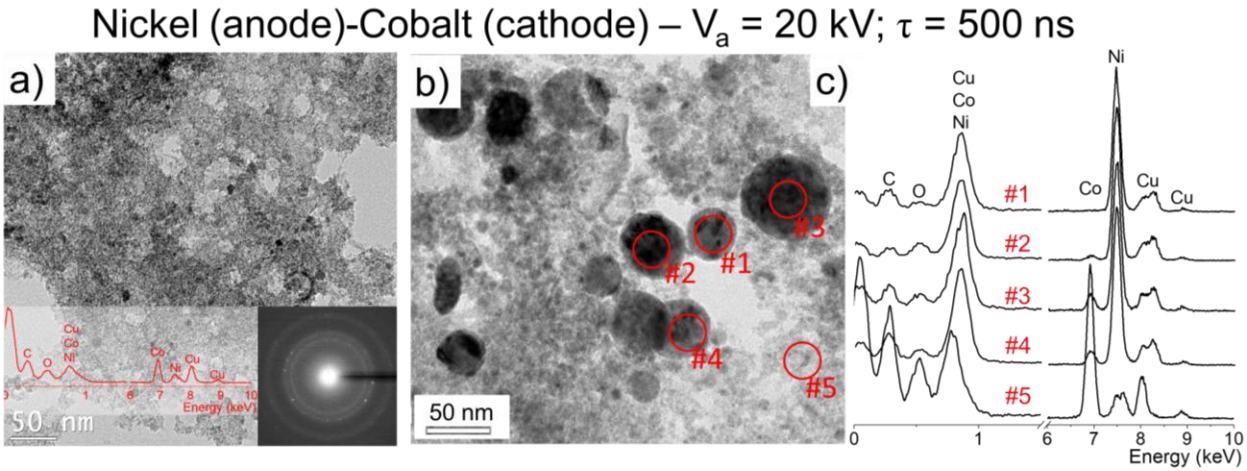

Figure 9 : Nanoparticles formed by nickel (anode) and cobalt (cathode) electrodes with 20kv_500ns discharge

Figure 10 shows various nanoparticles synthesized at 5 kV / 100 ns. Similar to the previous case, the EDS analysis on a large area (Figure 10a, area #1) shows signatures of both elements Co and Ni, among others. Particles #2 and #3, that has a diameter between 50 and 100 nm, are mainly composed of Ni and Co, respectively. It is worth noting that despite the statistical analysis of the particles, it was possible to find more Co particles, unlike the previous case of 20 kV / 500 ns.

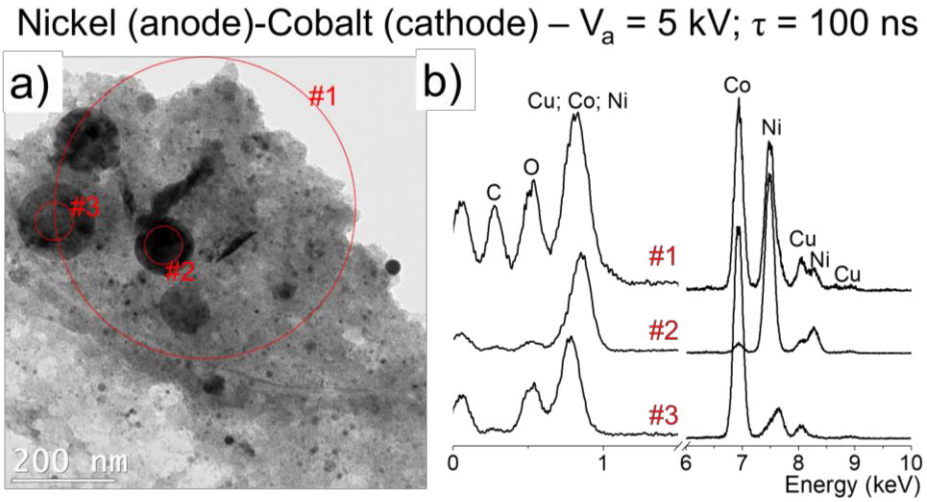

Figure 10 : Nanoparticles formed by nickel (anode) and cobalt (cathode) electrodes with 5kv_100ns discharge

Further discharges at high voltage / short pulse width (i.e., 20 kV / 100 ns) are conducted, and the results are summarized in Figure 11. The EDS analysis on area #1, that is dominated by particles that have a diameter < 10 nm, shows that these nanoparticles are composed of Ni and Co oxides. The particles that have diameter of 50-100 nm are made of Ni, as the results observed in the case of 20 kV / 500 ns. At this stage, it seems that at higher voltage the larger particles are made of nickel oxide while the smallest particles are made of cobalt and nickel oxides, although few large Co nanoparticles can be found with very small quantity.

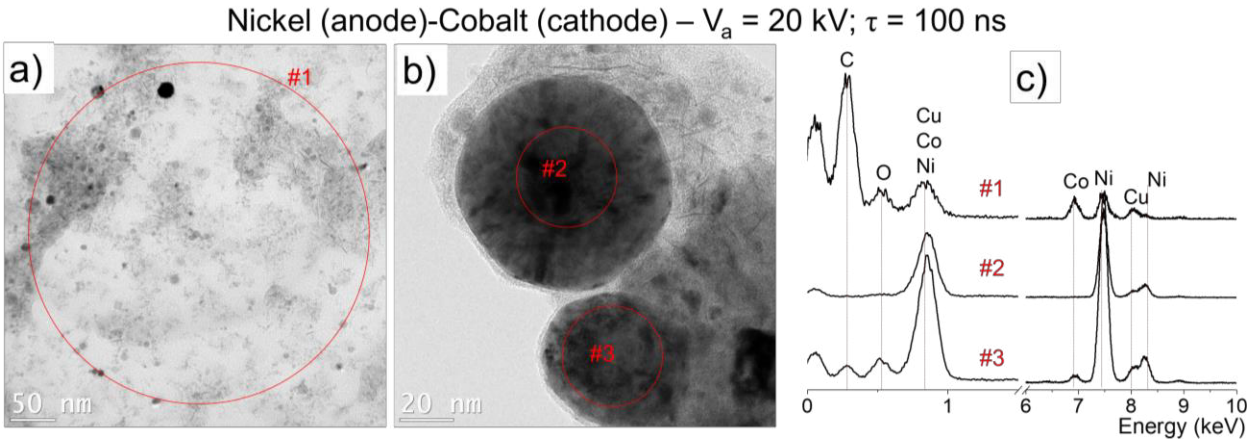

Figure 11 : Nanoparticles formed by a cobalt (anode) nickel (cathode) with 20kv_500ns discharge.

Because the erosion rate of anode and cathode can be different, we changed the polarity of each electrode regarding the previous conditions, i.e., cobalt-anode and nickel-cathode, and sustained discharges at 5 kV / 100 ns. The nanoparticles synthesized under this condition are shown in Figure 12. An EDS analysis of a large area of nanoparticles shows the presence of both Ni and Co peaks (Figure 12a). It is worth noting that the probability to produce nanoparticles that have diameter > 20 nm is strongly reduced (Figure 12b). EDS analysis on individual particles shows three types of compositions: only nickel oxide, only cobalt oxide, and core-shell like nanoparticle, as the one shown in Figure 12c.

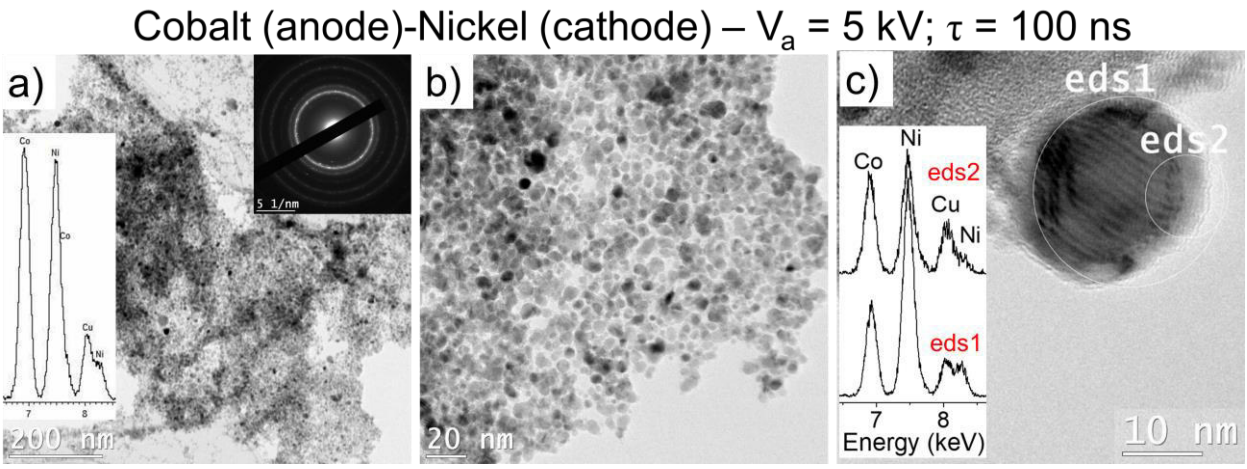

Figure 12 : Nanoparticles formed by a cobalt (anode) nickel (cathode) with 5kv_100ns discharge.

From the above TEM observations, one concludes that spark discharges between Ni and/or Co electrodes in water produce three distributions of nanoparticles. The first distribution is characterized by particles diameter larger than 50 nm composed of nickel or cobalt, depending on the nature of the electrodes, with an oxide shell of few nanometers. The shell was found inhomogeneous around the particles, because it probably growths during particle ejection in water. The second distribution counts the particles with size typically between 10 and 50 nm that are composed of nickel oxide or cobalt oxide depending on the electrode's configuration. It seems that surface of some particles from this distribution exhibit at their surfaces $Co(OH)_2$ or $Ni(OH)_2$ if Co or Ni electrodes were used, respectively. The third distribution is composed of nanoparticles that have a diameter smaller than 10nm and they are composed of nickel or cobalt oxides. In the case of Ni-Co or Co-Ni electrodes, nanoalloys were not found, but rather a core-shell structure in addition to individual Ni and Co nanoparticles.

4. UV-VISIBLE ABSORPTION SPECTROSCOPY

UV-Visible absorption spectroscopy was performed on the as-synthesized nanoparticles in solution. The advantage of such a characterization technique is about its statistical approach on a large number of particles present in solution, unlike TEM, which is rather a local analysis. The

absorbance curves of nanoparticles synthesized in the case of Ni-Ni discharges at a pulse width of 500 ns and for various voltages are shown in Figure 13a. The absorbance curves are similar to those reported in other studies [20,59,60]. The trend of absorbance values acquired under various conditions of applied voltage are expected, as the production rate is higher at high voltage. However, the normalized spectra (shown in the inset of Figure 13a) do not present significant differences, indicating thus that the synthesized nanoparticles under various applied voltages are similar. This fact is further confirmed by reporting the direct optical band gap energy by performing the Tauc plot, as shown in Figure 13b. The measured energy gap is ~4 eV, which also agrees with the values reported elsewhere [59][60].

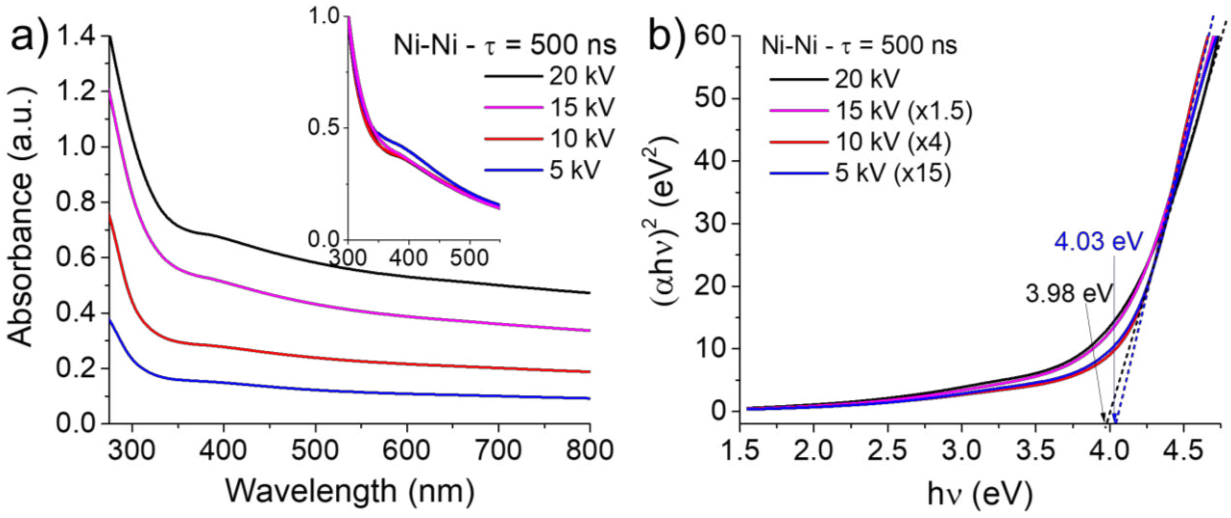

Figure 13 : UV-visible spectrum and Tauc plot of Ni and NiO nanoparticles (Pulse width 500ns)

Similarly, the UV-Visible absorbance spectra of nanoparticles synthesized in the case of Co-Co discharges at a pulse width of 500 ns and for various voltages are shown in Figure 14a; the absorbance curves are very similar to those reported for Co_3O_4 nanoparticles [61,62]. Similar to the pervious case of Ni-Ni discharges, the production rate of Co-based nanoparticles increases with the applied voltage (increase of the absorbance value), but there is no significant variation in the

peak shape and position as shown by the normalized spectra (inset of Figure 14a). The application of Tauc plot method on the absorbance spectra reveals two direct optical band gaps at ~2.6 eV and 4 eV, regardless the amplitude of the applied voltage. These two gaps are also already reported in other studies on Co_3O_4 [63] and their presence is attributed to charge transfer in Co_3O_4. It was reported that the first transition (2.6 eV) is due to charge transfer between $Co^{3+}(\pi^*t_2) \rightarrow Co^{2+}(\sigma^*t_2)$, which is attributed to the internal oxidation-reduction process inside the unit cell. Meanwhile, the second transition (4 eV) is due to charge transfer involved between $O_2^-(\pi^*\Gamma) \rightarrow Co^{2+}(\sigma^*t_2)$, which is the real band gap of Co_3O_4 that corresponds to interband transitions [61][64].

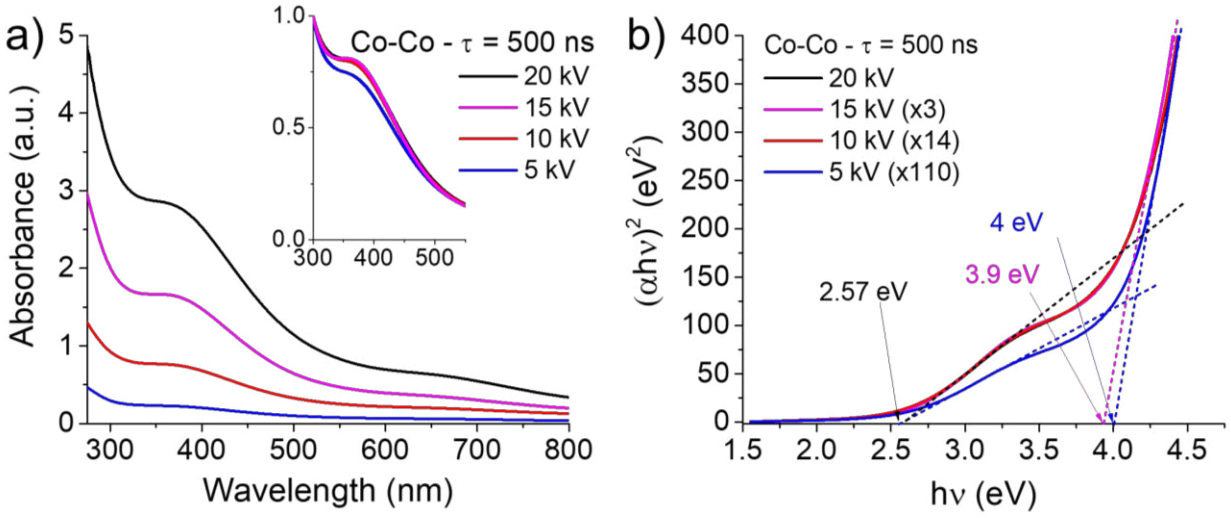

Figure 14 : UV-visible spectrum and Tauc plot of Co and Co_3O_4 nanoparticles (Pulse width 500ns) x

On the other hand, the band gap energy of the nanoparticles ($E_{g,nano}$) depends on the bandgap energy of the bulk material ($E_{g,bulk}$) and on the nanoparticles' diameter (D) through Brus's equation [65]:

$$E_{g,nano} = E_{g,bulk} + \frac{\mathrm{h}^2}{2\mathrm{D}^2 m_0}\left(\frac{1}{m_e^*/m_0} + \frac{1}{m_h^*/m_0}\right) - \frac{1.8e^2}{2\pi\varepsilon_0\varepsilon_r D} \qquad (1)$$

where m_0 = 9.109×10^{-31} kg is the electron mass, and m_e^* and m_h^* are the electron and hole effective masses, respectively. h is Planck's constant, and e is the electron charge.

In the case of NiO (respectively Co_3O_4), $E_{g,bulk}$ = 3.8 eV [66] (respectively 1.8 eV and 3.35 eV [67]), m_h^*/m_0 = 0.8 [68] (respectively 0.4 [69]), $m_e^*/m_0 = 0.8$ [70] (respectively $m_e^*/m_0 = 0.2$ [61]), and relative permittivity ε_r = 11.5 [71] (respectively 12.6 [61]). Considering the values of $E_{g,nano}$ found from Tauc plot, the main unknown in equation 1 is the particle's diameter. We found this latter being ~3.4 nm for particles synthesized in Ni-Ni discharge and 3.5 or 3.8 nm for particles synthesized in Co-Co discharges, if we consider the two band of Co_3O_4, respectively, which is in great agreement with the size of the smallest particles observed in TEM.

We also performed the UV-Visible absorption on the nanoparticles synthesized using different electrodes, and the absorbance curves acquired in the case of Ni (anode)-Co (cathode) are shown in Figure 15a for different voltages. In a first approximation, the curves behavior is close to that of nanoparticles synthesized in Ni-Ni discharges. However, the Tauc plots performed on these curves, as shown in Figure 15b, reveal two direct optical band gaps, at 2.6 and 4 eV. The presence of these two bands indicate that Co_3O_4 nanoparticles are present together with NiO nanoparticles. The insignificant dependence of the energy bands on the discharge voltage indicate that the nature of nanoparticles does not appreciably change with the discharge condition.

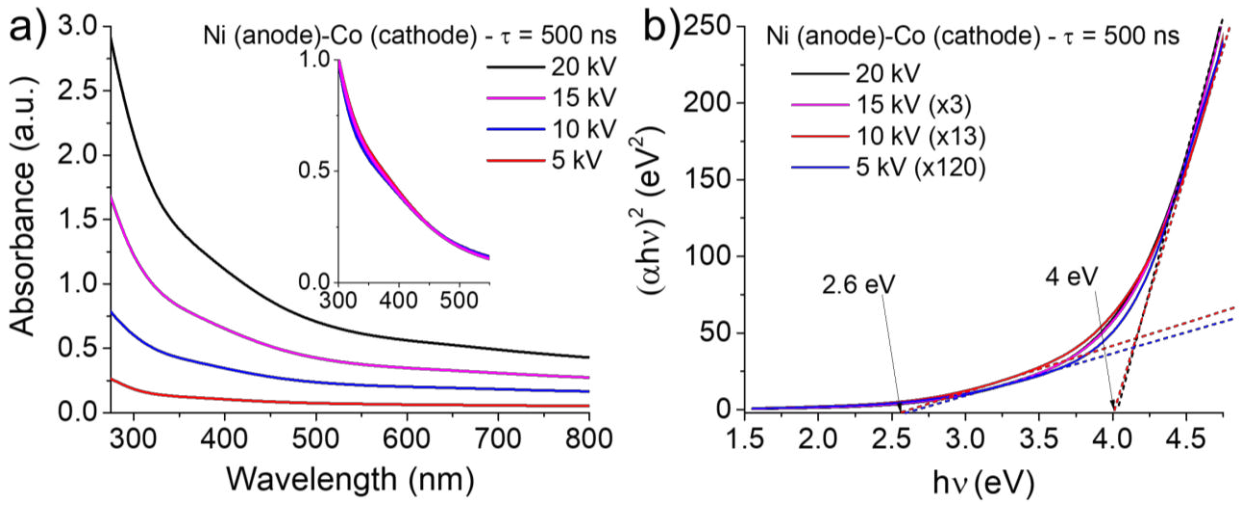

Figure 15 : UV-visible spectrum and Tauc plot of Ni /Co nanoparticles inside the cobalt oxide layer (Pulse width 500ns) (Anode: Nickel / Cathode: Cobalt)

In an opposite electrode configuration, i.e., Co (anode)-Ni (cathode), the absorbance spectra, shown in Figure 16a, reveal a behavior different from the previous configuration, where the spectra are closer to those obtained in Co-Co configurations. Tauc plots, shown in Figure 16b, also reveals the presence of the two optical bands those at 2.6 and 4 eV.

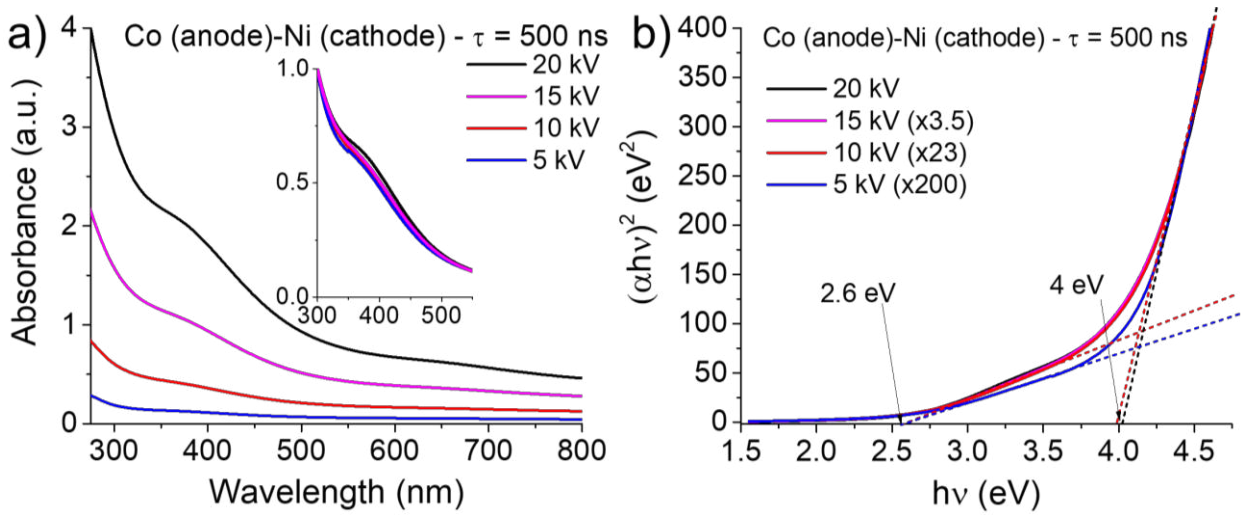

Figure 16 : UV-visible spectrum and Tauc plot of Ni /Co nanoparticles inside the cobalt oxide layer (Pulse width 500ns) (Anode: Cobalt / Cathode: Nickel)

Because that the UV-Vis absorption spectroscopy is a global analysis, unlike TEM which is local, the insignificant dependence of the applied voltage on the general behavior of the absorbance spectra and the band gap energies, indicate that the produced nanoparticles are very similar, i.e., the process is highly reproducible and selective to produce nanoparticles. This is true for the case of similar electrodes, Ni-Ni or Co-Co, as well as for the case of different electrodes, Ni-Co and Co-Ni. However, the fact that the electrodes configuration is pin-to-plate may explain the behavior of the absorbance spectra that, in the case of Co-Ni, is close to that of Co-Co, and that, in the case of Ni-Co, is close to that of Ni-Ni. In this context, we used the absorbance spectra acquired in Co-Co and Ni-Ni to rebuild those obtained in Ni-Co and Co-Ni, under similar experimental conditions of applied voltage and pulse width, and the results are depicted in Figure 17. In the case of Co-Ni (at 5 kV/100 ns), the reproduction of the absorbance spectrum was optimum for 39% of Co-Co and 28% of Ni-Ni spectra. Meanwhile, in the case of Ni-Co (at 5 kV/100 ns), the reproduction of the absorbance spectrum was optimum for 46% of Ni-Ni and 19% of Co-Co. Although the reproduction is not perfect, it provides several information: i) in the case

of Co-Ni, the content of Co-Co is relatively higher than Ni-Ni; ii) in the case of Ni-Co, the content of Ni-Ni is relatively higher than Co-Co; iii) the reproduction of the absorbance spectra is not 100% achieved, which means that particles others than Ni and Co may be present, such as core-shell structure or nanoalloys; these latter are not found among the particles analyzed in TEM, however, in a discharge conditions close to ours [71], nanoalloys are clearly observed.

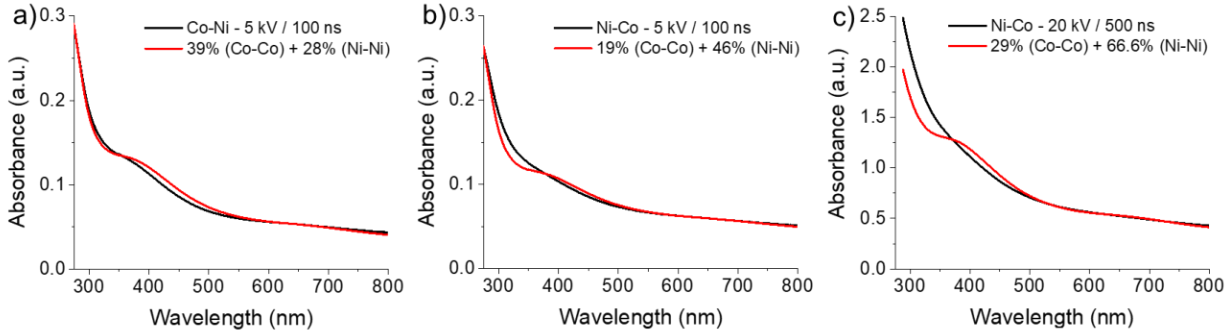

Figure 17 : Reconstitution of the alloy absorbance with the pure metal absorbance in the same experimental conditions

7. CONCLUSION

In this study, by sustaining discharges in water between different configuration of Co and Ni electrodes, Co or Ni particles (and their oxides) are synthesized. The electrode configuration has an impact on the concentration of the nanoparticles, as the use of Co-Ni or Ni-Co produced Co and Ni nanoparticles (and their oxides) with a majority dominated by the nature of the anode pin. However, no measurable evidence of the influence of the discharge parameters on the characteristics of the synthesized nanoparticles.

The produced nanoparticles are thoroughly characterized using TEM and SAED. Although the synthesis of Co-Ni nanoalloys was not confirmed under the various investigated discharge conditions of pulse widths (100 and 500 ns) and voltage amplitude (5 and 20 kV), core-shell

nanoparticles are observed among the Ni and Co nanoparticles. The as-synthesized nanoparticles are also characterized by UV-VIS absorption spectroscopy, and direct optical band gaps of the nanomaterials are determined. The found band gap energies were used to confirm the average size of the dominated nanoparticles, which is found ~ 3-4 nm.

ACKNOWLEDGMENTS

This publication is based upon work supported by the King Abdullah University of Science and Technology (KAUST) Office of Sponsored Research (OSR) under Award No. OSR-2019-CPF-1975.33

REFERENCE

[1] He X and Hwang H-M 2016 Nanotechnology in food science: Functionality, applicability, and safety assessment *Journal of Food and Drug Analysis* **24** 671–81

[2] Singh T, Shukla S, Kumar P, Wahla V, Bajpai V K and Rather I A 2017 Application of Nanotechnology in Food Science: Perception and Overview *Front. Microbiol.* **8**

[3] Gu M, Zhang Q and Lamon S 2016 Nanomaterials for optical data storage *Nature Reviews Materials* **1**

[4] Mansuripur M 2011 The role of nanotechnology in data storage devices and systems *Nonlinear Optics* Joint International Symposium on Optical Memory and Optical Data Storage (Kauai, Hawaii: OSA) p OMA2

[5] Nasimi P and Haidari M 2013 Medical Use of Nanoparticles: Drug Delivery and Diagnosis Diseases *International Journal of Green Nanotechnology* **1** 1943089213506978

[6] Murthy S K 2007 Nanoparticles in modern medicine: State of the art and future challenges *Int J Nanomedicine* **2** 129–41

[7] Beek W J E, Wienk M M and Janssen R A J 2004 Efficient Hybrid Solar Cells from Zinc Oxide Nanoparticles and a Conjugated Polymer *Advanced Materials* **16** 1009–13

[8] Beydoun D, Amal R, Low G and McEvoy S Role of Nanoparticles in Photocatalysis 20

[9] Oseguera-Galindo D, Machorro-Mejia R, Bogdanchikova N and Mota-Morales J 2016 Silver nanoparticles synthesized by laser ablation confined in urea choline chloride deep-eutectic solvent - ScienceDirect

[10] Sylvestre J-P, Poulin S, Kabashin A V, Sacher E, Meunier M and Luong J H T Surface Chemistry of Gold Nanoparticles Produced by Laser Ablation in Aqueous Media 6

[11] Popov A A, Tselikov G, Dumas N, Berard C, Metwally K, Jones N, Al-Kattan A, Larrat B, Braguer D, Mensah S, Da Silva A, Estève M-A and Kabashin A V 2019 Laser- synthesized TiN nanoparticles as promising plasmonic alternative for biomedical applications *Scientific Reports* **9** 1–11

[12] Hamdan A, Abdul Halim R, Anjum D and Cha M S 2017 Synthesis of SiOC:H nanoparticles by electrical discharge in hexamethyldisilazane and water *Plasma Processes and Polymers* **14** 1700089

[13] Hamdan A, Noël C, Ghanbaja J, Migot-Choux S and Belmonte T 2013 Synthesis of platinum embedded in amorphous carbon by micro-gap discharge in heptane *Materials Chemistry and Physics* **142** 199–206

[14] Hamdan A and Cha M S 2018 Carbon-based nanomaterial synthesis using nanosecond electrical discharges in immiscible layered liquids: n-heptane and water *Journal of Physics D: Applied Physics* **51** 244003

[15] Mishra P K and Ekielski A 2019 The Self-Assembly of Lignin and Its Application in Nanoparticle Synthesis: A Short Review *Nanomaterials* **9** 243

[16] Eswar N K R, Singh S A and Heo J 2019 Atomic layer deposited photocatalysts: comprehensive review on viable fabrication routes and reactor design approaches for photo-mediated redox reactions *Journal of Materials Chemistry A* **7** 17703–34

[17] Salavati-Niasari M and Khansari A 2014 Synthesis and characterization of Co3O4 nanoparticles by a simple method *Comptes Rendus Chimie* **17** 352–8

[18] Wadekar K F, Nemade K R and Waghuley S A 2017 Chemical synthesis of cobalt oxide (Co3O4) nanoparticles using Co- precipitation method **7** 3

[19] Vijaya Kumar P, Jafar Ahamed A and Karthikeyan M 2019 Synthesis and characterization of NiO nanoparticles by chemical as well as green routes and their comparisons with respect to cytotoxic effect and toxicity studies in microbial and MCF-7 cancer cell models *SN Appl. Sci.* **1** 1083

[20] Rahdar A, Aliahmad M and Azizi Y 2015 NiO Nanoparticles: Synthesis and Characterization 7

[21] El-Kemary M, Nagy N and El-Mehasseb I 2013 Nickel oxide nanoparticles: Synthesis and spectral studies of interactions with glucose *Materials Science in Semiconductor Processing* **16** 1747–52

[22] Pfeiffer T V, Feng J and Schmidt-Ott A 2014 New developments in spark production of nanoparticles *Advanced Powder Technology* **25** 56–70

[23] Tabrizi N S, Ullmann M, Vons V A, Lafont U and Schmidt-Ott A 2008 Generation of nanoparticles by spark discharge *J Nanopart Res* **11** 315

[24] Glad X, Profili J, Cha M S and Hamdan A 2020 Synthesis of copper and copper oxide nanomaterials by electrical discharges in water with various electrical conductivities *Journal of Applied Physics* **127** 023302

[25] Kabbara H, Ghanbaja J, Noël C and Belmonte T 2017 Synthesis of Cu@ZnO core–shell nanoparticles by spark discharges in liquid nitrogen *Nano-Structures & Nano-Objects* **10** 22–9

[26] Trad M, Nominé A, Tarasenka N, Ghanbaja J, Noël C, Tabbal M and Belmonte T 2019 Synthesis of Ag and Cd nanoparticles by nanosecond-pulsed discharge in liquid nitrogen *Frontiers of Chemical Science and Engineering* **13** 360–8

[27] Belmonte T, Hamdan A, Kosior F, Noël C and Henrion G 2014 Interaction of discharges with electrode surfaces in dielectric liquids: application to nanoparticle synthesis *J. Phys. D: Appl. Phys.* **47** 224016

[28] Hamdan A, Kabbara H, Noël C, Ghanbaja J, Redjaimia A and Belmonte T 2018 Synthesis of two-dimensional lead sheets by spark discharge in liquid nitrogen *Particuology* **40** 152–9

[29] Kabbara H, Ghanbaja J, Redjaïmia A and Belmonte T 2019 Crystal structure, morphology and formation mechanism of a novel polymorph of lead dioxide, γ-PbO2 *J Appl Cryst* **52** 304–11

[30] Kabbara H, Ghanbaja J, Noël C and Belmonte T 2018 Nano-objects synthesized from Cu, Ag and Cu28Ag72 electrodes by submerged discharges in liquid nitrogen *Materials Chemistry and Physics* **217** 371–8

[31] Kabbara H, Ghanbaja J, Noël C and Belmonte T 2018 Synthesis of copper and zinc nanostructures by discharges in liquid nitrogen *Materials Chemistry and Physics* **207** 350–8

[32] Kabbara H, Noël C, Ghanbaja J, Hussein K, Mariotti D, Švrček V and Belmonte T 2015 Synthesis of nanocrystals by discharges in liquid nitrogen from Si–Sn sintered electrode *Sci Rep* **5**

[33] Trad M, Nominé A, Noël C, Ghanbaja J, Tabbal M and Belmonte T Evidence of alloy formation in CoNi nanoparticles synthesized by nanosecond-pulsed discharges in liquid nitrogen *Plasma Processes and Polymers* **n/a** e1900255

[34] Mate V R, Shirai M and Rode C V 2013 Heterogeneous Co3O4 catalyst for selective oxidation of aqueous veratryl alcohol using molecular oxygen *Catalysis Communications* **33** 66–9

[35] Saputra E, Duan X, Armedi Pinem J, Bahri S and Wang S 2017 Shape-controlled Co3O4 catalysts for advanced oxidation of phenolic contaminants in aqueous solutions *Separation and Purification Technology* **186** 213–7

[36] Zhou Y, Dong C-K, Han L, Yang J and Du X-W 2016 Top-Down Preparation of Active Cobalt Oxide Catalyst *ACS Catal.* **6** 6699–703

[37] Liu F, Sang Y, Ma H, Li Z and Gao Z 2017 Nickel oxide as an effective catalyst for catalytic combustion of methane *Journal of Natural Gas Science and Engineering* **41** 1–6

[38] Singh H, Yadav R, Rajput P, Bhattacharyya D, Jha S N and Sinha A K 2019 Magnetically Recoverable Ni/NiO Catalyst for Hydrogenation of Cashew Nut Shell Oil to Value-Added Products *Energy Fuels* **33** 5332–42

[39] Adekunle A S, Oyekunle J A O, Oluwafemi O S, Joshua A O, Makinde O, Ogunfowokan A O, Eleruja M A and Ebenso E E 2014 Comparative Catalytic Properties of Ni(OH)2 and NiO Nanoparticles Towards the Degradation of Nitrite (NO2-) and Nitric Oxide (NO) *Int. J. Electrochem. Sci.* **9** 14

[40] Tadic M, Nikolic D, Panjan M and Blake G R 2015 Magnetic properties of NiO (nickel oxide) nanoparticles: Blocking temperature and Neel temperature *Journal of Alloys and Compounds* **647** 1061–8

[41] Seidov Z, Açıkgöz M, Kazan S and Mikailzade F 2016 Magnetic properties of Co3O4 polycrystal powder *Ceramics International* **42** 12928–31

[42] Ichiyanagi Y and Yamada S 2005 The size-dependent magnetic properties of Co3O4 nanoparticles *Polyhedron* **24** 2813–6

[43] Herner S B, Weerakkody A D, Belkadi A and Moddel G 2017 High performance MIIM diode based on cobalt oxide/titanium oxide *Applied Physics Letters* **110** 223901

[44] Azad I, Ram M K, Goswami D Y and Stefanakos E 2018 Fabrication and characterization of NiO based metal−insulator−metal diode using Langmuir-Blodgett method for high frequency rectification *AIP Advances* **8** 045219

[45] Li J, Shao Y, Chen X, Wang H, Li Y and Zhang Q 2016 All-inorganic quantum-dot light-emitting-diodes with vertical nickel oxide nanosheets as hole transport layer *Progress in Natural Science: Materials International* **26** 503–9

[46] Xiong C, Zhang T, Kong W, Zhang Z, Qu H, Chen W, Wang Y, Luo L and Zheng L 2018 ZIF-67 derived porous Co3O4 hollow nanopolyhedron functionalized solution-gated graphene transistors for simultaneous detection of glucose and uric acid in tears *Biosensors and Bioelectronics* **101** 21–8

[47] Mohan S, Srivastava P, Maheshwari S N, Sundar S and Prakash R 2011 Nano Structured Nickel Oxide based DNA Biosensor for Detection of Visceral Leishmaniasis (Kala-azar) *Analyst* **136** 2845–51

[48] Mishra S, Yogi P, Sagdeo P R and Kumar R 2018 Mesoporous Nickel Oxide (NiO) Nanopetals for Ultrasensitive Glucose Sensing *Nanoscale Res Lett* **13**

[49] Benchettara A and Benchettara A 2015 Electrochemical Sensor Based on Nanoparticles of Cobalt Oxides for Determination of Glucose *Materials Today: Proceedings* **2** 4212–6

[50] Dalkıran B, Erden P E and Kılıç E 2016 CONSTRUCTION OF AN ELECTROCHEMICAL XANTHINE BIOSENSOR BASED ON GRAPHENE/COBALT OXIDE NANOPARTICLES/CHITOSAN COMPOSITE FOR FISH FRESHNESS DETECTION *Journal of the Turkish Chemical Society, Section A: Chemistry* **3**

[51] He K, Zhang S, Li J, Yu X, Meng Q, Zhu Y, Hu E, Sun K, Yun H, Yang X-Q, Zhu Y, Gan H, Mo Y, Stach E A, Murray C B and Su D 2016 Visualizing non-equilibrium lithiation of spinel oxide via in situ transmission electron microscopy *Nature Communications* **7** 1–9

[52] Swanson H E and Tatge E 1953 *Standard X-ray Diffraction Powder Pattern* (USA: National Bureau of Standards)

[53] Swanson H E, Morris M C, Stinchfield R P and Evans E H 1962 *Standard x-ray diffraction powder patterns* (USA: National Bureau of Standards)

[54] Wang R, Lang J, Liu Y, Lin Z and Yan X 2015 Ultra-small, size-controlled Ni(OH) 2 nanoparticles: elucidating the relationship between particle size and electrochemical performance for advanced energy storage devices *NPG Asia Materials* **7** e183–e183

[55] Luo Y, Li G, Duan G and Zhang L 2006 One-step synthesis of spherical α-Ni(OH) $_2$ nanoarchitectures *Nanotechnology* **17** 4278–83

[56] Bartůněk V, Huber Š, Sedmidubský D, Sofer Z, Šimek P and Jankovský O 2014 CoO and Co3O4 nanoparticles with a tunable particle size *Ceramics International* **40** 12591–5

[57] Cui H, Zhao Y, Ren W, Wang M and Liu Y 2013 Large scale selective synthesis of α-Co(OH)2 and β-Co(OH)2 nanosheets through a fluoride ions mediated phase transformation process *Journal of Alloys and Compounds* **562** 33–7

[58] Yang J, Liu H, Martens W N and Frost R L 2010 Synthesis and Characterization of Cobalt Hydroxide, Cobalt Oxyhydroxide, and Cobalt Oxide Nanodiscs *The Journal of Physical Chemistry C* **114** 111–9

[59] Sta I, Jlassi M, Kandyla M, Hajji M, Koralli P, Allagui R, Kompitsas M and Ezzaouia H 2015 Hydrogen sensing by sol–gel grown NiO and NiO:Li thin films *Journal of Alloys and Compounds* **626** 87–92

[60] Sagadevan S and Podder J 2015 Investigations on structural, optical, morphological and electrical properties of nickel oxide nanoparticles *International Journal of Nanoparticles* **8** 289

[61] Blakemore J D, Gray H B, Winkler J R and Müller A M 2013 Co3O4 Nanoparticle Water-Oxidation Catalysts Made by Pulsed-Laser Ablation in Liquids *ACS Catalysis* **3** 2497–500

[62] Alrehaily L, Joseph J, Biesinger M, Guzonas D and Wren J 2012 Gamma-radiolysis-assisted cobalt oxide nanoparticle formation *Physical chemistry chemical physics : PCCP* **15**

[63] Ravi Dhas C, Venkatesh R, Jothivenkatachalam K, Nithya A, Suji Benjamin B, Moses Ezhil Raj A, Jeyadheepan K and Sanjeeviraja C 2015 Visible light driven photocatalytic degradation of Rhodamine B and Direct Red using cobalt oxide nanoparticles *Ceramics International* **41** 9301–13

[64] Farhadi S, Pourzare K and Sadeghinejad S 2014 Synthesis and characterization of Co3O4 nanoplates by simple thermolysis of the [Co(NH3)6]2(C2O4)3·4H2O complex *Polyhedron* **67** 104–10

[65] Li R, Tang L, Zhao Q, Ly T H, Teng K S, Li Y, Hu Y, Shu C and Lau S P 2019 In2S3 Quantum Dots: Preparation, Properties and Optoelectronic Application *Nanoscale Res Lett* **14** 161

[66] Itapu S, Borra V and Mossayebi F 2018 A Computational Study on the Variation of Bandgap Due to Native Defects in Non-Stoichiometric NiO and Pd, Pt Doping in Stoichiometric NiO *Condensed Matter* **3** 46

[67] Lenglet M and Jørgensen C K 1994 Reinvestigation of the optical properties of Co3O4 *Chemical Physics Letters* **229** 616–20

[68] Rödl C and Schleife A 2014 Photoemission spectra and effective masses of n- and p-type oxide semiconductors from first principles: ZnO, CdO, SnO2, MnO, and NiO *physica status solidi (a)* **211** 74–81

[69] Cheng C-S, Serizawa M, Sakata H and Hirayama T 1998 Electrical conductivity of Co3O4 films prepared by chemical vapour deposition *Materials Chemistry and Physics* **53** 225–30

[70] Garoufalis C S, Barnasas A, Stamatelatos A, Karoutsos V, Grammatikopoulos S, Poulopoulos P and Baskoutas S 2018 A Study of Quantum Confinement Effects in Ultrathin NiO Films Performed by Experiment and Theory *Materials (Basel)* **11**

[71] Kashir A, Jeong H-W, Lee G, Mikheenko P and Jeong Y H Dielectric properties of strained NiO thin films 14